UNIVERSITY OF CALIFORNIA
SANTA CRUZ

POROUS NITROGEN-DOPED ELECTROCATALYST FOR THE OXYGEN REDUCTION REACTION IN ALKALINE MEDIA

A dissertation submitted in partial satisfaction
of the requirements for the degree of

DOCTOR OF PHILOSOPHY

in

CHEMISTRY

by

Rene Mercado

September 2021

The Dissertation of Rene Mercado is approved:

_____
Professor Shaowei Chen, Chair

_____
Professor Ilan Benjamin

_____
Professor Scott Oliver

_____
Peter Biehl
Vice Provost and Dean of Graduate Studies

Table of Contents

List of Figures

List of Tables

Abstract

Porous nitrogen-doped electrocatalyst for the oxygen reduction reaction in alkaline media

By

Rene Mercado

The intense research interest in nanomaterials is largely fueled by the unique properties of nanoscale materials. Because of this, fuel cell technology can benefit from the optimization of nanomaterials. However, since Platinum is the leading state-of-the-art electrocatalyst for ORR, developing a catalyst that is cost efficient is under investigation. Developing electrocatalyst that are abundant earth metals is critical for a large-scale application of fuel cell technology. Among the non-precious metals explored in recent decades; Iron, Cobalt, and Nickel catalyst are regarded to be the most suitable candidate for the oxygen binding intermediates of ORR. Therefore, by introducing an additional non-noble metal, a bimetallic system, can have a further influence on the activity for ORR. Because of this, my dissertation will focus on a bimetallic system where they will be deposited onto two 3D nitrogen-doped carbon skeleton structures.

In chapter 1, fuel cell reaction mechanism is introduced. A systemic overview of designing Metal Nitrogen Centers (MNC'S) using various techniques. Additionally, the design of nitrogen centers in carbon materials is crucial for ORR. Upon the deposition of metals on nitrogen doped carbon, the M-N coordination site has shown to be the active site. Therefore, optimization of M-N site is done by using delicate selection of precursors, a process where is largely based on test and trial method.

Chapter 2 describes the design of CHS-FeCo(X) carbon cages using SiO_2 as a sacrificial template. A series of CHS-FeCo-X metal to metal mole feed ratio was used. The deposition of both Fe and Co resulted in single atoms decorated on the carbon skeleton as seen by the TEM. Furthermore, the chemical composition of CHS-FeCo(X) is in agreement with TEM,

suggesting an oxidized state. Additionally, all dual-metal samples showed a significant enhancement of the catalytic performance towards ORR in alkaline media, compared to its single metal dopants.

Chapter 3 is an extension of chapter 2. In this chapter, cobalt complexes were used instead of cobalt chloride salt. Electron microscopy also confirmed hollow carbon cages. However, due to the higher uptake of metals, nanoparticles occur. Additionally, FeCo-NC-$Na_3[Co(NO_2)_6]$ and FeCo-NC- $[Co(im)_4](NO_3)_2$ exhibited metallic phases as seen by both them and XPS with an obvious M-N interaction. Moreover, XPS, a charge transfer from Fe to Co was seen. Such an interaction resulted in a highly active electrocatalyst.

In chapter 4, a soft template synthesis was used to engineer 3D- hierarchical bimetallic (Fe,Ni) carbon nanoflowers. Transmission electron microscopy studies show that FeNi-NCF samples had a consisted flower-like morphology over various pyrolysis temperature. The FeN-NCF(3) sample had three times the uptake of iron compared to nickel. Additionally, XPS showed that it had the largest Ni to Fe electron transfer. Because of this, it exhibited an active electrocatalyst in alkaline conditions.

Acknowledgements

First, I would like to thank my family (Too many to name, you know who you are). To be honest, if I didn't have them, I probably wouldn't have made it this far. As my graduate study chapter is coming to a close, I am opening a new chapter: my wife Daffne will be giving birth to Maximus! Maximus, you are not here yet, but I hope that someday you see all the sacrifices I went through to try to achieve my American dream. Many people believed that I wasn't going to be able to make it, now look at me. If I can do it, with no role model in my life, then I know you can, because I will be there. I will do my best to help you out, so you won't have to struggle as your dad did. Hey kid, live life, have fun, and don't be too crazy like your dad. I love you! To Daffne, you have seen it all. From my early beginnings of my low-life junkie/wannabe gangster life to now actually receiving a PhD. Babe I got you! 13 years ago, I didn't even know what a degree was. At my 33 years of age, I have received a doctorate in physical chemistry. A doctorate? Still, can't believe it.

I would like to thank my advisor, Professor Shaowei Chen for being my mentor. Shaowei, you have pushed me many times to better myself and thank you for that. You made me become a better scientist and for that I greatly appreciate it. To Scott Oliver, thank you for always having time to meet me and have great conversations regarding my Dodgers! Always appreciated your great questions throughout my graduate career. To Ilan Benjamin, I appreciate you becoming my committee chair and always responding to all my late emails.

From lab mates to great friends: thank you Bing, Carolin, and John. Each of you have really helped in different ways. From talking about science to enjoying lunch and just laughing. Each of you made graduate school easy at one point in my graduate career.

Before I close this chapter, I want to say thank you again for those who have helped me. The motto I live by is, "Help those who have helped you". Signing out. Eltrapscientist/LaHueva

1. Introduction

1.1 Background and Overview

One of the grand challenges of this century is to develop cost-effective energy storage technologies that would allow the use of low-cost electricity from renewable sources to meet our energy needs, which will enable the development of human society.[1,2] However, due to the increase in personal mobility mainly derived from automobiles raises environmental concerns such as exhaust emission and global warming. Additionally, the depletion of fossil fuels and the rise in gas emissions, requires developing sustainable, high efficiency requires pressing attention.[3] Because of this, extensive studies have been carried out on novel energy application and storage technologies, such as proton exchange membrane fuel cell (PEMFC)[4] and lithium-Ion batteries[5], etc.

Amongst these devices, hydrogen fuel cells have attracted the special attention because of their high theoretical energy densities. Besides its electrochemical performance, hydrogen fuel cells also have the advantage of being environment friendly as their only byproduct are heat and water, making them the most promising technologies for the future of renewable applications.[6] Therefore, this dissertation is focused on the design of porous carbon materials for ORR.

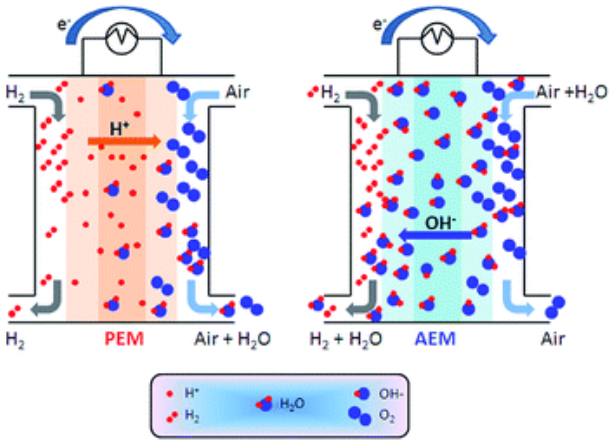

Figure 1.1 Schematic design of PEMFC in both acidic and alkaline electrolytes.

1.2 Mechanism of oxygen reduction reaction (ORR): Electrochemistry reaction of PEMFC's

As seen in figure 1.1, PEMFC's can happen in both acidic and alkaline electrolytes with their respective equation, via the four-electron pathway,

$$O_2+4H^++4e^-\rightarrow 2H_2O \text{ (acidic electrolyte) (1)}$$

$$O_2+ 2H_2O+4e^-\rightarrow 4OH^- \text{ (alkaline electrolyte) (2)}$$

Or the two-electron pathway,

$$O_2+2H^++2e^-\rightarrow H_2O_2 \text{ (acidic electrolyte) (3)}$$

$$O_2+ 2H_2O+2e^-\rightarrow H_2O_2+ 2OH^- \text{ (alkaline electrolyte) (4)}$$

Overall,

$$2H_2 +O_2\rightarrow 2H_2O \text{ (E cell=1.23V both acid and alkali) (5)}$$

Where the ORR prefers the 4e pathway, with minimal production of H_2O_2.[7] Though the electrode reactions can be different at various stages within the two conditions, but the overall reaction of the cells will be the same (equation 5), thus generating an open circuit

voltage of + 1.23 V under standard conditions.[8] Yet, one major issue lies in the sluggish oxygen reduction reaction (ORR) that takes place at the cathode. Therefore, development high efficiency, durability and low cost is required for commercialization of fuel cell technology. In spite that ORR follows similar reaction intermediate species in both alkaline and acid electrolyte, it has been noticed that it is much easier for active non-Pt electrocatalyst to achieve a high performance in alkaline than acidic electrolyte. This partly can be due to the electrocatalyst being unstable in acid. In a typical electrochemical test, the onset potential (E_{onset}), half-wave potential ($E_{1/2}$), diffusion-limited current and H_2O_2 yield are the commonly used parameters in the assessment of electrocatalytic activity. Within this thesis Pt/C will be used as the benchmark which has E_{onset}= +1.00V vs reversible hydrogen electrode (RHE), $E_{1/2}$ of +0.85V, limited current density of 5-6 mA/cm_2, and an electron transfer number (n) of 4. Moreover, Pt/C is considered the best commercialized electrocatalyst. However, Pt-based electrocatalyst exhibit long-term durability failure during its electrocatalytic operation, due to Ostwald ripening and deactivation by adsorption of CO intermediated on its surface.[9,10] Additionally, making it unsuitable use for commercial setting. Additionally, the low natural abundance leading to the high cost of Pt have significantly hindered the widespread commercialization of such technologies.[11]

Table 1. A list of ORRs and their reaction potentials in aqueous electrolytes.[21]

Electrolyte	Reaction pathway	Reaction potential [V] vs. NHE
alkaline	*4e pathway:*	
	$O_2+2H_2O+4e^-\rightarrow 4OH^-$	+0.401
	[2+2] e⁻ pathway:	
	$O_2+H_2O+2e^-\rightarrow HO_2^-+OH^-$	−0.065
	$HO_2^-+H_2O+2e^-\rightarrow 3OH^-$	+0.867
acidic	*4e pathway:*	
	$O_2+4H^++4e^-\rightarrow 2H_2O$	+1.229
	[2+2]e pathway:	
	$O_2+2H^++2e^-\rightarrow H_2O_2$	+0.70
	$H_2O_2+2H^++2e^-\rightarrow 2H_2O$	+1.76

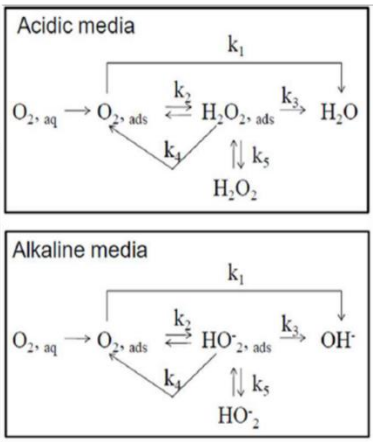

Figure 1.2 Summary of standard reaction potential of the corresponding reaction involved for ORR (left) and scheme of ORR reaction routes in acidic and alkaline media (right).[12]

Moreover, as stated oxygen reduction can take place in which four or two electrons are passed from the electrode to a molecular oxygen. This will be dependent on the electrolyte, which will force a reaction route that it will follow. Figure 1.2 shows both the possible 4 and $2e^-$ routes for ORR and the specific reaction formula involved in both acidic and alkaline media. As seen, upon the adsorption of oxygen molecule onto the surface of the electrode, there are four main routes the reaction can follow. **(1)** In the case of four electrons inserted into an oxygen molecule, it will form two water molecules in acidic media or four hydroxide ions in alkaline media given a direct (K_1) pathway without any intermediate products, known as the $4e^-$ pathway. **(2)** For the serial $2+2e^-$ pathway, the adsorbed oxygen molecule takes only two electrons at first, turning it into adsorbed peroxide species accepting another two electrons (K_2,K_3), forming the same final products as in the former pathway. **(3)** In order to produce a $2e^-$ pathway, the adsorbed peroxide species, will either decompose, forming a new oxygen molecule that goes back into the reduction cycle (K_4), or desorb from the electrode surface and go into the bulk electrolyte (K_5). Therefore, in order achieve a fuel cell with high energy density, the direct $4e^-$ pathway which has the fastest kinetics, will be the favorable route.

1.3 Insights and challenges for electrocatalyst

1.3.1 Binding of oxygen intermediates on metal substrates

As mentioned previously, the ORR pathway is directly correlated to the electrolyte used. However, it also varies depending on the choice of catalyst. To further understand the catalytic mechanism of ORR, we should understand some insights on the interaction that is involved between the catalyst surface and the intermediate species. The volcano plot (Figure 1.3) shows a relationship between the M-O and M-OH bond energies and the catalytic activity of the metal electrocatalyst, through electronic structure calculations combined with density functional calculations (DFT). [13] As seen in Figure 3, a volcano shape appears when plotting the activity of various transition against the oxygen intermediate binding energies. One can see that for the metals on the left of the volcano plot, their high oxygen binding energies make it easy for the adsorption of oxygen to form metal oxides. Whereas those on the right, due to their filled d orbitals, they weakly interact with the oxygen molecules, which will prevent the formation of back bonding between the metal and oxygen atoms. Therefore, these metal surfaces cannot simply activate the cleavage of O-O bond, thus leading to a poor catalytic behavior. Pt-like groups are the closest to the peak of the volcano plot indicating a moderate-optimal oxygen binding energy. Where the cleavage of O-O bond can be promoted by the M-O interactions. While Platinum is known to have a high catalytic activity for ORR, the volcano plot indicates that there is still room for improvement.[14,15] The binding of oxygen molecule on the platinum surface of Pt (111) at high potentials is still too favorable, leading to a high over-potential of 300mV for ORR.

1.3.2 d-band center theory

Additionally, the d-band center theory can be used to interpret the interaction between metal surface and adsorbates. The Metal-O (M-O) bond strength is dependent on the overlap of the 2p oxygen and d orbitals of the transition metals and how well they match with each other. The more the antibonding states are occupied, the weaker the M-O, and the

relative position of the d-band center to the fermi level influences the filling condition. To produce a stronger M-O bond, a shifting of the d-band center upward from the Fermi level is needed, resulting in a less occupancy in the antibonding states.[16] Because of this, there has been intensive efforts to adjust the electronic properties of platinum and other non-noble metals to Improve its catalytic activity which will be mentioned in the next section.

1.4 Metals for ORR

1.4.1 Noble metals for ORR

As mentioned, platinum and noble-based are the most efficient for ORR. Yet, some of the electrocatalytic activity remain subpar for practical applications. Additionally, when using noble metals, the development of the electrocatalyst should result in high performance electrocatalyst. A way to enhance the performance is to adjust the electronic properties of platinum and other noble metals (Pd and Ru) in the improvement of activity for ORR, the alloying with other transition metals should lead to a large effect on its oxygen binding intermediates, resulting in an active catalyst. It is expected that a bimetallic system can display not only a combination of the properties associated with each distinct metal, but also new or unexplored properties due to a possible synergistic effect between each metal. [17,18]In addition, the performance can also be boosted by reasonable selection of the alloy metals and the precise control of the size, leading to cost motivated.

The current strategies of these alloy-type structures are to enhance the intrinsic activity by engineering the surface in order to increase the active sites on the surface. For example, Stamenkovic et al.[15] discovered Pt_3Ni open framework had three-dimensional accessibility edges (Figure 1.4). Signifying that these exposed (111) surfaces were able to reach a half wave potential ($E_{1/2}$) of almost 100mV more positive than that state of the art Pt/C. Wang et al.[19] designed and synthesized square Pd_3Pb nanosheets. These square nanosheets endowed the Pd_3Pb catalyst with a high specific area and a large amount of exposed active sites. It was found that due to Pd_3Pb 3d states being closer to the fermi level

than those of Pd and Pt, and with a preferred orientation (100) resulted in high electrocatalytic ORR performance, and their mass activity of 0.78 A mg^{-1} at 0.9V was 7.1 times higher than that of commercialized Pt/C catalyst.

As stated, cost has a great influence on the commercialization of fuel cell technology. To decrease the cost of noble metals, such as those Pt-like electrocatalyst, metal loading must decrease. For instance, the noble metal particles mass loading must decrease as much as possible. For example, synthesized 2 nm Pt_3Co nanoparticles on a Co-N doped carbon substrate resulted in an ultralow Pt loading at a mass ration of 2.7 wt% and a high mass activity of 1.77 A/mg.[20] In addition, noble metal single atoms (SAC's) have also been widely used and have shown promising results for ORR.[21,22] Furthermore, these SAC's have shown great performance when a substrate of carbon[23], metal sulfide[24], metal phosphide[25], etc. As seen, a catalyst with a lower content of Pt metal can not only inherit the properties of Pt constituent, but also show a superior performance when compared to monometallic Pt.

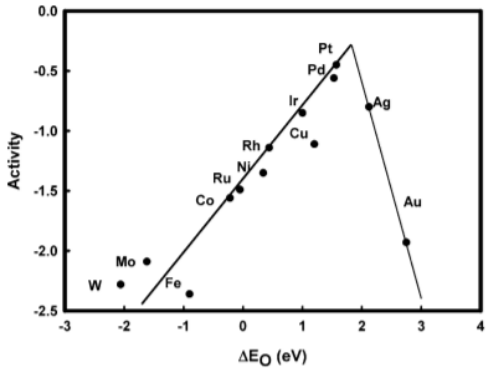

Figure 1.3 Trends in oxygen reduction activity plotted as a function of the oxygen binding energy.

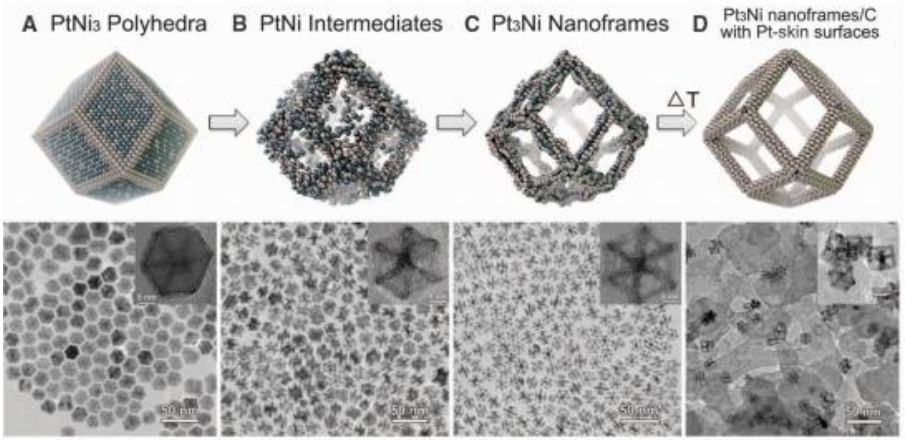

Figure 1.4 Schematic illustrations and corresponding TEM images at four stages during evolution process.

1.4.2 Non-noble metals for ORR

The development of nonprecious metal electrocatalyst for ORR that can replace platinum is crucial for the commercialization of fuel cells due to their low cost, high stability, and poisoning resistance. Among the non-precious metal catalyst, Fe[26], Co[27], and Ni[28] have showed promising ORR activity. Moreover, some of these catalysts even surpass noble materials. For example, Fe/N/C [29] has shown to have a better ORR activity than commercial Pt/C in alkaline electrolyte. The pyrolysis of Fe/N/C structure have shown that their nitrogen centers can be tailored to increase the activity for ORR in both acidic and alkaline media.[30–32] However, active sites of these Metal/N/C (M/N/C) is under debate and will be discussed in a later section.[33]

1.5 The design of carbon nanomaterials for ORR

1.5.1 Carbon materials used as a substrate for various energy applications.

Porous carbon has gained continuous interest do their broad range of applications in CO_2 capture[34], energy storage[35] , and catalysis[36]. Due to their various advantages, such as high surface area, chemical stability, tunability over pore geometries, pore dimensions, as well as the flexibility to hetero and metal doped or surface functionalization, which will be discussed in later sections.[37,38] A wide range of precursors and design of synthesis has enabled to produce hierarchical porous carbons, some of which include resin (e.g., melamine-formaldehyde resin[30], urea-formaldehyde resin[39]) and sacrificial templates (SiO_2 stober method[40]). Typically the preparation of these carbon materials involves carbonization and activation. The carbonization step removes volatile components in the precursor leaving a carbon rich product.[41] Within activation, a certain activating precursor can further create/tune the pore size, which results in various pore sizes (e.g., micropores and/or mesopores).[42] These low-cost porous carbon can reach a high surface area of up to 3000 m^2g^{-1} which can have a large influence on catalysis and in return, can lead to larger exposed active sites. Moreover, carbon materials provide great support for the loading of variety of metal centers, which can consequently lead to strong metal-support interactions.[43] Such parameters of carbon-based materials have shown to be a great outlook for electrocatalysis.

1.5.2 Nitrogen doped carbon used as an effective ORR catalyst

Metal free catalysis on nitrogen-doped carbon materials has shown to have high activity for ORR. It's proposed that this may be attributed to the larger electronegativity with respect to C atoms. Therefore, by creating a positive charge density on the adjacent C atoms, leading to a controlled adsorption of oxygen intermediate species.[44] In nitrogen-doped catalyst, the molecular structure of nitrogen has a critical role in affecting the properties of the N-doped carbon materials. Preparation of N-doped porous carbon materials were first demonstrated by using hard silica template and with conventional CVD of styrene and

acetonitrile as carbon and nitrogen sources, respectively.[45] Since then, various methods have been developed for the synthesis of N doped materials.[46] These methods have led to various nitrogen doping as seen in Figure 1.5.[47] Yet, their active sites and mechanism have been controversial. Some have claimed that Pyridinic, Pyrrolic or the nitrogen-carbon (CN_x) moieties are the active centers when metals are bound.[48,49] Until recently, it has been verified that Metal-N_x plays the dominant role, which will be in detail in the subsequent sections.[50–52]

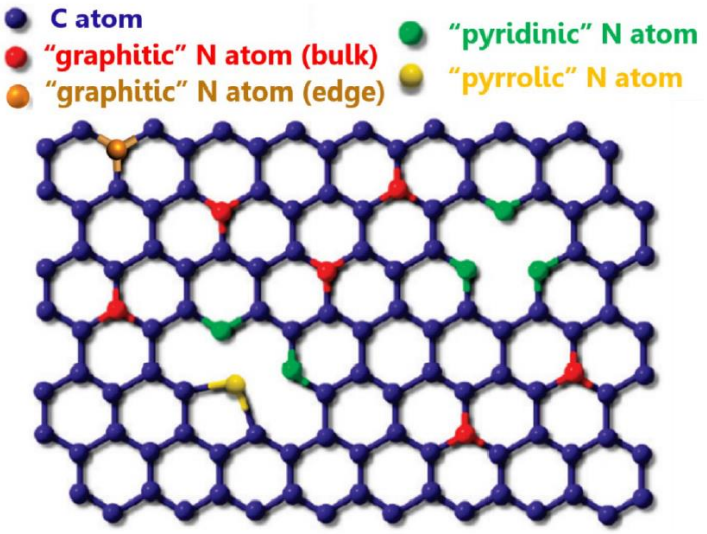

Figure 1.5 Schematic representation of different type of N atoms (graphitic, pyridinic, and pyrrolic N, red, green, and yellow, respectively) in nitrogen doped carbon.

1.5.3 Metal-Nitrogen-Carbon (M-N-C) catalyst

During the final stages of respiration, the protein cytochrome C oxidats (Cco) catalyzes the reduction of O_2 to H_2O in order to power its proton pump activity. The well understood mechanism of Cco is the myoglobin-like Fe-poryhpyrin that is adjacent to Cu coordinated by three histidine ligands, due to its favorability of oxygen binding.[53] Having such a bimetallic active site structure enables the oxygen molecule to adopt a bridge-like configuration when adsorbing onto the metal centers (Figure 1.6). This configuration has the great advantage of activating the O-O bond, resulting in the four-electron pathway. Due to

success of biocatalyst in facilitating the ORR in mammalian's body, researchers have attempted to develop similar structures that have M-N-C as ORR catalyst.

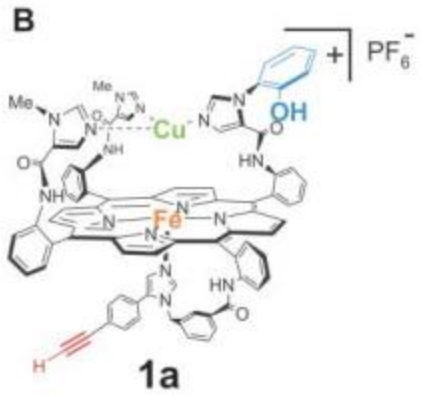

Figure 1.6 Model of Cco active site.

The first discovery of developing a similar structure that resembled a phtalocyanine was in 1964.[54] Ever since, the research field of M-N-C has allowed for the engineering of these macromolecules catalyzing ORR. These macromolecules have led to the synthesis of MN_X macrocycles within a carbon support. However, the MN_X is not stable enough in acidic media. It was later found that pyrolyzing the metal center macromolecule can result in better catalytic activity and stability.[55] However, the synthetic process was complex which led to using high cost techniques. Later on, a major breakthrough, where they synthesized the MN_x catalyst via pyrolysis by just using a mixture of nitrogen and cobalt precursors on a carbon support, which revealed that high performance MN_x electrocatalyst could be synthesized with cheap precursors.[56] Ever since, several works have followed similar synthetic techniques, leading to a success on catalyzing ORR. Even with the great increase of MN_x, challenges are still present, understanding the catalytic functions nitrogen centers and the rationale design of the catalyst structure is needed.

Even though many have used the standard synthetic route for the fabrication of M-N-C, its still challenging to reveal the mechanism and the identity of the active sites. Due to using

various precursor and certain synthetic techniques, the M-N-C catalyst has resulted in complex structures with inconsistent active centers. As stated previously, upon nitrogen dopants there are various types of nitrogen centers that can contribute toward the high activity for ORR. However, whatever the active site is, it is primarily decided by the electronic and geometric configuration of the metal atoms, where even small changes of their chemical environment can discriminate towards a certain catalytic mechanism. Because of this, the development of these catalyst has been greatly hampered due to their difficult structural characterization and active site identification.

M-N-C catalyst have demonstrated the be the most active for ORR among all M-N-C studied. As stated, two main active sites have been suggested to account for their high activity. They include iron-nitrogen centers (MN_x) embedded in the carbon matrix and (CN_x). The distinction between the two active sites lies on the role of the transition metal. For MN_x, the iron center is involved in the direct oxygen intermediate binding. Whereas, CN_x is a product during the pyrolysis formation of nitrogen rich precursors. However, research has concluded that these strictly do not participate catalyzing ORR on its own.

As stated, among all M-N-C, Fe-N-C centers have surpassed noble metals and commercialized Pt/C for ORR. Many researchers have found that pyrolyzing a mixture of iron precursor and nitrogen-containing carbon precursor has led to the development of FeN_4 moieties. The high ORR activity of FeN_4 structures has been attributed to optimal adsorption strength between the oxygen intermediates and the center of the Fe atom.[57] It was also confirmed that FeN_4 in alkaline media, while the reducing of oxygen, Fe resided out-of-plane and it would move back when bound to all four nitrogen centers at higher potentials. Therefore, Fe co-existed in two oxidation states Fe^{3+}/Fe^{2+}, signifying that near graphitic neighbors served as the electron-withdrawing groups. Because of this, FeN_4 coordination structure weakens the binding intermediates, leading to stabilizing these moieties at higher potentials.[57,58]

Prior to a better understanding of FeN_4 active moieties, researchers claim that metal centers only catalyze the formation of active various nitrogen centers (graphitic, pyriding, and pyrrolic) sites. It well understood that nitrogen centers can serve as “anchors” for both medal and oxygen intermediates for ORR. For example, producing a larger percentage of pyridinic dopant resulted in a drastic improvement for ORR in non-noble metals catalyst (cite). On the other hand, a group proposed that the carbon adjacent to pyridic are the active sites for N-doped carbon materials. Because of this, it has remained a challenge to attribute ORR activity on various CN_x centers. In order to further suggest an active site, there are couple of experiments researchers have done and will be discussed in subsequent section.

1.6 Characterization techniques and experiments for elucidating the “active site”.

1.6.1 Characterization

To find the existence of single atoms state of the art techniques are used. In a typical experiment, the morphology and elemental distribution can be analyzed through microscopy techniques (TEM, SEM, and HAADF-STEM). Additionally, to find signals of both Metal and Nitrogen centers in MN_X moieties, EELS mapping spectrum can produce sub-angstrom level resolution, which will lead to further elucidating if both metal and nitrogen are adjacent to one another, providing visual evidence for the existence of MN_x structures. The contents of elements can be quantitatively identified by ICP-OES. XPS measurement can reveal both the valance state and charge transfer properties, which can confirm the existence of Fe bound to pyridinic nitrogen at the edge of carbon scaffold. The porosity and surface area of carbon material can be measured by gas adsorption technique, such as Brunauer-Emmett-Teller method (BET). For more accurate identification of MN_x structure, X-ray absorption near-edge spectroscopy (XANES) and extended X-ray absorption fine structure (EXAFS) analysis, which are highly precise to the chemical environment, such as electron structure of an element and the type of coordination structure.

1.6.2 Elucidating the "active site"

Besides showing the existence of MN_X, various comparison studies are employed to elucidate its role as they ORR active site. For example, acid treatment can be used to selectively remove Fe-based nanoparticles without affecting the FeN_x centers. Many studies have reported that upon the nanoparticle removal, the ORR activity can result in an improved ORR or not depending on if FeN_x moieties are responsible for the ORR.[56,59,60] Poisoning tests are also a commonly used to better understand the active site. In this test, sulfur compounds are known to strongly adsorb onto metal sites, such as those seen in KSCN.[61] Because of this, FeN_x sites can be identified when embedded in the carbon matrix. To identify whether the active site is FeN_x or others withing the materials, using KSCN as the poisoning source, the Fe centers can then be blocked. In this study, they tested the ORR activity in the presence of 10mM KCN and found that $E_{1/2}$ exhibited a negative shift of 18mV, signifying that the contribution from FeN_x sites was minor, suggesting for the active site being carbon as seen in figure 1.7.[62]Where as, having decorated FeN_x throughout the carbon skeleton, the poisoning test of KSCN, resulting in no change, thus correlating their activity to these rich MN_x structures.[30]

Electrochemical performance test can also give us insight into the active site. As stated earlier, CN_x structures active sites are highly controversial. A group carried out an XPS experiment paired with CV cycles. They notice upon the concentration change (pyridinic, graphitic, or pyrrolic) through XPS that the ORR activity decreased as the as percentage of graphitic nitrogen also decreased, while the other CN_x exhibited no correlation.[63] Because of this, they correlated their high active electrocatalyst to graphitic nitrogen centers.

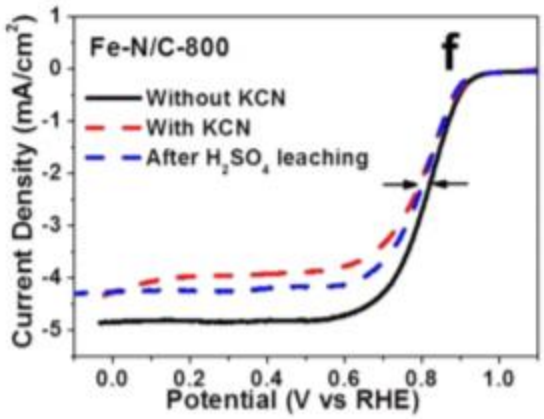

Figure 1.7KSCN poisoning teste

1.7 References

(1) Cook, T. R.; Dogutan, D. K.; Reece, S. Y.; Surendranath, Y.; Teets, T. S.; Nocera, D. G. Solar Energy Supply and Storage for the Legacy and Nonlegacy Worlds. *Chem Rev* **2010**, *110* (11), 6474–6502. https://doi.org/10.1021/cr100246c.

(2) Nitopi, S.; Bertheussen, E.; Scott, S. B.; Liu, X.; Engstfeld, A. K.; Horch, S.; Seger, B.; Stephens, I. E. L.; Chan, K.; Hahn, C.; Nørskov, J. K.; Jaramillo, T. F.; Chorkendorff, I. Progress and Perspectives of Electrochemical CO 2 Reduction on Copper in Aqueous Electrolyte. *Chem Rev* **2019**, *119* (12), 7610–7672. https://doi.org/10.1021/acs.chemrev.8b00705.

(3) Anantharaj, S.; Ede, S. R.; Sakthikumar, K.; Karthick, K.; Mishra, S.; Kundu, S. Recent Trends and Perspectives in Electrochemical Water Splitting with an Emphasis on Sulfide, Selenide, and Phosphide Catalysts of Fe, Co, and Ni: A Review. *Acs Catal* **2016**, *6* (12), 8069–8097. https://doi.org/10.1021/acscatal.6b02479.

(4) Yang, W.; Peng, Y.; Zhang, Y.; Lu, J. E.; Li, J.; Chen, S. Air Cathode Catalysts of Microbial Fuel Cell by Nitrogen-Doped Carbon Aerogels. *Acs Sustain Chem Eng* **2018**, *7* (4), 3917–3924. https://doi.org/10.1021/acssuschemeng.8b05000.

(5) Manthiram, A. A Reflection on Lithium-Ion Battery Cathode Chemistry. *Nat Commun* **2020**, *11* (1), 1550. https://doi.org/10.1038/s41467-020-15355-0.

(6) Kirubakaran, A.; Jain, S.; Nema, R. K. A Review on Fuel Cell Technologies and Power Electronic Interface. *Renew Sustain Energy Rev* **2009**, *13* (9), 2430–2440. https://doi.org/10.1016/j.rser.2009.04.004.

(7) Jung, E.; Shin, H.; Antink, W. H.; Sung, Y.-E.; Hyeon, T. Recent Advances in Electrochemical Oxygen Reduction to H 2 O 2 : Catalyst and Cell Design. *Acs Energy Lett* **2020**, *5* (6), 1881–1892. https://doi.org/10.1021/acsenergylett.0c00812.

(8) Varcoe, J. R.; Atanassov, P.; Dekel, D. R.; Herring, A. M.; Hickner, M. A.; Kohl, Paul. A.; Kucernak, A. R.; Mustain, W. E.; Nijmeijer, K.; Scott, K.; Xu, T.; Zhuang, L. Anion-Exchange Membranes in Electrochemical Energy Systems. *Energ Environ Sci* **2014**, *7* (10), 3135–3191. https://doi.org/10.1039/c4ee01303d.

(9) He, G.; Song, Y.; Liu, K.; Walter, A.; Chen, S.; Chen, S. Oxygen Reduction Catalyzed by Platinum Nanoparticles Supported on Graphene Quantum Dots. *Acs Catal* **2013**, *3* (5), 831–838. https://doi.org/10.1021/cs400114s.

(10) Ustarroz, J.; Ornelas, I. M.; Zhang, G.; Perry, D.; Kang, M.; Bentley, C. L.; Walker, M.; Unwin, P. R. Mobility and Poisoning of Mass-Selected Platinum Nanoclusters during the Oxygen Reduction Reaction. *Acs Catal* **2018**, *8* (8), 6775–6790. https://doi.org/10.1021/acscatal.8b00553.

(11) Wang, W.; Lei, B.; Guo, S. Engineering Multimetallic Nanocrystals for Highly Efficient Oxygen Reduction Catalysts. *Adv Energy Mater* **2016**, *6* (17), 1600236. https://doi.org/10.1002/aenm.201600236.

(12) Wu, K.; Wang, D.; Su, D.; Gentle, I. R. A Discussion on the Activity Origin in Metal-Free Nitrogen-Doped Carbons For Oxygen Reduction Reaction and Their Mechanisms. *Chemsuschem* **2015**, *8* (17), 2772–2788. https://doi.org/10.1002/cssc.201500373.

(13) Nørskov, J. K.; Rossmeisl, J.; Logadottir, A.; Lindqvist, L.; Kitchin, J. R.; Bligaard, T.; Jónsson, H. Origin of the Overpotential for Oxygen Reduction at a Fuel-Cell Cathode. *J Phys Chem B* **2004**, *108* (46), 17886–17892. https://doi.org/10.1021/jp047349j.

(14) Lu, B.; Guo, L.; Wu, F.; Peng, Y.; Lu, J.; Smart, T.; Wang, N.; Finfrock, Y.; Morris, D.; Zhang, P.; Li, N.; Gao, P.; Ping, Y.; Chen, S. Ruthenium Atomically Dispersed in Carbon Outperforms Platinum toward Hydrogen Evolution in Alkaline Media. *Nat Commun* **2019**, *10* (1), 631. https://doi.org/10.1038/s41467-019-08419-3.

(15) Chen, C.; Kang, Y.; Huo, Z.; Zhu, Z.; Huang, W.; Xin, H. L.; Snyder, J. D.; Li, D.; Herron, J. A.; Mavrikakis, M.; Chi, M.; More, K. L.; Li, Y.; Markovic, N. M.; Somorjai, G. A.; Yang, P.; Stamenkovic, V. R. Highly Crystalline Multimetallic Nanoframes with Three-Dimensional Electrocatalytic Surfaces. *Science* **2014**, *343* (6177), 1339–1343. https://doi.org/10.1126/science.1249061.

(16) Stamenkovic, V.; Mun, B. S.; Mayrhofer, K. J. J.; Ross, P. N.; Markovic, N. M.; Rossmeisl, J.; Greeley, J.; Nørskov, J. K. Changing the Activity of Electrocatalysts for Oxygen Reduction by Tuning the Surface Electronic Structure. *Angewandte Chemie Int Ed* **2006**, *45* (18), 2897–2901. https://doi.org/10.1002/anie.200504386.

(17) Campbell, C. Bimetallic Surface Chemistry. *Annu Rev Phys Chem* **1990**, *41* (1), 775–837. https://doi.org/10.1146/annurev.physchem.41.1.775.

(18) Xiong, Y.; Yang, Y.; DiSalvo, F. J.; Abruña, H. D. Synergistic Bimetallic Metallic Organic Framework-Derived Pt–Co Oxygen Reduction Electrocatalysts. *Acs Nano* **2020**, *14* (10), 13069–13080. https://doi.org/10.1021/acsnano.0c04559.

(19) Wang, K.; Qin, Y.; Lv, F.; Li, M.; Liu, Q.; Lin, F.; Feng, J.; Yang, C.; Gao, P.; Guo, S. Intermetallic Pd3Pb Nanoplates Enhance Oxygen Reduction Catalysis with Excellent Methanol Tolerance. *Small Methods* **2018**, *2* (3), 1700331. https://doi.org/10.1002/smtd.201700331.

(20) Chong, L.; Wen, J.; Kubal, J.; Sen, F. G.; Zou, J.; Greeley, J.; Chan, M.; Barkholtz, H.; Ding, W.; Liu, D.-J. Ultralow-Loading Platinum-Cobalt Fuel Cell Catalysts Derived from Imidazolate Frameworks. *Science* **2018**, *362* (6420), eaau0630. https://doi.org/10.1126/science.aau0630.

(21) Liu, J.; Jiao, M.; Lu, L.; Barkholtz, H. M.; Li, Y.; Wang, Y.; Jiang, L.; Wu, Z.; Liu, D.; Zhuang, L.; Ma, C.; Zeng, J.; Zhang, B.; Su, D.; Song, P.; Xing, W.; Xu, W.; Wang, Y.; Jiang, Z.; Sun, G. High Performance Platinum Single Atom Electrocatalyst for Oxygen Reduction Reaction. *Nat Commun* **2017**, *8* (1), 15938. https://doi.org/10.1038/ncomms15938.

(22) Li, X.; Yang, X.; Huang, Y.; Zhang, T.; Liu, B. Supported Noble-Metal Single Atoms for Heterogeneous Catalysis. *Adv Mater* **2019**, *31* (50), 1902031. https://doi.org/10.1002/adma.201902031.

(23) Yi, J.; Xu, R.; Wu, Q.; Zhang, T.; Zang, K.; Luo, J.; Liang, Y.; Huang, Y.; Cao, R. Atomically Dispersed Iron–Nitrogen Active Sites within Porphyrinic Triazine-Based Frameworks for Oxygen Reduction Reaction in Both Alkaline and Acidic Media. *Acs Energy Lett* **2018**, *3* (4), 883–889. https://doi.org/10.1021/acsenergylett.8b00245.

(24) Shang, H.; Zhou, X.; Dong, J.; Li, A.; Zhao, X.; Liu, Q.; Lin, Y.; Pei, J.; Li, Z.; Jiang, Z.; Zhou, D.; Zheng, L.; Wang, Y.; Zhou, J.; Yang, Z.; Cao, R.; Sarangi, R.; Sun, T.; Yang, X.; Zheng, X.; Yan, W.; Zhuang, Z.; Li, J.; Chen, W.; Wang, D.; Zhang, J.; Li, Y. Engineering Unsymmetrically Coordinated Cu-S1N3 Single Atom Sites with Enhanced Oxygen Reduction Activity. *Nat Commun* **2020**, *11* (1), 3049. https://doi.org/10.1038/s41467-020-16848-8.

(25) Zeng, H.; Liu, X.; Chen, F.; Chen, Z.; Fan, X.; Lau, W. Single Atoms on a Nitrogen-Doped Boron Phosphide Monolayer: A New Promising Bifunctional Electrocatalyst for ORR and OER. *Acs Appl Mater Inter* **2020**, *12* (47), 52549–52559. https://doi.org/10.1021/acsami.0c13597.

(26) Zhang, Z.; Sun, J.; Wang, F.; Dai, L. Efficient Oxygen Reduction Reaction (ORR) Catalysts Based on Single Iron Atoms Dispersed on a Hierarchically Structured Porous Carbon Framework. *Angew Chem-ger Edit* **2018**, *130* (29), 9176–9181. https://doi.org/10.1002/ange.201804958.

(27) Zitolo, A.; Ranjbar-Sahraie, N.; Mineva, T.; Li, J.; Jia, Q.; Stamatin, S.; Harrington, G. F.; Lyth, S. M.; Krtil, P.; Mukerjee, S.; Fonda, E.; Jaouen, F. Identification of Catalytic Sites in Cobalt-Nitrogen-Carbon Materials for the Oxygen Reduction Reaction. *Nat Commun* **2017**, *8* (1), 957. https://doi.org/10.1038/s41467-017-01100-7.

(28) Chen, J.; Li, H.; Fan, C.; Meng, Q.; Tang, Y.; Qiu, X.; Fu, G.; Ma, T. Dual Single-Atomic Ni-N4 and Fe-N4 Sites Constructing Janus Hollow Graphene for Selective Oxygen Electrocatalysis. *Adv Mater* **2020**, *32* (30), 2003134. https://doi.org/10.1002/adma.202003134.

(29) Lu, B.; Smart, T.; Qin, D.; Lu, J.; Wang, N.; Chen, L.; Peng, Y.; Ping, Y.; Chen, S. Nitrogen and Iron-Codoped Carbon Hollow Nanotubules as High-Performance Catalysts toward Oxygen Reduction Reaction: A Combined Experimental and Theoretical Study. *Chem Mater* **2017**, *29* (13), 5617–5628. https://doi.org/10.1021/acs.chemmater.7b01265.

(30) Mercado, R.; Wahl, C.; Lu, J. E.; Zhang, T.; Lu, B.; Zhang, P.; Lu, J. Q.; Allen, A.; Zhang, J. Z.; Chen, S. Nitrogen-Doped Porous Carbon Cages for Electrocatalytic Reduction of Oxygen: Enhanced Performance with Iron and Cobalt Dual Metal Centers. *Chemcatchem* **2020**, *12* (12), 3230–3239. https://doi.org/10.1002/cctc.201902324.

(31) Sarapuu, A.; Samolberg, L.; Kreek, K.; Koel, M.; Matisen, L.; Tammeveski, K. Cobalt- and Iron-Containing Nitrogen-Doped Carbon Aerogels as Non-Precious Metal Catalysts for Electrochemical Reduction of Oxygen. *J Electroanal Chem* **2015**, *746*, 9–17. https://doi.org/10.1016/j.jelechem.2015.03.021.

(32) Bezerra, C. W. B.; Zhang, L.; Lee, K.; Liu, H.; Marques, A. L. B.; Marques, E. P.; Wang, H.; Zhang, J. A Review of Fe–N/C and Co–N/C Catalysts for the Oxygen Reduction Reaction. *Electrochim Acta* **2008**, *53* (15), 4937–4951. https://doi.org/10.1016/j.electacta.2008.02.012.

(33) He, Y.; Liu, S.; Priest, C.; Shi, Q.; Wu, G. Atomically Dispersed Metal–Nitrogen–Carbon Catalysts for Fuel Cells: Advances in Catalyst Design, Electrode Performance, and Durability Improvement. *Chem Soc Rev* **2020**, *49* (11), 3484–3524. https://doi.org/10.1039/c9cs00903e.

(34) Talapaneni, S. N.; Singh, G.; Kim, I. Y.; AlBahily, K.; Al-Muhtaseb, A. H.; Karakoti, A. S.; Tavakkoli, E.; Vinu, A. Carbon Capture and Conversion: Nanostructured Carbon Nitrides for CO2 Capture and Conversion (Adv. Mater. 18/2020). *Adv Mater* **2020**, *32* (18), 2070142. https://doi.org/10.1002/adma.202070142.

(35) Chen, S.; Qiu, L.; Cheng, H.-M. Carbon-Based Fibers for Advanced Electrochemical Energy Storage Devices. *Chem Rev* **2020**, *120* (5), 2811–2878. https://doi.org/10.1021/acs.chemrev.9b00466.

(36) He, L.; Weniger, F.; Neumann, H.; Beller, M. Synthesis, Characterization, and Application of Metal Nanoparticles Supported on Nitrogen-Doped Carbon: Catalysis beyond Electrochemistry. *Angewandte Chemie Int Ed* **2016**, *55* (41), 12582–12594. https://doi.org/10.1002/anie.201603198.

(37) Yang, W.; Li, X.; Li, Y.; Zhu, R.; Pang, H. Applications of Metal–Organic-Framework-Derived Carbon Materials. *Adv Mater* **2019**, *31* (6), 1804740. https://doi.org/10.1002/adma.201804740.

(38) Benzigar, M. R.; Talapaneni, S. N.; Joseph, S.; Ramadass, K.; Singh, G.; Scaranto, J.; Ravon, U.; Al-Bahily, K.; Vinu, A. Recent Advances in Functionalized Micro and Mesoporous

Carbon Materials: Synthesis and Applications. *Chem Soc Rev* **2018**, *47* (8), 2680–2721. https://doi.org/10.1039/c7cs00787f.

(39) Zhao, X.; Zhang, Y.; Zhao, X.; Wang, X.; Zhao, Y.; Tan, H.; Zhu, H.; Ho, W.; Sun, H.; Li, Y. Urea and Melamine Formaldehyde Resin-Derived Tubular g-C 3 N 4 with Highly Efficient Photocatalytic Performance. *Acs Appl Mater Inter* **2019**, *11* (31), 27934–27943. https://doi.org/10.1021/acsami.9b08483.

(40) Ding, L.; Zhang, M.; Ren, Y.; Xu, J.; Zheng, J.; Alsulami, H.; Kutbi, M. A.; Zhang, F.-Y. Carbon-Supported Nickel Nanoparticles on SiO 2 Cores for Protein Adsorption and Nitroaromatics Reduction. *Acs Appl Nano Mater* **2020**, *3* (5), 4623–4634. https://doi.org/10.1021/acsanm.0c00656.

(41) Hwang, J.; Walczak, R.; Oschatz, M.; Tarakina, N. V.; Schmidt, B. V. K. J. Micro-Blooming: Hierarchically Porous Nitrogen-Doped Carbon Flowers Derived from Metal-Organic Mesocrystals. *Small* **2019**, *15* (37), 1901986. https://doi.org/10.1002/smll.201901986.

(42) Feng, J.; Tang, R.; Wang, X.; Meng, T. Biomass-Derived Activated Carbon Sheets with Tunable Oxygen Functional Groups and Pore Volume for High-Performance Oxygen Reduction and Zn–Air Batteries. *Acs Appl Energy Mater* **2021**, *4* (5), 5230–5236. https://doi.org/10.1021/acsaem.1c00755.

(43) Zhu, C.; Li, H.; Fu, S.; Du, D.; Lin, Y. Highly Efficient Nonprecious Metal Catalysts towards Oxygen Reduction Reaction Based on Three-Dimensional Porous Carbon Nanostructures. *Chem Soc Rev* **2015**, *45* (3), 517–531. https://doi.org/10.1039/c5cs00670h.

(44) Hu, X.; Wu, Y.; Li, H.; Zhang, Z. Adsorption and Activation of O 2 on Nitrogen-Doped Carbon Nanotubes. *J Phys Chem C* **2010**, *114* (21), 9603–9607. https://doi.org/10.1021/jp1000013.

(45) Xia, Y.; Mokaya, R. Generalized and Facile Synthesis Approach to N-Doped Highly Graphitic Mesoporous Carbon Materials. *Chem Mater* **2005**, *17* (6), 1553–1560. https://doi.org/10.1021/cm048057y.

(46) Wang, H.; Maiyalagan, T.; Wang, X. Review on Recent Progress in Nitrogen-Doped Graphene: Synthesis, Characterization, and Its Potential Applications. *Acs Catal* **2012**, *2* (5), 781–794. https://doi.org/10.1021/cs200652y.

(47) Wei, Q.; Tong, X.; Zhang, G.; Qiao, J.; Gong, Q.; Sun, S. Nitrogen-Doped Carbon Nanotube and Graphene Materials for Oxygen Reduction Reactions. *Catalysts* **2015**, *5* (3), 1574–1602. https://doi.org/10.3390/catal5031574.

(48) Fernandez-Escamilla, H. N.; Guerrero-Sanchez, J.; Contreras, E.; Ruiz-Marizcal, J. M.; Alonso-Nunez, G.; Contreras, O. E.; Felix-Navarro, R. M.; Romo-Herrera, J. M.; Takeuchi, N. Understanding the Selectivity of the Oxygen Reduction Reaction at the Atomistic Level on Nitrogen-Doped Graphitic Carbon Materials. *Adv Energy Mater* **2021**, *11* (3), 2002459. https://doi.org/10.1002/aenm.202002459.

(49) Zhang, J.; Dai, L. Heteroatom-Doped Graphitic Carbon Catalysts for Efficient Electrocatalysis of Oxygen Reduction Reaction. *Acs Catal* **2015**, *5* (12), 7244–7253. https://doi.org/10.1021/acscatal.5b01563.

(50) Zhang, H.; Hwang, S.; Wang, M.; Feng, Z.; Karakalos, S.; Luo, L.; Qiao, Z.; Xie, X.; Wang, C.; Su, D.; Shao, Y.; Wu, G. Single Atomic Iron Catalysts for Oxygen Reduction in

Acidic Media: Particle Size Control and Thermal Activation. *J Am Chem Soc* **2017**, *139* (40), 14143–14149. https://doi.org/10.1021/jacs.7b06514.

(51) Jiang, L.; Duan, J.; Zhu, J.; Chen, S.; Antonietti, M. Iron-Cluster-Directed Synthesis of 2D/2D Fe–N–C/MXene Superlattice-like Heterostructure with Enhanced Oxygen Reduction Electrocatalysis. *Acs Nano* **2020**, *14* (2), 2436–2444. https://doi.org/10.1021/acsnano.9b09912.

(52) Li, J.-C.; Xiao, F.; Zhong, H.; Li, T.; Xu, M.; Ma, L.; Cheng, M.; Liu, D.; Feng, S.; Shi, Q.; Cheng, H.-M.; Liu, C.; Du, D.; Beckman, S. P.; Pan, X.; Lin, Y.; Shao, M. Secondary-Atom-Assisted Synthesis of Single Iron Atoms Anchored on N-Doped Carbon Nanowires for Oxygen Reduction Reaction. *Acs Catal* **2019**, *9* (7), 5929–5934. https://doi.org/10.1021/acscatal.9b00869.

(53) Collman, J. P.; Devaraj, N. K.; Decréau, R. A.; Yang, Y.; Yan, Y.-L.; Ebina, W.; Eberspacher, T. A.; Chidsey, C. E. D. A Cytochrome c Oxidase Model Catalyzes Oxygen to Water Reduction Under Rate-Limiting Electron Flux. *Science* **2007**, *315* (5818), 1565–1568. https://doi.org/10.1126/science.1135844.

(54) JASINSKI, R. A New Fuel Cell Cathode Catalyst. *Nature* **1964**, *201* (4925), 1212–1213. https://doi.org/10.1038/2011212a0.

(55) Gupta, S.; Tryk, D.; Bae, I.; Aldred, W.; Yeager, E. Heat-Treated Polyacrylonitrile-Based Catalysts for Oxygen Electroreduction. *J Appl Electrochem* **1989**, *19* (1), 19–27. https://doi.org/10.1007/bf01039385.

(56) Lefèvre, M.; Proietti, E.; Jaouen, F.; Dodelet, J.-P. Iron-Based Catalysts with Improved Oxygen Reduction Activity in Polymer Electrolyte Fuel Cells. *Science* **2009**, *324* (5923), 71–74. https://doi.org/10.1126/science.1170051.

(57) Jia, Q.; Ramaswamy, N.; Hafiz, H.; Tylus, U.; Strickland, K.; Wu, G.; Barbiellini, B.; Bansil, A.; Holby, E. F.; Zelenay, P.; Mukerjee, S. Experimental Observation of Redox-Induced Fe–N Switching Behavior as a Determinant Role for Oxygen Reduction Activity. *Acs Nano* **2015**, *9* (12), 12496–12505. https://doi.org/10.1021/acsnano.5b05984.

(58) Ramaswamy, N.; Tylus, U.; Jia, Q.; Mukerjee, S. Activity Descriptor Identification for Oxygen Reduction on Nonprecious Electrocatalysts: Linking Surface Science to Coordination Chemistry. *J Am Chem Soc* **2013**, *135* (41), 15443–15449. https://doi.org/10.1021/ja405149m.

(59) Collman, J. P.; Denisevich, P.; Konai, Y.; Marrocco, M.; Koval, C.; Anson, F. C. Electrode Catalysis of the Four-Electron Reduction of Oxygen to Water by Dicobalt Face-to-Face Porphyrins. *J Am Chem Soc* **1980**, *102* (19), 6027–6036. https://doi.org/10.1021/ja00539a009.

(60) Ganesan, S.; Leonard, N.; Barton, S. C. Impact of Transition Metal on Nitrogen Retention and Activity of Iron–Nitrogen–Carbon Oxygen Reduction Catalysts. *Phys Chem Chem Phys* **2014**, *16* (10), 4576–4585. https://doi.org/10.1039/c3cp54751e.

(61) Yang, X.; Xia, D.; Kang, Y.; Du, H.; Kang, F.; Gan, L.; Li, J. Unveiling the Axial Hydroxyl Ligand on Fe□N4□C Electrocatalysts and Its Impact on the PH-Dependent Oxygen Reduction Activities and Poisoning Kinetics. *Adv Sci* **2020**, *7* (12), 2000176. https://doi.org/10.1002/advs.202000176.

(62) Niu, W.; Li, L.; Liu, X.; Wang, N.; Liu, J.; Zhou, W.; Tang, Z.; Chen, S. Mesoporous N-Doped Carbons Prepared with Thermally Removable Nanoparticle Templates: An Efficient Electrocatalyst for Oxygen Reduction Reaction. *J Am Chem Soc* **2015**, *137* (16), 5555–5562. https://doi.org/10.1021/jacs.5b02027.

(63) Wang, N.; Lu, B.; Li, L.; Niu, W.; Tang, Z.; Kang, X.; Chen, S. Graphitic Nitrogen Is Responsible for Oxygen Electroreduction on Nitrogen-Doped Carbons in Alkaline Electrolytes: Insights from Activity Attenuation Studies and Theoretical Calculations. *Acs Catal* **2018**, *8* (8), 6827–6836. https://doi.org/10.1021/acscatal.8b00338.

(64) Ning, F.; He, X.; Shen, Y.; Jin, H.; Li, Q.; Li, D.; Li, S.; Zhan, Y.; Du, Y.; Jiang, J.; Yang, H.; Zhou, X. Flexible and Lightweight Fuel Cell with High Specific Power Density. *Acs Nano* **2017**, *11* (6), 5982–5991. https://doi.org/10.1021/acsnano.7b01880.

(65) Jahan, M.; Liu, Z.; Loh, K. P. A Graphene Oxide and Copper-Centered Metal Organic Framework Composite as a Tri-Functional Catalyst for HER, OER, and ORR. *Adv Funct Mater* **2013**, *23* (43), 5363–5372. https://doi.org/10.1002/adfm.201300510.

(66) Men, B.; Sun, Y.; Li, M.; Hu, C.; Zhang, M.; Wang, L.; Tang, Y.; Chen, Y.; Wan, P.; Pan, J. Hierarchical Metal-Free Nitrogen-Doped Porous Graphene/Carbon Composites as an Efficient Oxygen Reduction Reaction Catalyst. *Acs Appl Mater Inter* **2016**, *8* (2), 1415–1423. https://doi.org/10.1021/acsami.5b10642.

(67) Behan, J. A.; Mates-Torres, E.; Stamatin, S. N.; Domínguez, C.; Iannaci, A.; Fleischer, K.; Hoque, Md. K.; Perova, T. S.; García-Melchor, M.; Colavita, P. E. Untangling Cooperative Effects of Pyridinic and Graphitic Nitrogen Sites at Metal-Free N-Doped Carbon Electrocatalysts for the Oxygen Reduction Reaction. *Small* **2019**, *15* (48), 1902081. https://doi.org/10.1002/smll.201902081.

(68) Gebremariam, T. T.; Chen, F.; Jin, Y.; Wang, Q.; Wang, J.; Wang, J. Bimetallic NiCo/CNF Encapsulated in a N-Doped Carbon Shell as an Electrocatalyst for Zn–Air Batteries and Water Splitting. *Catal Sci Technol* **2019**, *9* (10), 2532–2542. https://doi.org/10.1039/c9cy00266a.

(69) Gong, K.; Du, F.; Xia, Z.; Durstock, M.; Dai, L. Nitrogen-Doped Carbon Nanotube Arrays with High Electrocatalytic Activity for Oxygen Reduction. *Sci New York N Y* **2009**, *323* (5915), 760–764. https://doi.org/10.1126/science.1168049.

(70) Gu, D.; Zhou, Y.; Ma, R.; Wang, F.; Liu, Q.; Wang, J. Facile Synthesis of N-Doped Graphene-Like Carbon Nanoflakes as Efficient and Stable Electrocatalysts for the Oxygen Reduction Reaction. *Nano-micro Lett* **2017**, *10* (2), 29. https://doi.org/10.1007/s40820-017-0181-1.

(71) Sideri, I. K.; Tagmatarchis, N. Noble-Metal-Free Doped Carbon Nanomaterial Electrocatalysts. *Chem European J* **2020**, *26* (67), 15397–15415. https://doi.org/10.1002/chem.202003613.

(72) Luo, F.; Roy, A.; Silvioli, L.; Cullen, D. A.; Zitolo, A.; Sougrati, M. T.; Oguz, I. C.; Mineva, T.; Teschner, D.; Wagner, S.; Wen, J.; Dionigi, F.; Kramm, U. I.; Rossmeisl, J.; Jaouen, F.; Strasser, P. P-Block Single-Metal-Site Tin/Nitrogen-Doped Carbon Fuel Cell Cathode Catalyst for Oxygen Reduction Reaction. *Nat Mater* **2020**, *19* (11), 1215–1223. https://doi.org/10.1038/s41563-020-0717-5.

(73) Yang, Z.; Zhao, C.; Qu, Y.; Zhou, H.; Zhou, F.; Wang, J.; Wu, Y.; Li, Y. Trifunctional Self-Supporting Cobalt-Embedded Carbon Nanotube Films for ORR, OER, and HER Triggered by Solid Diffusion from Bulk Metal. *Adv Mater* **2019**, *31* (12), 1808043. https://doi.org/10.1002/adma.201808043.

(74) Kuk, Y.; Ahmed, S.; Sun, H.; Shim, J.; Park, G. Synthesis of Porous Carbon-coated Cobalt Catalyst through Pyrolyzing Metal–Organic Framework and Their Bifunctional OER/ORR Catalytic Activity for Zn-Air Rechargeable Batteries. *B Korean Chem Soc* **2020**, *41* (3), 310–316. https://doi.org/10.1002/bkcs.11973.

(75) Guo, Y.; Yuan, P.; Zhang, J.; Xia, H.; Cheng, F.; Zhou, M.; Li, J.; Qiao, Y.; Mu, S.; Xu, Q. Co2P–CoN Double Active Centers Confined in N-Doped Carbon Nanotube: Heterostructural Engineering for Trifunctional Catalysis toward HER, ORR, OER, and Zn–Air Batteries Driven Water Splitting. *Adv Funct Mater* **2018**, *28* (51), 1805641. https://doi.org/10.1002/adfm.201805641.

(76) Liu, X.; Jiao, Y.; Zheng, Y.; Jaroniec, M.; Qiao, S.-Z. Building Up a Picture of the Electrocatalytic Nitrogen Reduction Activity of Transition Metal Single-Atom Catalysts. *J Am Chem Soc* **2019**, *141* (24), 9664–9672. https://doi.org/10.1021/jacs.9b03811.

(77) Hou, C.; Zou, L.; Sun, L.; Zhang, K.; Liu, Z.; Li, Y.; Li, C.; Zou, R.; Yu, J.; Xu, Q. Single-Atom Iron Catalysts on Overhang-Eave Carbon Cages for High-Performance Oxygen Reduction Reaction. *Angewandte Chemie Int Ed* **2020**, *59* (19), 7384–7389. https://doi.org/10.1002/anie.202002665.

(78) Zhu, Z.; Zhai, Y.; Dong, S. Facial Synthesis of PtM (M = Fe, Co, Cu, Ni) Bimetallic Alloy Nanosponges and Their Enhanced Catalysis for Oxygen Reduction Reaction. *Acs Appl Mater Inter* **2014**, *6* (19), 16721–16726. https://doi.org/10.1021/am503689t.

(79) Lee, J.-S. M.; Fujiwara, Y.; Kitagawa, S.; Horike, S. Homogenized Bimetallic Catalysts from Metal–Organic Framework Alloys. *Chem Mater* **2019**, *31* (11), 4205–4212. https://doi.org/10.1021/acs.chemmater.9b01093.

(80) Yuan, S.; Cui, L.; Dou, Z.; Ge, X.; He, X.; Zhang, W.; Asefa, T. Nonprecious Bimetallic Sites Coordinated on N-Doped Carbons with Efficient and Durable Catalytic Activity for Oxygen Reduction. *Small* **2020**, *16* (40), 2000742. https://doi.org/10.1002/smll.202000742.

(81) Sarkar, S.; Biswas, A.; Purkait, T.; Das, M.; Kamboj, N.; Dey, R. S. Unravelling the Role of Fe–Mn Binary Active Sites Electrocatalyst for Efficient Oxygen Reduction Reaction and

Rechargeable Zn-Air Batteries. *Inorg Chem* **2020**, *59* (7), 5194–5205. https://doi.org/10.1021/acs.inorgchem.0c00446.

(82) Zhu, Z.; Yin, H.; Wang, Y.; Chuang, C.; Xing, L.; Dong, M.; Lu, Y.; Casillas-Garcia, G.; Zheng, Y.; Chen, S.; Dou, Y.; Liu, P.; Cheng, Q.; Zhao, H. Coexisting Single-Atomic Fe and Ni Sites on Hierarchically Ordered Porous Carbon as a Highly Efficient ORR Electrocatalyst. *Adv Mater* **2020**, *32* (42), 2004670. https://doi.org/10.1002/adma.202004670.

(83) Koshy, D. M.; Chen, S.; Lee, D. U.; Stevens, M. B.; Abdellah, A. M.; Dull, S. M.; Chen, G.; Nordlund, D.; Gallo, A.; Hahn, C.; Higgins, D. C.; Bao, Z.; Jaramillo, T. F. Understanding the Origin of Highly Selective CO2 Electroreduction to CO on Ni,N-doped Carbon Catalysts. *Angewandte Chemie Int Ed* **2020**, *59* (10), 4043–4050. https://doi.org/10.1002/anie.201912857.

(84) Chen, S.; Koshy, D. M.; Tsao, Y.; Pfattner, R.; Yan, X.; Feng, D.; Bao, Z. Highly Tunable and Facile Synthesis of Uniform Carbon Flower Particles. *J Am Chem Soc* **2018**, *140* (32), 10297–10304. https://doi.org/10.1021/jacs.8b05825.

(85) Xing, Z.; Qi, Y.; Tian, Z.; Xu, J.; Yuan, Y.; Bommier, C.; Lu, J.; Tong, W.; Jiang, D.; Ji, X. Identify the Removable Substructure in Carbon Activation. *Chem Mater* **2017**, *29* (17), 7288–7295. https://doi.org/10.1021/acs.chemmater.7b01937.

(86) Wang, X.; Jia, Y.; Mao, X.; Liu, D.; He, W.; Li, J.; Liu, J.; Yan, X.; Chen, J.; Song, L.; Du, A.; Yao, X. Edge-Rich Fe−N4 Active Sites in Defective Carbon for Oxygen Reduction Catalysis. *Adv Mater* **2020**, *32* (16), 2000966. https://doi.org/10.1002/adma.202000966.

(87) Liu, D.; Jia, B.; Liu, X.; Zhao, B.; Gao, J.; Cao, Q.; Wu, S.; Qin, Y. Effects of Oxygen Functional Groups and FeCl 3 on the Evolution of Physico-Chemical Structure in Activated

Carbon Obtained from Jixi Bituminous Coal. *Rsc Adv* **2018**, *8* (16), 8569–8579. https://doi.org/10.1039/c7ra12928a.

(88) Sarhan, A. A. O.; Bolm, C. Iron(Iii) Chloride in Oxidative C–C Coupling Reactions. *Chem Soc Rev* **2009**, *38* (9), 2730–2744. https://doi.org/10.1039/b906026j.

(89) Lu, S.; Jin, M.; Zhang, Y.; Niu, Y.; Gao, J.; Li, C. M. Chemically Exfoliating Biomass into a Graphene-like Porous Active Carbon with Rational Pore Structure, Good Conductivity, and Large Surface Area for High-Performance Supercapacitors. *Adv Energy Mater* **2018**, *8* (11), 1702545. https://doi.org/10.1002/aenm.201702545.

(90) Zhu, J.; Li, W.; Li, S.; Zhang, J.; Zhou, H.; Zhang, C.; Zhang, J.; Mu, S. Defective N/S-Codoped 3D Cheese-Like Porous Carbon Nanomaterial toward Efficient Oxygen Reduction and Zn–Air Batteries. *Small* **2018**, *14* (21), 1800563. https://doi.org/10.1002/smll.201800563.

(91) He, T.; Peng, Y.; Li, Q.; Lu, J. E.; Liu, Q.; Mercado, R.; Chen, Y.; Nichols, F.; Zhang, Y.; Chen, S. Nanocomposites Based on Ruthenium Nanoparticles Supported on Cobalt and Nitrogen-Codoped Graphene Nanosheets as Bifunctional Catalysts for Electrochemical Water Splitting. *Acs Appl Mater Inter* **2019**, *11* (50), 46912–46919. https://doi.org/10.1021/acsami.9b17056.

(92) Liu, Q.; Peng, Y.; Li, Q.; He, T.; Morris, D.; Nichols, F.; Mercado, R.; Zhang, P.; Chen, S. Atomic Dispersion and Surface Enrichment of Palladium in Nitrogen-Doped Porous Carbon Cages Lead to High-Performance Electrocatalytic Reduction of Oxygen. *Acs Appl Mater Inter* **2020**, *12* (15), 17641–17650. https://doi.org/10.1021/acsami.0c03415.

(93) He, T.; Zhang, Y.; Chen, Y.; Zhang, Z.; Wang, H.; Hu, Y.; Liu, M.; Pao, C.-W.; Chen, J.-L.; Chang, L. Y.; Sun, Z.; Xiang, J.; Zhang, Y.; Chen, S. Single Iron Atoms Stabilized by Microporous Defects of Biomass-Derived Carbon Aerogels as High-Performance Cathode

Electrocatalysts for Aluminum–Air Batteries. *J Mater Chem A* **2019**, *7* (36), 20840–20846. https://doi.org/10.1039/c9ta05981d.

(94) Morales, D. M.; Kazakova, M. A.; Dieckhöfer, S.; Selyutin, A. G.; Golubtsov, G. V.; Schuhmann, W.; Masa, J. Trimetallic Mn-Fe-Ni Oxide Nanoparticles Supported on Multi-Walled Carbon Nanotubes as High-Performance Bifunctional ORR/OER Electrocatalyst in Alkaline Media. *Adv Funct Mater* **2020**, *30* (6), 1905992. https://doi.org/10.1002/adfm.201905992.

(95) Liu, C.; Li, H.; Chen, J.; Yu, Z.; Ru, Q.; Li, S.; Henkelman, G.; Wei, L.; Chen, Y. 3d Transition-Metal-Mediated Columbite Nanocatalysts for Decentralized Electrosynthesis of Hydrogen Peroxide. *Small* **2021**, *17* (13), 2007249. https://doi.org/10.1002/smll.202007249.

(96) Grosvenor, A.; Kobe, B.; Biesinger, M.; McIntyre, N. Investigation of Multiplet Splitting of Fe 2p XPS Spectra and Bonding in Iron Compounds. *Surf Interface Anal* **2004**, *36* (12), 1564–1574. https://doi.org/10.1002/sia.1984.

(97) Grosvenor, A. P.; Biesinger, M. C.; Smart, R. St. C.; McIntyre, N. S. New Interpretations of XPS Spectra of Nickel Metal and Oxides. *Surf Sci* **2006**, *600* (9), 1771–1779. https://doi.org/10.1016/j.susc.2006.01.041.

(98) Varnell, J.; Tse, E.; Schulz, C.; Fister, T.; Haasch, R.; Timoshenko, J.; Frenkel, A.; Gewirth, A. Identification of Carbon-Encapsulated Iron Nanoparticles as Active Species in Non-Precious Metal Oxygen Reduction Catalysts. *Nat Commun* **2016**, *7* (1), 12582. https://doi.org/10.1038/ncomms12582.

2. Nitrogen-Doped Porous Carbon Cages for Electrocatalytic Reduction of Oxygen: Enhanced Performance with Iron and Cobalt Dual Metal Centers

2.1 Abstract

The unique electronic structures of heteroatom-doped carbon materials make them promising electrocatalysts towards the oxygen reduction reaction (ORR). In this study, dual-metal (Fe an Co) and nitrogen-codoped porous carbon cages (CHS-FeCo) were synthesized by controlled pyrolysis of a melamine-formaldehyde resin embedded with iron and cobalt precursors at varying ratios with silica nanoparticles as rigid templates. Transmission electron microscopy measurements confirmed the formation of hollow carbon cages and the absence of metal (oxide) nanoparticles suggested atomic dispersion of the metal species within the carbon skeletons. X-ray photoelectron spectroscopic analysis revealed an elemental composition of mostly carbon, oxygen, and nitrogen, with a total metal content of about 1 at%. Electrochemically, the dual-metal ones showed a significant enhancement of the catalytic performance towards ORR in alkaline media, as compared to samples with single or no metal dopants. This was accounted for by the synergistic interaction between the Fe and Co centers in the carbon samples, as evidenced in X-ray absorption spectroscopic studies. Remarkably, the CHS-FeCo sample even exhibited apparent resistance against KSCN poisoning, where XPS analysis revealed oxidation of KSCN and no metal-sulfur interaction, in sharp contrast to the monometal counterparts which were easily poisoned. Results from this study suggest that the synergistic interactions between dual metal centers may be exploited for enhanced ORR performance of carbon-based nanocomposite catalysts.

2.2 Introduction

In recent decades, proton exchange membrane fuel cells (PEMFCs) have gained a great deal of attention as potential power sources for diverse applications, not only due to their emission-free operation and utilization of non-fossil fuels, but also because hydrogen has a significantly higher energy density than regular gasoline and PEMFCs have a greater theoretical efficiency than combustion engines.[1] In order to achieve the efficiency, the electrochemical reactions taking place in the cell must do so with fast kinetics at low overpotentials. In PEMFCs, the oxygen reduction reaction (ORR) at the cathode has notoriously sluggish kinetics, and does hardly occur without effective catalysts, making this reaction a major obstacle for the large-scale commercialization of fuel cell technology.[2] Platinum-based catalysts have been shown to provide the necessary catalytic activity at sufficiently high mass loadings, but its low abundance and prohibitive cost limits their use in commercial settings.[3] A range of strategies have been examined to improve the ORR activity of Pt nanoparticles, which usually involve the manipulation of size, composition, and surface atomic arrangements of the catalysts.[4,5] In addition, extensive research efforts have also been devoted to the design and engineering of Pt-free catalysts. Of these, carbon-based materials have received increasing attention, as recent studies have shown that carbon nanomaterials, such as carbon nanotubes, graphene oxide, and carbon spheres, can be an efficient, low-cost, metal-free alternative to Pt for ORR.[6-8] While pristine carbon materials are unable to achieve an activity comparable to that of commercial Pt, heteroatom dopants, such as nitrogen, are known to modulate the electronic properties and surface polarities of the carbon skeleton, and have been shown to greatly increase the ORR activity.[9] This is primarily because heteroatom doping induces a charge redistribution, thereby facilitating the adsorption of oxygen.[10]

With the embedment of select transition metal elements into the carbon skeletons, the ORR activity can be markedly enhanced.[11,12] Promising non-noble transition metals, such as iron, cobalt, nickel, and manganese, have been used in the design of carbon-based ORR

catalysts, and are believed to make an essential contribution to the overall activity,[13-16] which is mostly ascribed to the formation of metal-nitrogen-carbon (MNC) coordinated structures, the so-called single atom catalysts.[15-18] In these studies, the catalysts are generally prepared by controlled pyrolysis of metal and heteroatom-containing precursors,[19-25] and the ORR active sites are formed as the result of a series of heat treatment and etching steps.[14,16,19] It is now broadly accepted that nitrogen-carbon structures that are active for ORR include various kinds of nitrogen defects in the carbon matrix, replacing sp^2-hybridized carbon atoms either at the edges (pyrrolic and pyridinic) or within the skeleton (graphitic); and the nitrogen dopants may serve as the coordinating environment for metal ions, forming the presumed active center MN_x for ORR.[26-29]

Interestingly, the ORR activity can be further enhanced by incorporating dual metal dopants into the carbon matrix (e.g., Fe, Co, Pt, Pd, and Ni),[30-32] where the synergistic interactions between the metal centers can be exploited to facilitate the adsorption and reduction of oxygen intermediates,[33] and it has recently been demonstrated that bimetallic systems such as iron and cobalt are among the most promising for the electroreduction of oxygen.[22] In carbon materials, FeN_x sites have been proposed as the active sites,[34-36] where the high spin state of iron is particularly attractive.[37] In addition to this, the enhanced corrosion resistance of cobalt[38,39] can have an influence on ORR in both acid and alkaline media. In a recent study,[40] Fe and Co were both incorporated in a mesoporous porphyrinic carbon structure (OMPCs), which exhibited an ORR activity that was markedly better than those of the monometal ones and comparable to Pt in acidic environments. This was ascribed to the bimetal interaction that had a synergistic effect on FeCo-OMPCs, which resulted in a weakened interaction with oxygen, as compared to the monometal OMPCs and Pt.

The porosity of the catalyst materials is another important parameter that can impact the accessibility to the catalytic active centers and mass transfer of reaction species, and hence the ORR activity.[41] This can be manipulated by using select structural templates.[34,42-47] In this

study, we report the preparation of porous carbon cages codoped with nitrogen and dual metals of Fe and Co, and observed a remarkable ORR activity in alkaline media, as compared to the metal-free samples or samples doped with a single metal species, which was accounted for by the synergistic interactions between the Fe and Co centers in the carbon matrix. In addition, the Fe,Co-codoped carbon catalysts were found to exhibit apparent resistance against KSCN poisoning, in sharp contrast to the monometal counterparts that could be easily poisoned by KSCN.

2.3 Experimental Section

2.3.1 Chemicals

Tetraethyl orthosilicate (TEOS, 98%, Acros Organics), ammonium hydroxide (NH_4OH, 28%, Fisher Scientific), reagent alcohol (EtOH, absolute, Macron Fine Chemicals), melamine (99%, Acros Organics), formaldehyde (37% v/v, Acros Organics), sodium hydroxide (NaOH, Fisher Scientific), ferrous sulfate heptahydrate ($FeSO_4 \cdot 7H_2O$, Fisher Scientific), ferrous chloride tetrahydrate ($FeCl_2 \cdot 4H_2O$, Fisher Scientific), iron(III) acetylacetonate ($Fe(acac)_3$, Acros organics), ferric chloride hexahydrate ($FeCl_3 \cdot 6H_2O$, Fisher Scientific), cobalt(II) chloride hexahydrate ($CoCl_2 \cdot 6H_2O$, Fisher Scientific), hydrofluoric acid (HF, 48%, Fisher Scientific), and Pt/C (20 wt%, Alfa Aesar) were all used as received. Water was supplied from a Barnstead Nanopure Water System (18.3 MΩ cm).

2.3.2 Synthesis of silica nanoparticles

SiO_2 nanoparticles were synthesized by adopting a literature procedure.[48] Typically, 16 mL of NH_4OH and 0.6 mL of TEOS were added into 240 mL of EtOH to form a clear solution, which was magnetically stirred for 16 h at room temperature. The product (SiO_2 nanoparticles) was collected by centrifugation, vacuum dried, and stored for future use.

2.3.3 Synthesis of melamine-formaldehyde resin coated silica nanoparticles

A melamine-formaldehyde resin coating layer was grown onto the SiO_2 nanoparticles prepared above.[47] In a typical synthesis, 0.189 g of melamine was dissolved in 30 mL of H_2O

at 90 °C, into which were added 12.5 mg of SiO_2 nanoparticles, 795 μL of formaldehyde, and a catalytic amount of NaOH, and the mixture was stirred overnight. The product was collected by centrifugation and vacuum dried to yield melamine-formaldehyde resin coated silica nanoparticles (SiO_2@MF).

2.3.4 Synthesis of dual-metal and nitrogen-codoped hollow carbon spheres

The SiO_2@MF obtained above was then used to prepare dual metals and nitrogen-doped hollow carbon spheres.[49] In brief, 50.0 mg of SiO_2@MF was soaked for several hours in an aqueous solution containing $FeSO_4$ and $CoCl_2$ at varied concentrations. The product was centrifuged and vacuum dried before being placed in a tube furnace and heated to 800°C for 1 h in a N_2 atmosphere at the heating rate of 10 °C/min (800°C was identified as the optimal temperature, not shown). The obtained black powder was stirred in a 10% HF solution to remove the SiO_2 templates, yielding dual-metal and nitrogen-codoped porous carbon cages. Three samples were prepared at varied Co loadings, denoted as CHS-FeCo(1), CHS-FeCo(2), and CHS-FeCo(3).

Six control samples were also prepared in the same manner. The first one (CHS) was derived directly by pyrolysis of SiO_2@MF without the soaking in any salt solution. The second sample (CHS-Fe) was prepared by soaking SiO_2@MF in a solution containing only $FeSO_4$; the third one (CHS-Co) was prepared by soaking SiO_2@MF in the solution contained only $CoCl_2$. The fourth sample (CHS-$FeCo_{FeCl2}$) was prepared by soaking SiO_2@MF in a solution containing $FeCl_2$ and $CoCl_2$. The fifth sample (CHS-$FeCo_{FeCl3}$) was prepared by soaking SiO_2@MF in a solution containing $FeCl_3$ and $CoCl_2$; and the sixth sample (CHS-$FeCo_{Fe(acac)3}$) was prepared by soaking SiO_2@MF in a solution containing $Fe(acac)_3$ and $CoCl_2$.

2.3.5 Characterization

Transmission electron microscopy (TEM) images were acquired using a Philips CM300 microscope operated at 300 kV. Scanning electron microscopy (SEM) images were obtained on a FEI Quanta 3D field emission microscope operated at 10.0 kV. X-ray photoelectron

spectroscopy (XPS) studies were conducted using a PHI5400/XPS instrument with an Al K_α source operated at 350 W and 10^{-9} Torr. XAS measurements were performed using the Sector 20-BM beamline of the Advanced Photon Source at Argonne National Laboratory (Argonne, IL). The beamline was equipped with a double-crystal Si(111) monochromator. A 12-element Ge fluorescence detector was used to collect spectra of the Fe and Co K-edge. The energy was calibrated according to the absorption edge of a pure Fe or Co foil, as appropriate. Data processing and fitting were performed using WinXAS[50] and Analyzer v0.1 software, with scattering paths generated by FEFF8.[51] S_0^2 values for Fe (0.80) and Co (0.74) were obtained by fitting Fe and Co foil, respectively.

2.3.6 Electrochemistry

All electrochemical tests were carried out on a CHI710 workstation in a three-electrode setup. A graphite rod was used as the counter electrode and a Ag/AgCl electrode in 1.0 M KCl was used as the reference electrode. This electrode was calibrated against a reversible hydrogen electrode (RHE), and all potentials in this study are reported in reference to this RHE. A rotating (gold) ring-(glassy carbon) disk electrode (RRDE, Pine Research Instruments) was used as the working electrode. To prepare catalyst inks, 0.8 mg of the samples obtained above and 2.0 µL Nafion were added to 200 µL of a water-ethanol mixture (1:1 v/v). After sonication for at least 30 min, 5.0 µL of the ink was dropcast onto the glassy carbon disk, corresponding to a catalyst loading of 81.30 µL/cm^2. Once the catalyst film was dried, 3.0 µL of 20% Nafion was added to cover the catalyst layer, and the electrodes were immersed into electrolyte solutions for testing.

2.4 Results and Discussion

In this study, duel metals and nitrogen-codoped porous carbon cages were prepared by using a three-step procedure (Figure 2.1): (i) SiO_2 nanoparticles were prepared and used as the rigid templates onto which a melamine-formaldehyde (MF) polymer layer is grown; (ii) the obtained SiO_2@MF nanoparticles were impregnated with select Fe and Co precursors, and underwent

pyrolysis at controlled temperatures for carbonization of the polymer layers; and (iii) finally the SiO_2 templates were removed by chemical etching with HF, affording dual metals and nitrogen-codoped porous carbon cages. In this procedure, melamine acted as the main carbon and nitrogen source, and formaldehyde used to link the melamine monomers to each other and to the silica surface.[52]

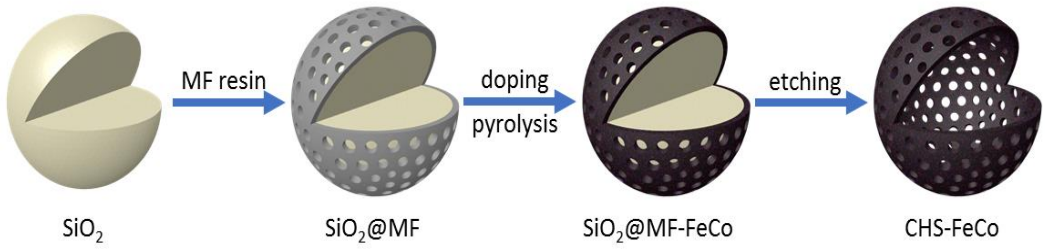

Figure 2.1 . Schematic illustration of the preparation of CHS-FeCo.

Figure 2.2 shows representative TEM images of (a) CHS and (b) CHS-FeCo(2). One can see that hollow carbon cages were successfully produced by pyrolysis of the SiO_2@MF precursors followed by HF etching, with the wall thickness mostly in the range of 1.0 to 2.5 nm (Figure 2.2b inset) and the interior diameter consistent with that of the SiO_2 sphere templates (140 ± 27 nm, Figure 2.3). In high-resolution TEM measurements (Figure 2b inset), the CHS-FeCo samples did not yield well-defined lattice fringes, suggesting the formation of only an amorphous carbon structure, as observed previously.[47] Remarkably, the fact that no particulate objects were observed also suggests that the metal species were most likely atomically dispersed within the carbon matrix. This is consistent with elemental mapping results based on energy-dispersive X-ray analysis, where both Fe and Co were scattered within the carbon matrix, without apparent agglomeration (Figure 2.2d-h). In addition, one can see that nitrogen is also rather evenly dispersed within the carbon skeleton, suggesting successful doping of nitrogen in the carbon.

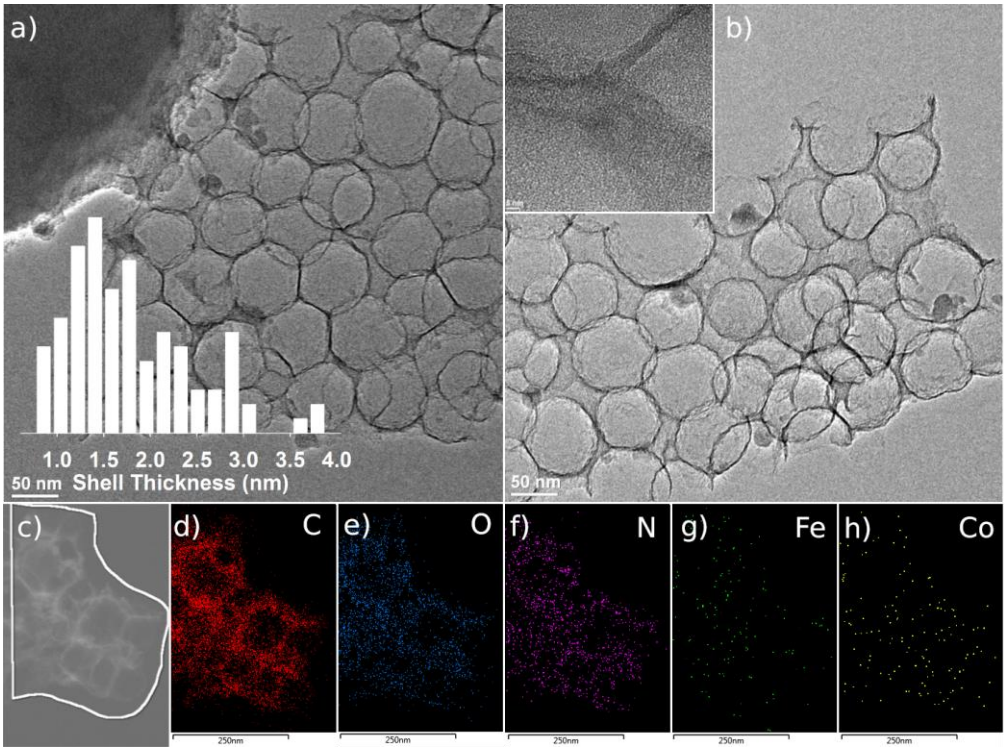

Figure 2.2 Electron microscopy studies. (a) Representative TEM image of CHS. Inset is a histogram of the shell thicknesses. (b) TEM image of CHS-FeCo(2). Inset is a high-resolution image of the sample. (c-h) Elemental maps of CHS-FeCo(2).

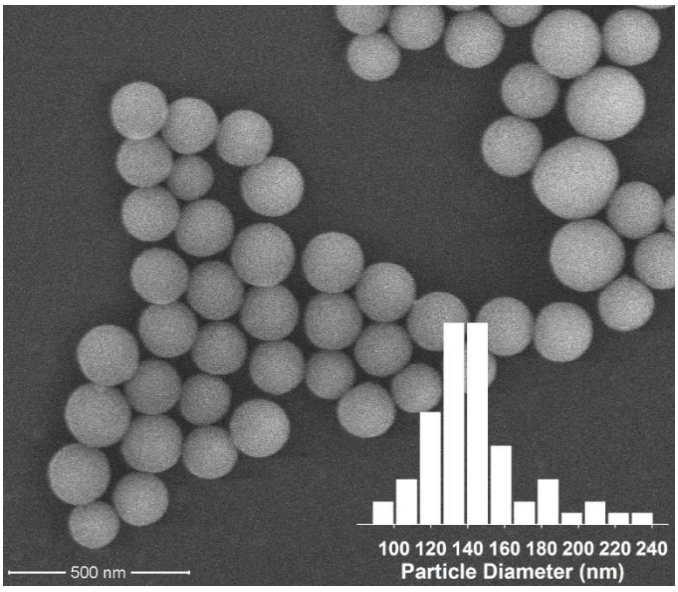

Figure 2.3SEM image of SiO2 spheres. Inset is a histogram of the particle diameters.

XPS measurements were then conducted to probe the elemental composition of the carbon cages and the valence states of the elements. The survey spectra (Figure 2.4) show that the cages are mainly composed of carbon, nitrogen, and oxygen, as well as iron and cobalt in the case of the CHS-FeCo samples, with the exception of those only doped with single Fe or Co, which are also consistent with the elemental maps shown above in Figure 2d-h. In addition, based on the integrated peak areas, the elemental contents in the samples were quantitatively assessed. From Table 2.1, one can see that for the metal-free CHS sample, carbon accounts for about 72.74 at% of the total content, nitrogen 9.21 at% and oxygen 14.23 at%. With the addition of a single metal precursor, these elemental fractions remained almost unchanged, with a trace amount of metal species, 0.16 at% for Fe in CHS-Fe and 0.06 at% for Co in CHS-Co. For the bimetallic CHS-FeCo(1,2,3) series, whereas the N content was almost invariant at ca. 6%, the total metal content increased from 0.32 at% for CHS-FeCo(1) to 0.38 at% for CHS-FeCo(2) and to 0.49 at% for CHS-FeCo(3), with the Fe content at 0.27 at% for

both CHS-FeCo(1) and CHS-FeCo(2) and 0.38 at% for CHS-FeCo(3), and the Co content at 0.05 at% for CHS-FeCo(1) and 0.11 at% for both CHS-FeCo(2) and CHS-FeCo(3).

Table 2.1 Elemental compositions of the CHS samples from XPS measurements

Sample	**C (at%)**	**O (at%)**	**N (at%)**	**Fe (at%)**	**Co (at%)**	**Total Metal (at%)**
CHS	72.74	14.23	9.21			
CHS-Fe	70.84	15.02	9.21	0.16		0.16
CHS-Co	73.54	11.93	9.80		0.06	0.06
CHS-FeCo(1)	71.03	17.63	5.88	0.27	0.05	0.32
CHS-FeCo(2)	64.01	20.60	6.28	0.27	0.11	0.38
CHS-FeCo(3)	79.64	11.22	6.87	0.38	0.11	0.49
CHS-$FeCo_{FeCl2}$	77.13	9.53	11.20	0.06	0.03	0.08
CHS-$FeCo_{FeCl3}$	77.91	11.19	8.44	0.03	0.03	0.06
CHS-$FeCo_{Fe(acac)3}$	70.93	13.35	11.58	0.08	0.02	0.10

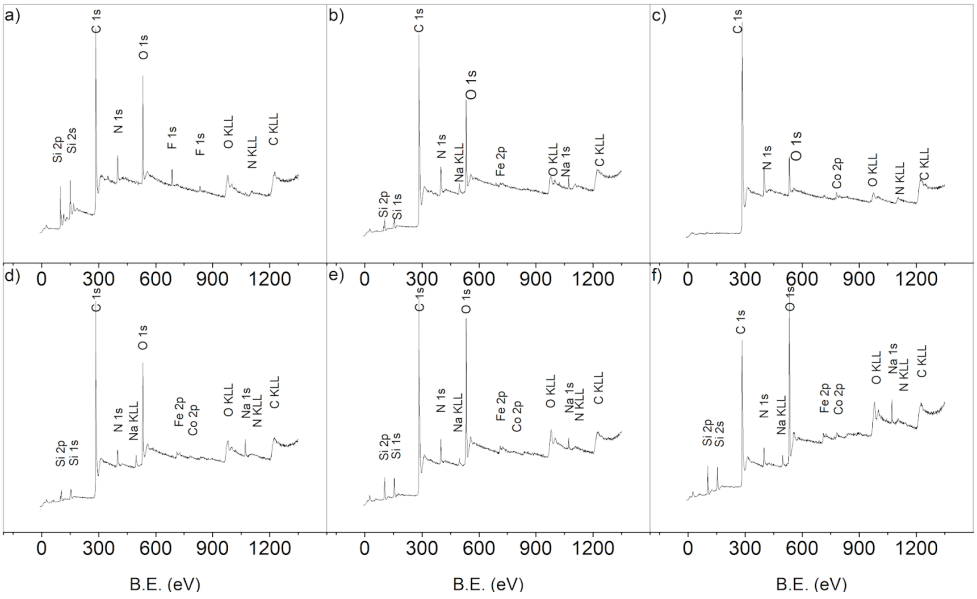

Figure 2.4 XPS survey spectra of (a) CHS, (b) CHS-Fe, (c) CHS-Co, (d) CHS-FeCo(1), (e) CHS-FeCo(2), and (f) CHS-FeCo(3).

High-resolution XPS scans for the C 1s, N 1s, Fe 2p, and Co 2p electrons are depicted in Figure 5. All C 1s scans (Figure 2.5a) exhibit a very similar shape and composition. Deconvolution yields a sharp peak at 284.5 eV, which can be assigned to graphitic (sp^2) carbon and provides evidence for successful carbonization of the melamine-formaldehyde resin, another one at 285.1 eV for sp^3-hybridized carbon (including N-bonded C), and two additional ones at 287.0 and 289.8 eV due to various forms of oxidized carbon that can be assigned to C=O, COOH, and π - π* transitions.[53,54] Figure 2.5b shows the N 1s scans of the CHS, CHS-Fe, CHS-Co and CHS-FeCo(1,2,3) samples. For the latter, six distinct peaks at 398.15, 398.97, 399.84, 400.84, and 401.75 eV can be resolved and assigned to pyridinic N, metal-N, pyrrolic, graphitic, and oxidized N, respectively (the small broad peak at 404.0 eV likely stems from chemisorbed NO_x species).[49,55,56] The integrated area of the N-metal peak decreases with

decreasing metal content in the samples and is completely absent in the metal-free CHS sample (Table 2.1, 2.2).

Table 2.2 Binding energies and contents of nitrogen dopants in CHS from XPS measurements.

Sample	N-Fe/Co		Pyridinic N		Pyrrolic N		Graphitic N		Oxidized N	
	B.E. (eV)	at%	B.E. (eV)	at%	B.E. (eV)	at%	B.E. (eV)	at%	B.E. (eV)	at%
CHS	-	-	398.29	3.19	399.80	1.95	400.89	2.15	401.79	1.91
CHS-Fe	398.96	1.51	398.14	3.11	399.92	1.71	400.86	1.52	401.67	1.35
CHS-Co	399.03	0.84	398.08	3.11	399.68	1.35	400.80	2.72	401.66	1.78
CHS-FeCo(1)	399.08	0.86	398.41	1.77	400.03	1.23	401.00	1.19	402.05	0.83
CHS-FeCo(2)	399.01	1.66	398.19	1.99	399.83	1.22	400.80	1.00	401.61	0.41
CHS-FeCo(3)	398.53	1.46	398.13	1.64	399.76	1.48	400.79	1.42	401.71	.87
CHS-$FeCo_{FeCl2}$	398.67	1.27	398.01	2.91	399.62	0.87	400.82	4.40	401.80	1.76
CHS-$FeCo_{FeCl3}$	398.96	1.19	398.07	2.22	399.89	1.62	400.81	1.51	401.67	1.90
CHS-$FeCo_{Fe(acac)3}$	398.82	2.14	398.12	3.10	399.60	2.27	400.88	2.60	401.69	1.47

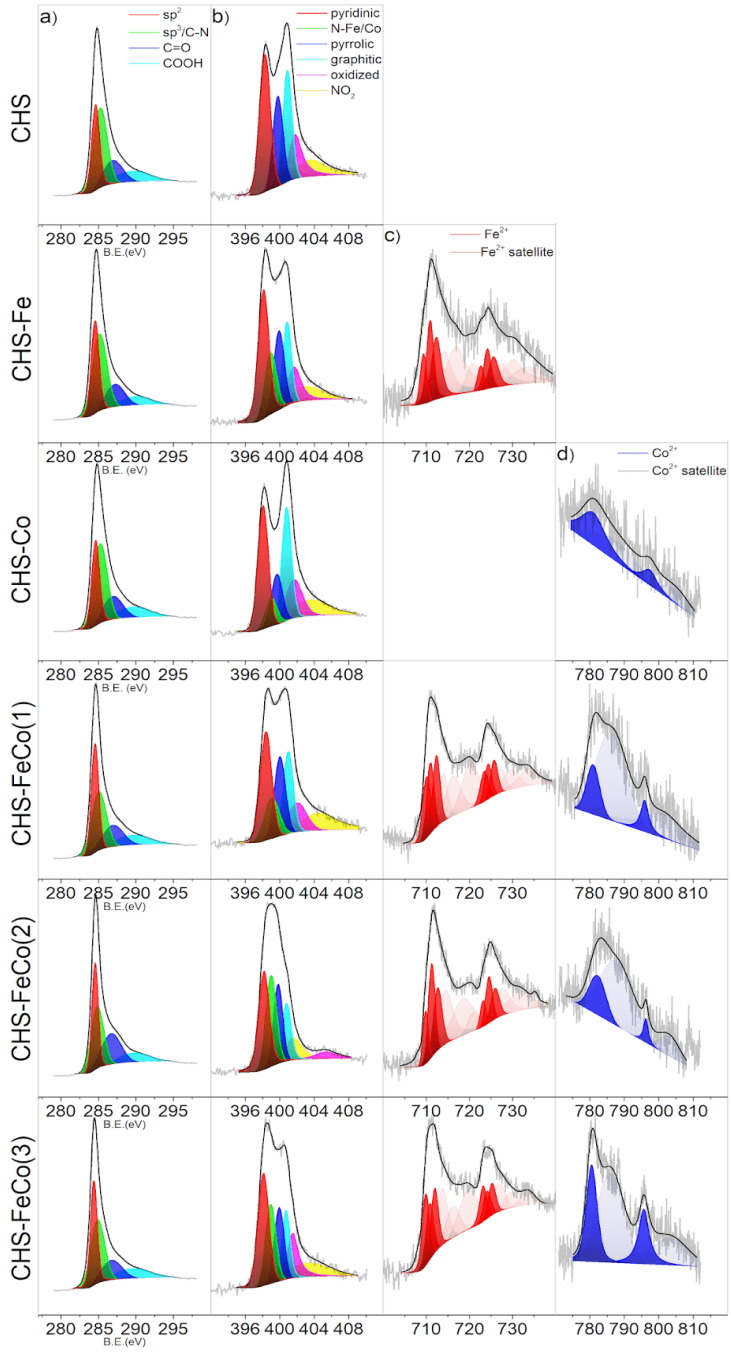

Figure 2.5 High-resolution XPS scans of the (a) C 1s, (b) N 1s, (c) Fe 2p, and (d) Co 2p electrons of CHS, CHS-Fe, CHS-Co, and CHS-FeCo(1,2,3) samples. Grey curves are experimental data, and colored peaks are deconvolution fits.

The respective high-resolution scans of the Fe 2p and Co 2p electrons are depicted in Figure 2.5c-d. Since both metals contain, in their high spin forms, unpaired electrons in non-spherically symmetric orbitals, the scans do not only exhibit spin-orbit coupling producing a larger $p_{3/2}$ and a smaller $p_{1/2}$ peak, but also spin multiplet splitting and various satellite features.[57] This is particularly prominent in the Fe 2p scans, whereas the intensity of the Co 2p peaks is too low to resolve individual spin multiplet peaks. The best fits for the Fe2p scans are based on Fe^{2+} multiplet patterns.[58] Similarly, the experimental data for Co is best fitted using a single set of Co^{2+} peaks and corresponding satellites,[59] noting that the peaks for Co^{2+} and Co^{3+} overlap to such an extent that it becomes impossible to resolve them reliably due to their low abundance.[57] Notably, the Fe $2p_{3/2}$ binding energy (Table 2.3) remains unchanged around 709.9 eV for all CHS-FeCo(1,2,3) samples, but somewhat higher than that (708.6 eV) for CHS-Fe. This binding energy is in the intermediate between those reported for Fe^{2+} and Fe^{3+},[57,58] indicating that the Fe species in the CHS-FeCo samples were likely Fe^{2+} in an electron-withdrawing environment, as compared to CHS-Fe, given that the precursor used was of the +2 oxidation state in all samples. Notably, the Co $2p_{3/2}$ binding energy can be estimated to be 779.8 eV for the samples; yet the low abundance of Co in combination with the overlap between the features of the different oxidation states makes it impossible to determine them precisely.[60] Lastly, high-resolution O 1s scans (Figure 2.6) suggest that no metal oxides are formed in the samples, as indicated by the absence of a corresponding peak between 529 and 530 eV (that is, the metal centers are embedded within the carbon matrix most likely forming M-N bonds).[61]

Table 2.3 Metal binding energies of the first peaks and atomic percentages from XPS measurements.

Sample	**Fe $2p_{3/2}$ B.E. (eV)**	**Fe at%**	**Co B.E. (eV)**	**Co at%**
CHS-Fe	708.56	0.16		
CHS-Co			779.53	0.06
CHS-FeCo(1)	709.88	0.27	779.78	0.05
CHS-FeCo(2)	709.90	0.24	779.82	0.10
CHS-FeCo(3)	709.90	0.38	779.92	0.11
CHS-$FeCo_{FeCl2}$	708.69	0.06	778.76	0.03
CHS-$FeCo_{FeCl3}$	709.35	0.03	780.11	0.03
CHS-$FeCo_{Fe(acac)3}$	709.05	0.08	778.81	0.02

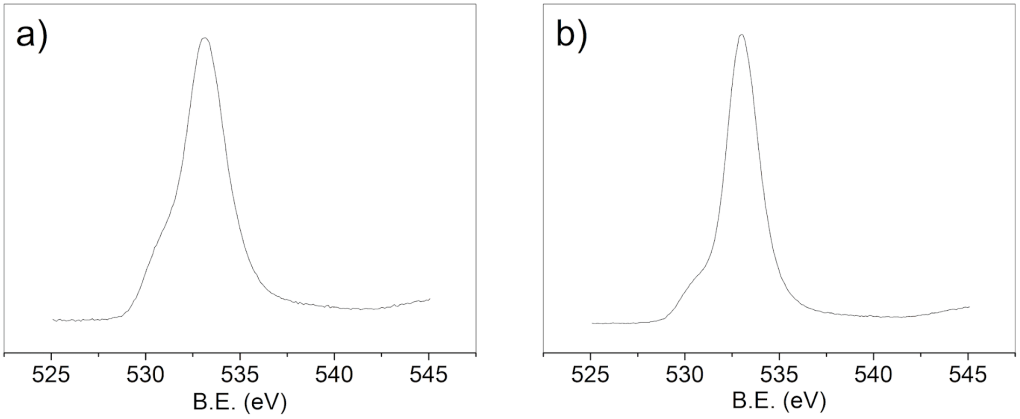

Figure 2.6 High-resolution O 1s XPS spectra of (a) CHS-FeCo(1) and (b) CHS-FeCo(2) samples.

X-ray absorption near-edge structure (XANES) and extended X-ray absorption fine structure (EXAFS) analysis was then conducted to probe the atomic configurations and coordination

environments of the metal centers. The Fe XANES curves in Figure 2.7a shows a fingerprint peak in the pre-edge region for the Fe foil at 7113 eV, which diminished markedly for the CHS-Fe and CHS-FeCo samples, implying that the Fe centers are non-metallic in the latter.[62] Additionally, one can see that both CHS-FeCo(2) and CHS-Fe exhibited a markedly higher absorption edge energy than the Fe foil, again, indicating a higher oxidation state of the Fe centers in CHS-Fe and CHS-FeCo than Fe(0). Furthermore, the fact that the absorption edge energy was slightly higher for CHS-FeCo(2) than for CHS-Fe is in good agreement with results from XPS measurements (Figure 2.5) where the Fe centers in the former were found to be situated in an electron-withdrawing environment, as compared to that in the latter. The same observation can be made for the Co XANEs profiles (Figure 2.7b), where the oxidation state of Co in CHS-FeCo is apparently higher than Co(0) in the Co foil.

Figure 2.7c shows the corresponding Fe FT-EXAFS spectra. The Fe foil can be seen to display two major peaks at 2.28 and 4.36 Å, due to the first and second shells of Fe-Fe.[63] These spectral features were totally absent in CHS-Fe and CHS-FeCo, which show a major peak at 1.58 Å. Because of the absence of metal oxides in the latter samples, this peak is most likely due to the first coordination shell of Fe–N,[62] and the average coordination number (CN) was estimated to be 3.8 for CHS-FeCo(2), significantly higher than that (3.2) for CHS-Fe (Table S4). This suggests that CHS-FeCo(2) contained a significant number of FeN_4 moieties, which are known to be very active for ORR, while other samples contained mostly unsaturated FeN_3 sites that are less active.[35] By contrast, CHS-Fe was best fitted with a single Fe–N shell, suggesting that the metals exist as single sites in the form of FeN_x, whereas the best fit for CHS-FeCo(2) consisted primarily of two shells, Fe–N and Fe–C/M. The peak corresponding to this second shell which may be due to the interaction between Co and Fe in this sample is located at 2.55Å. It is noteworthy to say that even though this peak is present in both samples, but at a much greater intensity in CHS-FeCo(2). Therefore, It is impossible to distinguish directly between Fe–C and Fe–Co, but since the corresponding peak also exists at low intensity in CHS-Fe, it is likely that this low intensity fraction originates from Fe–C, which is the only

possibility in CHS-Fe, while the remainder of the larger peak at 2.55Å in CHS-FeCo(2) most likely comes from Fe–Co.[64] In summary, EXAFS results suggest that the combination of Fe and Co results in a direct interaction between the two metal centers, with excess Fe present in the sample forming FeN_x.

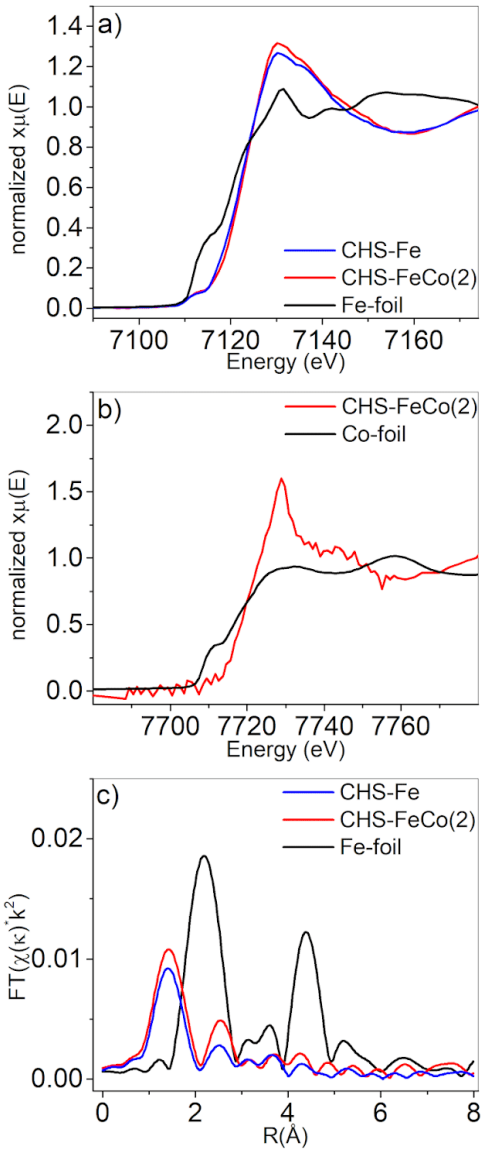

Figure 2.7 X-ray absorption spectroscopic studies. (a) Iron normalized X-ray absorption near edge structure data for CHS-Fe, CHS-FeCo(2), and Fe-foil. (b) Cobalt normalized X-ray absorption near edge structure data for CHS-FeCo(2) and Co-foil. (c) Fourier transform extended X-ray adsorption fine structure data for CHS-Fe, CHS-FeCo(2) and Fe foil.

Table 2.4 Structural parameters extracted from EXAFS fitting (S02 = 0.80)

Sample	Shell	C.N.	R (Å)	σ^2 (10^{-3} Å^2)	ΔE_0 (eV)
Fe foil[ref]	Fe-Fe	8 (fixed)	2.48(1)	1.4(2)	2.4(1)
	Fe-Fe	6 (fixed)	2.87(2)	7.8(2)	
CHS-Fe	Fe–N	3.2(4)	1.96(1)	6.3(3)	-5.2(1)
CHS-FeCo(2)	Fe–N	3.8(4)	1.98(1)	7.5(1)	-2.0(1)
	Fe–Co	1.3(2)	2.98(2)		

S_0^2 is the amplitude reduction factor (obtained by the fitting of Fe foil); CN is the coordination number; R is bond distance; σ^2 is Debye-Waller factor (a measure of thermal and static disorder in absorber-scatterer distances); ΔE_0 is edge-energy shift (the difference between the zero-kinetic energy value of the sample and that of the theoretical model).

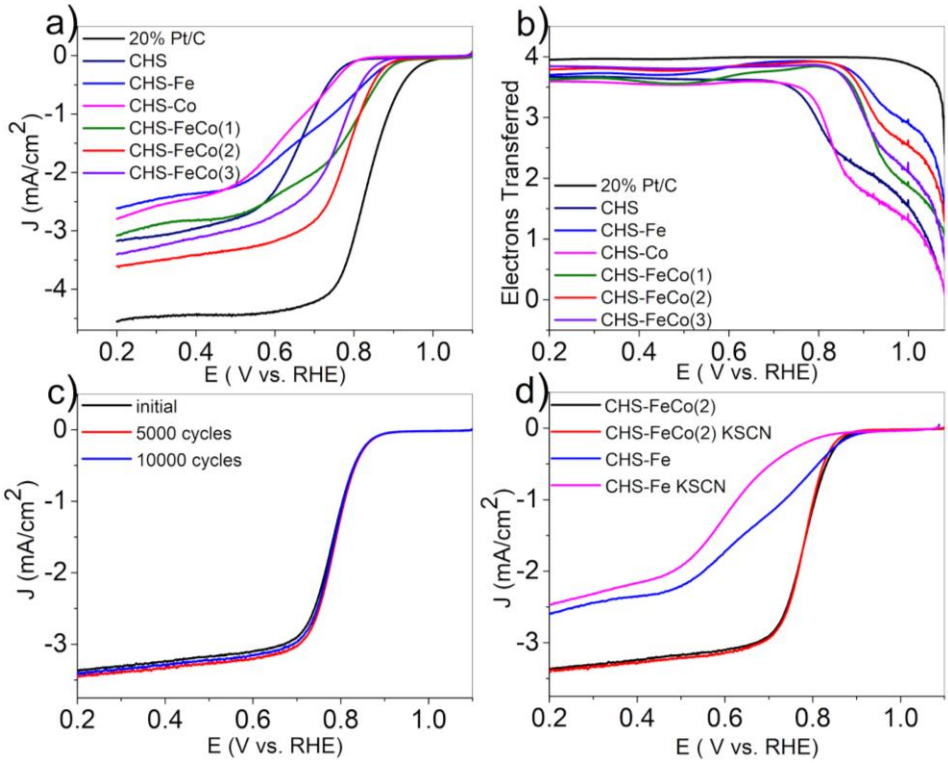

Figure 2.8 Polarization curves of various CHS samples at 1600 rpm and a potential scan rate of 10 mV/s in an oxygen-saturated 0.1 M KOH solution. (a) Comparison of CHS, CHS-Fe, CHS-Co, and CHS-FeCo(1,2,3). (b) Number of electron transfer for the various samples in (a). (c) Stability test of CHS-FeCo(2) for up to 10,000 potential cycles. (d) ORR polarization curves of CHS-FeCo(2) and CHS-Fe before and after the addition of KSCN to the electrolyte.

The electrocatalytic performance of the samples was then evaluated in RRDE measurements. From the polarization curves in Figure 2.8a, it is evident that the CHS-Co sample exhibited a very poor activity (E_{onset} = +0.81 V and $E_{½}$ = +0.65 V), similar to metal-free CHS (E_{onset} = +0.80 V and $E_{½}$ = +0.67 V). The performance was substantially improved with the CHS-Fe sample (E_{onset} = +0.92 V), as Fe-N moiety has been known to be active towards ORR.[65,66] An even better performance was observed with the CHS-FeCo samples (Table S5), which varied in the order of CHS-FeCo(3) (E_{onset} = +0.90 V and $E_{½}$ = +0.78 V) < CHS-FeCo(1) (E_{onset} = +0.89 V and $E_{½}$ = +0.74 V) < CHS-FeCo(2) (E_{onset} = +0.93 V and $E_{½}$ = +0.79 V).

Consistent behaviors can be seen in the respective electron transfer numbers in Figure 2.8b. For instance, at +0.50 V, n = 3.61 for CHS-FeCo(1), 3.80 for CHS-FeCo(2) and CHS-FeCo(3). Such a promising performance is highly comparable or even superior to leading single and dual doped Fe/Co catalyst reported in recent literature with relevant carbon-based catalysts (Table S6). These results suggest that CHS-FeCo(2) stood out as the best catalyst among the series (Figure 2.9, although the performance remains subpar as compared to that of Pt/C). This is most likely due to the synergistic effects of the two metal dopants, as evidenced in the above XPS and XAS measurements (Figure 2.5 and 2.7).

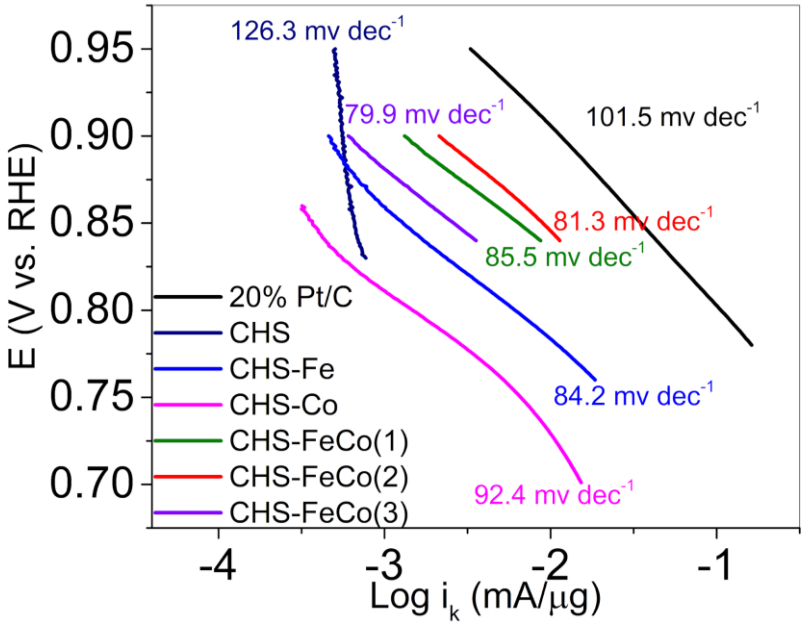

Figure 2.9 Tafel plot curves of the series of CHS samples calculated from polarization curves in Figure 2.8a.

Interestingly, the ORR performance also varied with both the counterion and oxidation state of the metal salt precursors. From Figure 2.10, one can see that CHS-FeCo prepared with $FeSO_4$ as the precursor exhibited a markedly better ORR activity than those with $FeCl_2$,

$FeCl_3$ and $Fe(acac)_3$. XPS analysis shows that the metal content of the samples was about eight times higher for the former (Figure 2.11), possibly due to the different thermal volatilities of the iron compounds.[67,68] However, the difference in metal content between the latter three was too small to account for their apparent difference of the catalytic performance. This suggests that the metal precursor used influences the chemical nature of the active sites, thereby enabling distinct catalytic pathways. Indications of such a chemical change have come from XPS and EXAFS analysis suggesting that the direct interaction between the Fe and Co dopants in CHS-FeCo is absent in other samples. Further research is strongly desired to unravel the

Table 2.5 Comparison of the ORR performance between CHS-FeCo(2) and relevant non-noble metal/carbon electrocatalysts in the literature in 0.1 M KOH

Sample	**Onset (V vs. RHE)**	**Half-Wave Potential (V vs. RHE)**	**Tafel slope (mv dec^{-1})**	**Reference**
CHS-FeCo(2)	+0.93	+0.79	81.3	This work
FeCo-NCNFs-800	+0.90	+0.81	60	ACS Sustainable Chem. Eng. 2019, 7,5462−5475
Fe/Co–CNTs-80	+0.928	+0.78	75	Chemistry Select 2018,3, 207–213
N-CNTs-650	+0.94	+0.85	NA	J. Am. Chem. Soc.2017, 139, 8212-8221

FeCo-NC	+0.86	+0.74	65	small. 2016,12,No. 31, 4193–4199
Fe/Co-NpGr	+0.93	+0.79	NA	Adv. Funct.Mater.2016, 26, 2150–2162
Fe-N-CFS	+0.93	+0.81	NA	Angew .Chem. Int. Ed.2015, 54, 8179-8183
Fe-N/C	+0.92	+0.81	NA	J. Am. Chem. Soc.2014, 136, 11027-11033
Co_3O_4/N-rm/GO	+0.84	+0.74	NA	Nat. Mater.2011, 10, 780-786

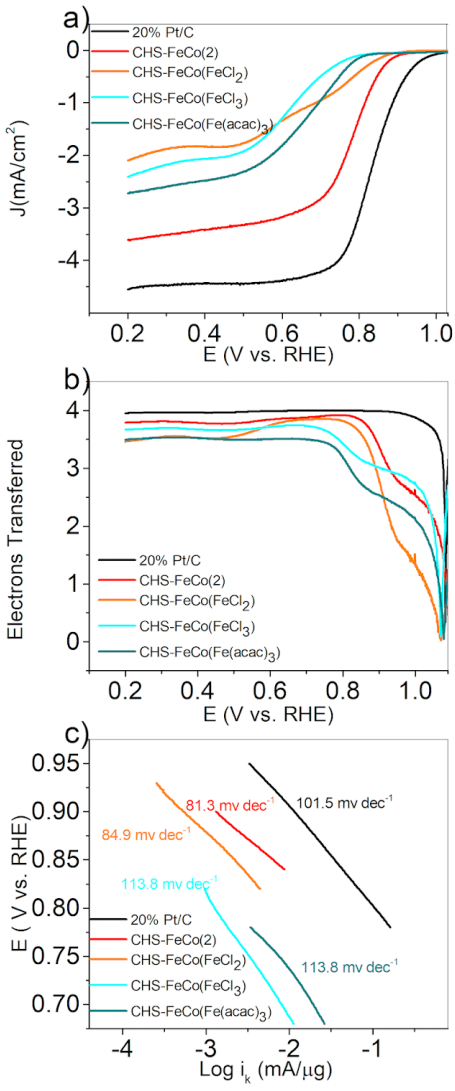

Figure 2.10 Polarization curves of various CHS samples at 1600 rpm and a potential scan rate of 10 mV/s in an oxygen-saturated 0.1 M KOH solution. (a) Comparison of CHS, CHS-Fe, CHS-FeCo(2), CHS-FeCo(FeCl2), CHS-FeCo(FeCl3), CHS-FeCo(Fe(acac)3). (b) Electron transfe transfer number (n) from panel (a). (d) Stabilty test of up to 10,000 potential cycles conducted with CHS-FeCo(2). (c) Tafel plot curves ofthe various samples

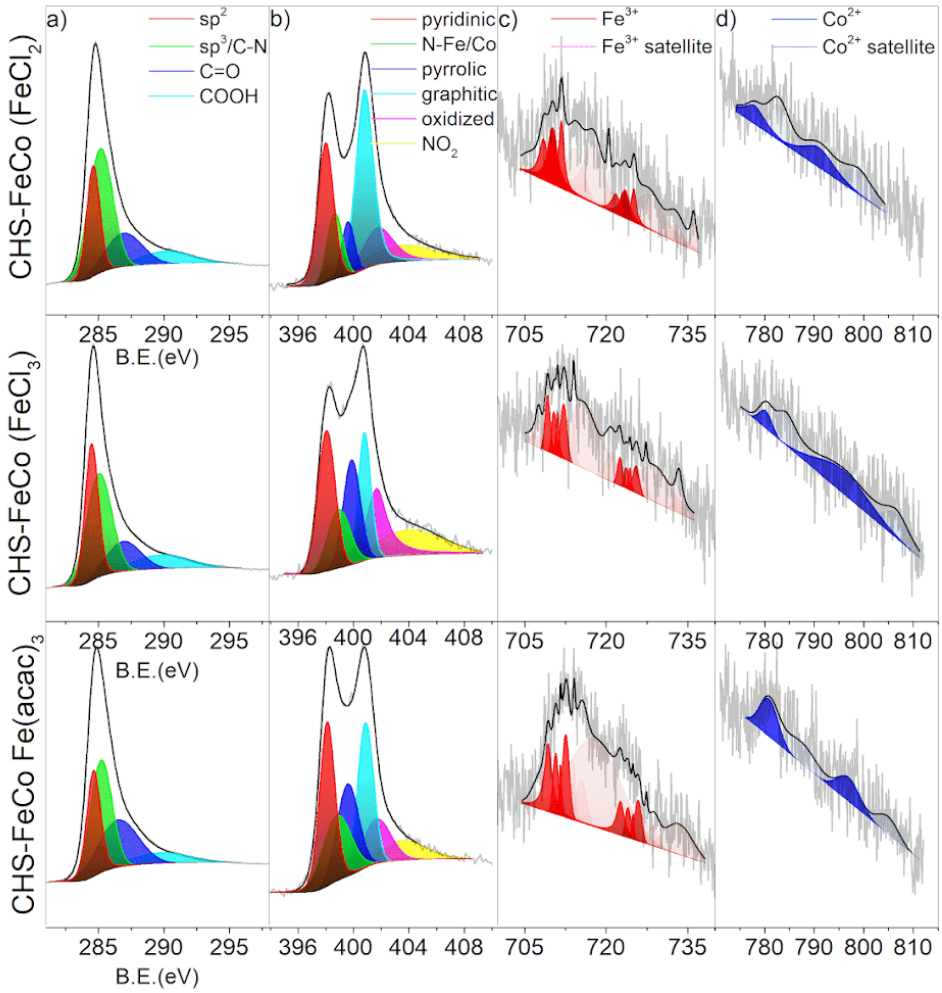

Figure 2.11 High-resolution XPS scans of the (a) C 1s, (b) N 1s, (c) Fe 2p, and (d) Co 2p electrons of CHS-FeCo (FeCl2), CHS-FeCo (FeCl3), CHS-FeCo (Fe(acac)3). Grey curves are experimental data, and colored areas are deconvolution fits.

The stability of the catalysts was then tested by repeated potential sweeping. As shown in Figure 2.8c, the polarization curves remained virtually unchanged for up to 10,000 cycles. Such remarkable stability confirms that the metal centers were indeed incorporated into the carbon spheres by forming strong M-N linkages. In addition to the stability test, the catalytic performance was examined when the electrolyte was poisoned with 10 mM KSCN (Figure

2.8d). The thiocyanate anion binds strongly and selectively to metals, both in nanoparticle and in atomically dispersed forms, blocking access to the metal active centers.[69] Therefore, if these metal centers are directly involved in the catalytic process, the addition of KSCN is expected to effectively diminish the catalytic activity, thereby providing insight into the nature of the active sites.[70,71] Interestingly, from Figure 5d one can see that CHS-FeCo(2) shows virtually no activity loss upon the addition of KSCN, whereas the activity of CHS-Fe deteriorated significantly, with the half-wave potential shifted negatively by ca. 100 mV. The latter observation has been observed rather extensively in prior studies.[72] However, the resistance of CHS-FeCo(2) against thiocyanide poisoning has never been seen with any dual metal-based catalysts for ORR.

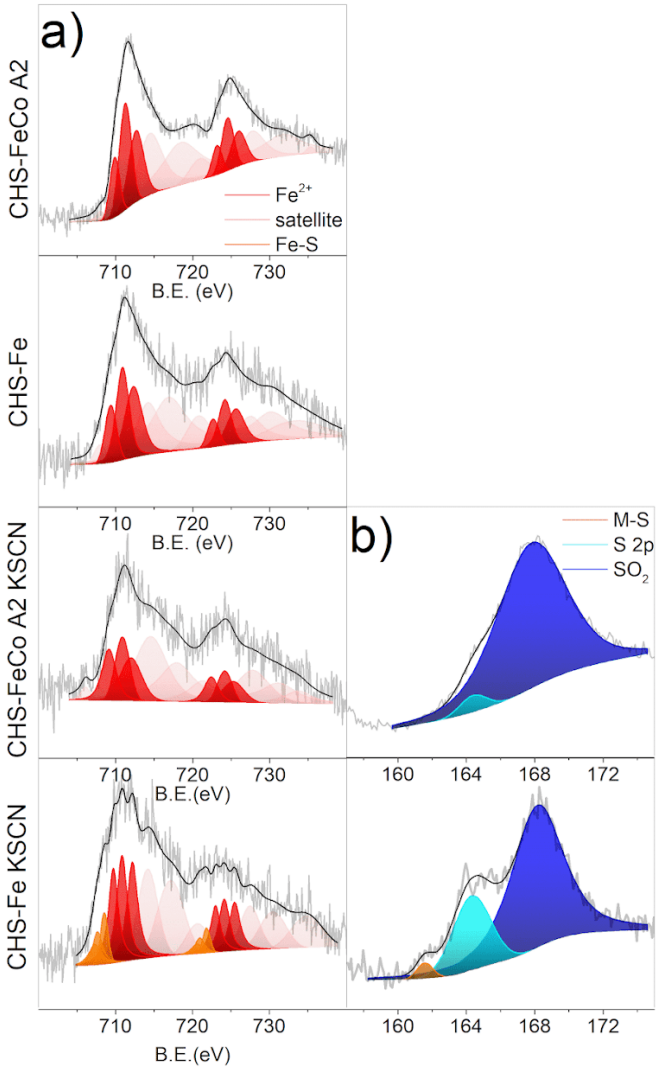

Figure 2.12 High-resolution XPS scans of the (a) Fe 2p, (b) S 2p, electrons of CHS-FeCo(2) and CHS-Fe before and after the addition of KSCN. Grey curves are experimental data, and shaded peaks are deconvolution fits.

The structures of the CHS-FeCo(2) and CHS-Fe samples were then analyzed by XPS measurements before and after the KSCN poisoning tests (Figure 2.12). For CHS-Fe, the spectral results exhibit clear signs of KSCN poisoning, as demonstrated by the notable metal-sulfur (M-S) signature with an S 2p peak at the binding energy of 161.2 eV.[73]

Meanwhile, a new set of peaks emerged in the Fe 2p spectrum at 707.3, 707.7 and 708.5 eV, which can all be attributed to Fe(II) in Fe(II)-S bond.[74] This poisoning led to a marked diminishment of the ORR activity of CHS-Fe. By contrast, no such S and Fe species can be found for CHS-FeCo(2) after KSCN treatment. One can see that the Fe(II) $2p_{1/2}$ binding energy exhibited only a slight variation from 709.90 to 709.19 eV, and S 2p electrons showed only a peak at 167.82 eV for SO_2 and another one at 164.4 eV for elemental S.[74] This suggests that SCN^- was mostly likely oxidized by CHS-FeCo(2) to SO_2, and the lack of KSCN poisoning of the CHS-FeCo(2) catalyst is in good agreement with the almost unchanged electrocatalytic activity (Figure 2.5d). Further studies are needed to unravel the mechanistic details.

2.5 Conclusion

In this study, dual metals (Fe and Co) and nitrogen-codoped carbon cages were prepared by controlled pyrolysis of a melamine-formaldehyde polymer shell supported on SiO_2 nanoparticle templates. TEM and X-ray absorption spectroscopic measurements suggested atomic dispersion of the metal centers within the carbon matrix and the synergistic interactions between the dual metal centers led to marked enhancement of the electrocatalytic activity towards ORR in alkaline media, as compared to the metal-free or monometal counterparts. Remarkably, the dual-metal sample exhibited apparent resistance against thiocyanide poisoning. Results from this study suggest that dual metal doping and the ensuing metal-metal interactions may be exploited as a unique strategy for further enhancement of ORR electrocatalysis by carbon-based nanocomposites for.

Acknowledgments

This work was supported in part by the National Science Foundation (CHE-1710408 and CHE-1900235). TEM and XPS work was carried out at the National Center for Electron Microscopy and Molecular Foundry, Lawrence Berkeley National Laboratory, which is supported by the US Department of Energy, as part of a user project.

2.6 References

(1) Zhou, X. J.; Qiao, J. L.; Yang, L.; Zhang, J. J. A Review of Graphene-Based Nanostructural Materials for Both Catalyst Supports and Metal-Free Catalysts in PEM Fuel Cell Oxygen Reduction Reactions. *Adv Energy Mater* **2014**, *4*.

(2) Yang, Z.; Nie, H.; Chen, X.; Huang, S. Recent progress in doped carbon nanomaterials as effective cathode catalysts for fuel cell oxygen reduction reaction. *J Power Sources* **2013**, *236*, 238-249.

(3) Fernández, J. L.; Raghuveer, V.; Manthiram, A.; Bard, A. J. Pd− Ti and Pd− Co− Au electrocatalysts as a replacement for platinum for oxygen reduction in proton exchange membrane fuel cells. *Journal of the American Chemical Society* **2005**, *127*, 13100-13101.

(4) Yamamoto, K.; Imaoka, T.; Chun, W.-J.; Enoki, O.; Katoh, H.; Takenaga, M.; Sonoi, A. Size-specific catalytic activity of platinum clusters enhances oxygen reduction reactions. *Nat Chem* **2009**, *1*, 397.

(5) Wang, Y.-J.; Zhao, N.; Fang, B.; Li, H.; Bi, X. T.; Wang, H. Carbon-supported Pt-based alloy electrocatalysts for the oxygen reduction reaction in polymer electrolyte membrane fuel cells: particle size, shape, and composition manipulation and their impact to activity. *Chemical reviews* **2015**, *115*, 3433-3467.

(6) Gong, K.; Du, F.; Xia, Z.; Durstock, M.; Dai, L. Nitrogen-doped carbon nanotube arrays with high electrocatalytic activity for oxygen reduction. *Science* **2009**, *323*, 760-764.

(7) Jian, L.; Zhang, Q. S.; Sandy, B. H.; (Max), L. G. Q. Monodisperse Yolk–Shell Nanoparticles with a Hierarchical Porous Structure for Delivery Vehicles and Nanoreactors. *Angewandte Chemie* **2010**, *122*, 5101-5105.

(8) Ai, K.; Liu, Y.; Ruan, C.; Lu, L.; Lu, G. Sp2 C-dominant N-doped carbon sub-micrometer spheres with a tunable size: a versatile platform for highly efficient oxygen-reduction catalysts. *Advanced Materials* **2013**, *25*, 998-1003.

(9) Li, Y.; Zhao, Y.; Cheng, H.; Hu, Y.; Shi, G.; Dai, L.; Qu, L. Nitrogen-doped graphene quantum dots with oxygen-rich functional groups. *Journal of the American Chemical Society* **2011**, *134*, 15-18.

(10) Masa, J.; Xia, W.; Muhler, M.; Schuhmann, W. On the Role of Metals in Nitrogen-Doped Carbon Electrocatalysts for Oxygen Reduction. *Angewandte Chemie International Edition* **2015**, *54*, 10102-10120.

(11) Choi, C. H.; Park, S. H.; Woo, S. I. Binary and ternary doping of nitrogen, boron, and phosphorus into carbon for enhancing electrochemical oxygen reduction activity. *Acs Nano* **2012**, *6*, 7084-7091.

(12) Fang, X.; Zhao, X.; Fang, W.; Chen, C.; Zheng, N. Self-templating synthesis of hollow mesoporous silica and their applications in catalysis and drug delivery. *Nanoscale* **2013**, *5*, 2205-2218.

(13) Shi, Z.; Liu, H.; Lee, K.; Dy, E.; Chlistunoff, J.; Blair, M.; Zelenay, P.; Zhang, J.; Liu, Z.-S. Theoretical study of possible active site structures in cobalt-polypyrrole catalysts for oxygen reduction reaction. *The Journal of Physical Chemistry C* **2011**, *115*, 16672-16680.

(14) Jaouen, F.; Lefèvre, M.; Dodelet, J.-P.; Cai, M. Heat-treated Fe/N/C catalysts for O2 electroreduction: are active sites hosted in micropores? *The Journal of Physical Chemistry B* **2006**, *110*, 5553-5558.

(15) Strickland, K.; Miner, E.; Jia, Q.; Tylus, U.; Ramaswamy, N.; Liang, W.; Sougrati, M.-T.; Jaouen, F.; Mukerjee, S. Highly active oxygen reduction non-platinum group metal electrocatalyst without direct metal–nitrogen coordination. *Nature communications* **2015**, *6*, 7343.

(16) Chung, H. T.; Won, J. H.; Zelenay, P. Active and stable carbon nanotube/nanoparticle composite electrocatalyst for oxygen reduction. *Nature communications* **2013**, *4*, 1922.

(17) Singh, K. P.; Bae, E. J.; Yu, J.-S. Fe–P: a new class of electroactive catalyst for oxygen reduction reaction. *Journal of the American Chemical Society* **2015**, *137*, 3165-3168.

(18) Zagal, J. H.; Koper, M. T. Reactivity descriptors for the activity of molecular MN4 catalysts for the oxygen reduction reaction. *Angewandte Chemie International Edition* **2016**, *55*, 14510-14521.

(19) Schulenburg, H.; Stankov, S.; Schünemann, V.; Radnik, J.; Dorbandt, I.; Fiechter, S.; Bogdanoff, P.; Tributsch, H. Catalysts for the oxygen reduction from heat-treated iron (III) tetramethoxyphenylporphyrin chloride: structure and stability of active sites. *The Journal of Physical Chemistry B* **2003**, *107*, 9034-9041.

(20) Zhou, Q.; Li, C. M.; Li, J.; Lu, J. Electrocatalysis of template-electrosynthesized cobalt− porphyrin/polyaniline nanocomposite for oxygen reduction. *The Journal of Physical Chemistry C* **2008**, *112*, 18578-18583.

(21) Maldonado, S.; Stevenson, K. J. Direct preparation of carbon nanofiber electrodes via pyrolysis of iron (II) phthalocyanine: electrocatalytic aspects for oxygen reduction. *The Journal of Physical Chemistry B* **2004**, *108*, 11375-11383.

(22) Wu, G.; More, K. L.; Johnston, C. M.; Zelenay, P. High-performance electrocatalysts for oxygen reduction derived from polyaniline, iron, and cobalt. *Science* **2011**, *332*, 443-447.

(23) Proietti, E.; Jaouen, F.; Lefèvre, M.; Larouche, N.; Tian, J.; Herranz, J.; Dodelet, J.-P. Iron-based cathode catalyst with enhanced power density in polymer electrolyte membrane fuel cells. *Nature communications* **2011**, *2*, 416.

(24) Chlistunoff, J. RRDE and voltammetric study of ORR on pyrolyzed Fe/polyaniline catalyst. On the origins of variable Tafel slopes. *The Journal of Physical Chemistry C* **2011**, *115*, 6496-6507.

(25) Wu, G.; Artyushkova, K.; Ferrandon, M.; Kropf, A. J.; Myers, D.; Zelenay, P. Performance durability of polyaniline-derived non-precious cathode catalysts. *Ecs Transactions* **2009**, *25*, 1299-1311.

(26) Mehmood, A.; Pampel, J.; Ali, G.; Ha, H. Y.; Ruiz-Zepeda, F.; Fellinger, T. P. Facile Metal Coordination of Active Site Imprinted Nitrogen Doped Carbons for the Conservative Preparation of Non-Noble Metal Oxygen Reduction Electrocatalysts. *Adv Energy Mater* **2018**, *8*, 1701771.

(27) Leonard, N. D.; Wagner, S.; Luo, F.; Steinberg, J.; Ju, W.; Weidler, N.; Wang, H.; Kramm, U. I.; Strasser, P. Deconvolution of Utilization, Site Density, and Turnover Frequency of Fe–Nitrogen–Carbon Oxygen Reduction Reaction Catalysts Prepared with Secondary N-Precursors. *Acs Catal* **2018**, *8*, 1640-1647.

(28) Peng, Y.; Lu, B.; Chen, S. Carbon-Supported Single Atom Catalysts for Electrochemical Energy Conversion and Storage. *Advanced Materials* **2018**, *30*, 1801995.

(29) Qian, Y.; Du, P.; Wu, P.; Cai, C.; Gervasio, D. F. Chemical nature of catalytic active sites for the oxygen reduction reaction on nitrogen-doped carbon-supported non-noble metal catalysts. *The Journal of Physical Chemistry C* **2016**, *120*, 9884-9896.

(30) Fu, G.-T.; Liu, C.; Zhang, Q.; Chen, Y.; Tang, Y.-W. Polyhedral Palladium–Silver Alloy Nanocrystals as Highly Active and Stable Electrocatalysts for the Formic Acid Oxidation Reaction. *Sci Rep-Uk* **2015**, *5*, 13703.

(31) Bu, L.; Zhang, N.; Guo, S.; Zhang, X.; Li, J.; Yao, J.; Wu, T.; Lu, G.; Ma, J.-Y.; Su, D. Biaxially strained PtPb/Pt core/shell nanoplate boosts oxygen reduction catalysis. *Science* **2016**, *354*, 1410-1414.

(32) Zhu, Z.; Zhai, Y.; Dong, S. Facial synthesis of PtM (M= Fe, Co, Cu, Ni) bimetallic alloy nanosponges and their enhanced catalysis for oxygen reduction reaction. *Acs Appl Mater Inter* **2014**, *6*, 16721-16726.

(33) Xue, H.; Tang, J.; Gong, H.; Guo, H.; Fan, X.; Wang, T.; He, J.; Yamauchi, Y. Fabrication of PdCo bimetallic nanoparticles anchored on three-dimensional ordered N-doped

porous carbon as an efficient catalyst for oxygen reduction reaction. *Acs Appl Mater Inter* **2016**, *8*, 20766-20771.

(34) Lu, B.; Guo, L.; Wu, F.; Peng, Y.; Lu, J. E.; Smart, T. J.; Wang, N.; Finfrock, Y. Z.; Morris, D.; Zhang, P. Ruthenium atomically dispersed in carbon outperforms platinum toward hydrogen evolution in alkaline media. *Nature communications* **2019**, *10*, 631.

(35) Zitolo, A.; Goellner, V.; Armel, V.; Sougrati, M.-T.; Mineva, T.; Stievano, L.; Fonda, E.; Jaouen, F. Identification of catalytic sites for oxygen reduction in iron-and nitrogen-doped graphene materials. *Nat Mater* **2015**, *14*, 937.

(36) Yi, J.-D.; Xu, R.; Wu, Q.; Zhang, T.; Zang, K.-T.; Luo, J.; Liang, Y.-L.; Huang, Y.-B.; Cao, R. Atomically dispersed iron–nitrogen active sites within porphyrinic triazine-based frameworks for oxygen reduction reaction in both alkaline and acidic media. *ACS Energy Letters* **2018**, *3*, 883-889.

(37) Lin, L.; Yang, Z. K.; Jiang, Y.-F.; Xu, A.-W. Nonprecious bimetallic (Fe, Mo)–N/C catalyst for efficient oxygen reduction reaction. *Acs Catal* **2016**, *6*, 4449-4454.

(38) Choi, J.-Y.; Hsu, R. S.; Chen, Z. Highly active porous carbon-supported nonprecious metal− N electrocatalyst for oxygen reduction reaction in PEM fuel cells. *The Journal of Physical Chemistry C* **2010**, *114*, 8048-8053.

(39) Lin, Q.; Bu, X.; Kong, A.; Mao, C.; Bu, F.; Feng, P. Heterometal-embedded organic conjugate frameworks from alternating monomeric iron and cobalt metalloporphyrins and their application in design of porous carbon catalysts. *Advanced materials* **2015**, *27*, 3431-3436.

(40) Cheon, J. Y.; Kim, T.; Choi, Y.; Jeong, H. Y.; Kim, M. G.; Sa, Y. J.; Kim, J.; Lee, Z.; Yang, T.-H.; Kwon, K. Ordered mesoporous porphyrinic carbons with very high electrocatalytic activity for the oxygen reduction reaction. *Sci Rep-Uk* **2013**, *3*, 2715.

(41) Liang, C.; Li, Z.; Dai, S. Mesoporous carbon materials: synthesis and modification. *Angewandte Chemie International Edition* **2008**, *47*, 3696-3717.

(42) Yang, W.; Fellinger, T.-P.; Antonietti, M. Efficient metal-free oxygen reduction in alkaline medium on high-surface-area mesoporous nitrogen-doped carbons made from ionic liquids and nucleobases. *Journal of the American Chemical Society* **2010**, *133*, 206-209.

(43) Niu, W.; Li, L.; Liu, X.; Wang, N.; Liu, J.; Zhou, W.; Tang, Z.; Chen, S. Mesoporous N-doped carbons prepared with thermally removable nanoparticle templates: an efficient electrocatalyst for oxygen reduction reaction. *Journal of the American Chemical Society* **2015**, *137*, 5555-5562.

(44) Niu, W.; Li, L.; Liu, J.; Wang, N.; Li, W.; Tang, Z.; Zhou, W.; Chen, S. Graphene-Supported Mesoporous Carbons Prepared with Thermally Removable Templates as Efficient Catalysts for Oxygen Electroreduction. *Small* **2016**, *12*, 1900-1908.

(45) Niu, W.; Li, L.; Wang, N.; Zeng, S.; Liu, J.; Zhao, D.; Chen, S. Volatilizable template-assisted scalable preparation of honeycomb-like porous carbons for efficient oxygen electroreduction. *Journal of Materials Chemistry A* **2016**, *4*, 10820-10827.

(46) Niu, W.; Li, L.; Chen, S. Recent progress in template-assisted synthesis of nitrogen-doped porous carbons for oxygen electroreduction. *Journal of Electrochemistry* **2017**, *23*, 110-122.

(47) Lu, B.; Smart, T. J.; Qin, D.; Lu, J. E.; Wang, N.; Chen, L.; Peng, Y.; Ping, Y.; Chen, S. Nitrogen and Iron-Codoped Carbon Hollow Nanotubules as High-Performance Catalysts toward Oxygen Reduction Reaction: A Combined Experimental and Theoretical Study. *Chemistry of Materials* **2017**, *29*, 5617-5628.

(48) Harada, T.; Ikeda, S.; Ng, Y. H.; Sakata, T.; Mori, H.; Torimoto, T.; Matsumura, M. Rhodium Nanoparticle Encapsulated in a Porous Carbon Shell as an Active Heterogeneous Catalyst for Aromatic Hydrogenation. *Advanced Functional Materials* **2008**, *18*, 2190-2196.

(49) Zhang, R.; He, S.; Lu, Y.; Chen, W. Fe, Co, N-functionalized carbon nanotubes in situ grown on 3D porous N-doped carbon foams as a noble metal-free catalyst for oxygen reduction. *Journal of Materials Chemistry A* **2015**, *3*, 3559-3567.

(50) Ressler, T. WinXAS: a program for X-ray absorption spectroscopy data analysis under MS-Windows. *Journal of synchrotron radiation* **1998**, *5*, 118-122.

(51) Ankudinov, A.; Ravel, B.; Rehr, J.; Conradson, S. Real-space multiple-scattering calculation and interpretation of x-ray-absorption near-edge structure. *Phys Rev B* **1998**, *58*, 7565.

(52) Mou, S.; Lu, Y.; Jiang, Y. A facile and cheap coating method to prepare SiO2/melamine-formaldehyde and SiO2/urea-formaldehyde composite microspheres. *Applied Surface Science* **2016**, *384*, 258-262.

(53) Yang, Z.; Xu, M.; Liu, Y.; He, F.; Gao, F.; Su, Y.; Wei, H.; Zhang, Y. Nitrogen-doped, carbon-rich, highly photoluminescent carbon dots from ammonium citrate. *Nanoscale* **2014**, *6*, 1890-1895.

(54) Kundu, S.; Wang, Y.; Xia, W.; Muhler, M. Thermal stability and reducibility of oxygen-containing functional groups on multiwalled carbon nanotube surfaces: a quantitative high-resolution XPS and TPD/TPR study. *The Journal of Physical Chemistry C* **2008**, *112*, 16869-16878.

(55) Sarapuu, A.; Samolberg, L.; Kreek, K.; Koel, M.; Matisen, L.; Tammeveski, K. Cobalt-and iron-containing nitrogen-doped carbon aerogels as non-precious metal catalysts for electrochemical reduction of oxygen. *Journal of Electroanalytical Chemistry* **2015**, *746*, 9-17.

(56) Zhong, H.; Zhang, H.; Liu, S.; Deng, C.; Wang, M. Nitrogen-Enriched Carbon from Melamine Resins with Superior Oxygen Reduction Reaction Activity. *ChemSusChem* **2013**, *6*, 807-812.

(57) Biesinger, M. C.; Payne, B. P.; Grosvenor, A. P.; Lau, L. W.; Gerson, A. R.; Smart, R. S. C. Resolving surface chemical states in XPS analysis of first row transition metals, oxides and hydroxides: Cr, Mn, Fe, Co and Ni. *Applied Surface Science* **2011**, *257*, 2717-2730.

(58) Grosvenor, A.; Kobe, B.; Biesinger, M.; McIntyre, N. Investigation of multiplet splitting of Fe 2p XPS spectra and bonding in iron compounds. *Surface and Interface Analysis:*

An International Journal devoted to the development and application of techniques for the analysis of surfaces, interfaces and thin films **2004**, *36*, 1564-1574.

(59) Chen, Y.; Zhao, S.; Liu, Z. Influence of the synergistic effect between Co–N–C and ceria on the catalytic performance for selective oxidation of ethylbenzene. *Physical Chemistry Chemical Physics* **2015**, *17*, 14012-14020.

(60) Powell, C. Elemental binding energies for X-ray photoelectron spectroscopy. *Applied Surface Science* **1995**, *89*, 141-149.

(61) Dupin, J.-C.; Gonbeau, D.; Vinatier, P.; Levasseur, A. Systematic XPS studies of metal oxides, hydroxides and peroxides. *Physical Chemistry Chemical Physics* **2000**, *2*, 1319-1324.

(62) Chen, Y.; Ji, S.; Wang, Y.; Dong, J.; Chen, W.; Li, Z.; Shen, R.; Zheng, L.; Zhuang, Z.; Wang, D. Isolated single iron atoms anchored on N-doped porous carbon as an efficient electrocatalyst for the oxygen reduction reaction. *Angewandte Chemie International Edition* **2017**, *56*, 6937-6941.

(63) Cao, L.; Liu, W.; Luo, Q.; Yin, R.; Wang, B.; Weissenrieder, J.; Soldemo, M.; Yan, H.; Lin, Y.; Sun, Z. Atomically dispersed iron hydroxide anchored on Pt for preferential oxidation of CO in H 2. *Nature* **2019**, *565*, 631.

(64) Chang, Q.; Zhang, C.; Liu, C.; Wei, Y.; Cheruvathur, A. V.; Dugulan, A. I.; Niemantsverdriet, J.; Liu, X.; He, Y.; Qing, M. Relationship between Iron Carbide Phases (ε-Fe2C, Fe7C3, and χ-Fe5C2) and Catalytic Performances of Fe/SiO2 Fischer–Tropsch Catalysts. *Acs Catal* **2018**, *8*, 3304-3316.

(65) Song, L. T.; Wu, Z. Y.; Zhou, F.; Liang, H. W.; Yu, Z. Y.; Yu, S. H. Sustainable Hydrothermal Carbonization Synthesis of Iron/Nitrogen-Doped Carbon Nanofiber Aerogels as Electrocatalysts for Oxygen Reduction. *Small* **2016**, *12*, 6398-6406.

(66) Wang, Y.; Kong, A.; Chen, X.; Lin, Q.; Feng, P. Efficient oxygen electroreduction: hierarchical porous Fe–N-doped hollow carbon nanoshells. *Acs Catal* **2015**, *5*, 3887-3893.

(67) Hollebone, B. R.; Wiles, D. R.: Preparation of volatile metal chlorides from their ores. Google Patents, 1968.

(68) Hoene, J. V.; Charles, R. G.; Hickam, W. M. Thermal decomposition of metal acetylacetonates: mass spectrometer studies. *The Journal of Physical Chemistry* **1958**, *62*, 1098-1101.

(69) Wang, Q.; Zhou, Z.-Y.; Lai, Y.-J.; You, Y.; Liu, J.-G.; Wu, X.-L.; Terefe, E.; Chen, C.; Song, L.; Rauf, M. Phenylenediamine-based FeN x/C catalyst with high activity for oxygen reduction in acid medium and its active-site probing. *Journal of the American chemical Society* **2014**, *136*, 10882-10885.

(70) Thorum, M. S.; Hankett, J. M.; Gewirth, A. A. Poisoning the oxygen reduction reaction on carbon-supported Fe and Cu electrocatalysts: evidence for metal-centered activity. *The Journal of Physical Chemistry Letters* **2011**, *2*, 295-298.

(71) Varnell, J. A.; Edmund, C.; Schulz, C. E.; Fister, T. T.; Haasch, R. T.; Timoshenko, J.; Frenkel, A. I.; Gewirth, A. A. Identification of carbon-encapsulated iron nanoparticles as active species in non-precious metal oxygen reduction catalysts. *Nature communications* **2016**, *7*, 12582.

(72) Huang, Z.; Pan, H.; Yang, W.; Zhou, H.; Gao, N.; Fu, C.; Li, S.; Li, H.; Kuang, Y. In situ self-template synthesis of Fe–N-doped double-shelled hollow carbon microspheres for oxygen reduction reaction. *Acs Nano* **2018**, *12*, 208-216.

(73) Niu, S.; Jiang, W. J.; Tang, T.; Yuan, L. P.; Luo, H.; Hu, J. S. Autogenous Growth of Hierarchical NiFe (OH) x/FeS Nanosheet-On-Microsheet Arrays for Synergistically Enhanced High-Output Water Oxidation. *Advanced Functional Materials* **2019**, *29*, 1902180.

(74) Han, W.; Gao, M. Investigations on iron sulfide nanosheets prepared via a single-source precursor approach. *Crystal Growth and Design* **2008**, *8*, 1023-1030.

3. Oxygen Reduction Reaction Catalyzed by Nitrogen-Doped Carbon with Iron and Cobalt Metal Sites

3.1 Abstract

The tunable structures and electronic properties of doped carbon materials make them promising electrocatalysts towards oxygen reduction reaction (ORR), a critical process in various electrochemical energy technologies. In this study, Fe/Co co-doped carbon cages were synthesized using hard silica templates that were coated with a melamine-formaldehyde resin and doped with different Fe and Co precursors at varying ratios. Electron microscopy studies confirmed the formation of hollow carbon cages, while X-ray photoelectron spectroscopy analysis revealed an elemental composition of mostly carbon, oxygen, and nitrogen, with a total metal content of about 1.0-1.5% and charge transfer from Fe to Co. Such metal-metal interaction was influenced by the Co precursor, occurring between oxidized states of the metals in the metallic phases when complexes such as $Na_3[Co(NO_2)_6]$ and $[Co(im)_4](NO_3)_2$ are used. By changing the Co precursor it also accompanied changes in the Tafel slopes, indicating changes in the catalytic mechanism as a result of the electronic structure of the active sites.

3.2 Introduction

Proton exchange membrane fuel cells (PEMFCs) have been gaining much attention as a potential power source for a variety of applications.[1] PEMFCs entail two important reactions, oxidation of small molecule fuels at the anode and reduction of oxygen at the cathode, and the device performance is largely dictated by the oxygen reduction reaction (ORR), thanks to its notoriously sluggish electron-transfer kinetics and complex reaction pathways.[2] Thus it is critical to develop efficient catalysts for these reactions such that a sufficiently high current density can be achieved for practical applications. Platinum-based catalysts have been the leading option; yet the low natural abundance and prohibitive cost have limited their

commercial use.[3] An alternative approach is to engineer carbon nanostructures as high-efficiency, low-cost catalysts towards ORR. For instance, nitrogen-doped carbons have been known to show a high electrocatalytic activity for oxygen reduction[4–6] due to modulation of the electronic properties and surface polarities of the carbon skeleton that facilitates oxygen binding and oxygen reduction[7,8] These nitrogen centers embedded on the carbon matrix have shown to influence ORR activity.[9–12] Furthermore, for the development of these carbon-based catalyst, most research is focused on the incorporation of non-noble metals onto a nitrogen doped carbon matrix. [13,14] Upon doping of non-noble metals , they tend to produce a MN_x coordination moieties, generally argued to be the ORR active sites,[15–2223–25] Recently, bimetallic catalyst have proven to be more efficient at catalyzing ORR reaction, compared to its counterparts. This has been correlated to the change of surface charge distribution of active sites significantly improving the electron transfer, thus a more efficient ORR catalyst.,[26–29] To this day, carbon nanostructures doped with iron and cobalt bimetallic centers are among the most promising for ORR electrocatalysis.[31–33] Even then, the catalytic activities are below expectations, still producing sluggish kinetics for ORR. To maximize the active materials for ORR, porosity of the carbon material should further be enhanced. A way to maximize the active site in carbon materials can be done by using a hard template synthesis. Where ordered mesoporous silica, metal oxides, have been employed as hard templates. Using this method, produces well-defined porous structures, high density of active sites exposed on the nanopores, where they can be finely controlled during the carbonization process. Ultimately, leading to an active catalyst. Using silica nanoparticles has shown to produce porous carbon structures with tailoring structures resulting in greater accessibility of the catalytic active site.[31,31,34–39] Because of this, we report the preparation of porous hollow co-doped carbon spheres with bi-metallic centers of Fe and Co, by a facile silica sacrificial hard template. Transmission electron microscopy studies show that the metal centers are most likely atomically dispersed within the carbon matrix, which is further confirmed in X-ray photoelectron/absorption spectroscopy (XPS/XAS) measurements. Due to the Fe-Co

electronic interactions, the resulting FeCo-NC exhibited markedly enhanced ORR activity in alkaline media, as compared to the mono-metal counterparts; significantly, the samples prepared with the $Na_3[Co(NO_2)_6]$ complex stood out as the best among the series.

3.3 Experimental Section

3.3.1 Chemicals

Tetraethyl orthosilicate (TEOS, 98%, Acros Organics), ammonium hydroxide (NH_4OH, 28%, Fisher Scientific), reagent alcohol (EtOH, absolute, Macron Fine Chemicals), melamine (99%, Acros Organics), formaldehyde (37% v/v, Acros Organics), sodium hydroxide (NaOH, Fisher Scientific), ferrous sulfate heptahydrate ($FeSO_4 \cdot 7H_2O$, Fisher Scientific), ferrous chloride tetrahydrate ($FeCl_2 \cdot 4H_2O$, Fisher Scientific), cobalt chloride hexahydrate ($CoCl_2 \cdot 6H_2O$, Fisher Scientific), sodium bisulfate ($NaHSO_4$, Fisher Scientific), hydrofluoric acid (HF, 48%, Fisher Scientific), and Pt/C (20 wt%, Alfa Aesar) were used as received. tetraethylammonium cobalt(II) chloride ($(Et_4N)_2CoCl_4$), tetrakis(imidazole)cobalt(II) nitrate ($[Co(Im)_4](NO_3)_2$), and sodium hexanitrocobaltate(III) ($Na_3[Co(NO_2)_6]$) were prepared previously.[40,41] Water was supplied from a Barnstead Nanopure Water System (18.3 MΩ cm).

3.3.2 Synthesis of silica spheres

SiO_2 nanospheres were synthesized by adopting a literature procedure.[42] In brief, 16 mL of NH_4OH and 0.6 mL of TEOS were added to 240 mL of EtOH to form a clear solution, which was stirred for 16 h at room temperature. The product was collected by centrifugation, vacuum dried, and stored for subsequent use.

3.3.3 Synthesis of melamine formaldehyde resin-coated SiO2 spheres

The SiO_2 nanospheres prepared above were then coated with a melamine formaldehyde (MF) resin, as described previously.[39] In a typical synthesis, 0.567 g of melamine was dissolved in 90 mL of H_2O at 90 °C, into which were then added 37.5 mg of SiO_2 nanospheres, 2.925 µL of formaldehyde, and a catalytic amount of NaOH under magnetic

stirring overnight. The product was collected by centrifugation and vacuum dried to yield SiO_2@MF core@shell structures.

3.3.4 Synthesis of Fe,Co,N-codoped porous carbon

FeCo-NC nanocomposites were then prepared by controlled pyrolysis of the SiO_2@MF obtained above, along with select metal complexes.[43] In brief, 50.0 mg of SiO_2@MF was soaked for several hours in a solution containing the same $FeSO_4$ precursor and varied Co complexes at select concentrations up to 16.0 mM. All solutions were prepared in water, except for $[Co(Im)_4](NO_3)_2$ where it was dissolved in ethanol. The product was centrifuged and vacuum dried before being placed in a tube furnace and heated at 800 °C, for 1 h in a N_2 atmosphere. The obtained black powders were then dispersed into a 10% HF solution under magnetic stirring to remove the SiO_2 templates, yielding Fe,Co and N co-doped (FeCo-NC) porous carbon that were denoted as FeCo-NC-X (X = $CoCl_2$, $Na_3[Co(NO_2)_6]$, $Co(Im)_4(NO_3)_2$)

3.3.5 Characterization

Transmission electron microscopy (TEM) images were acquired with a Philips CM300 microscope operated at 300 kV. Scanning electron microscopy (SEM) images were obtained on a FEI Quanta 3D field emission microscope operated at 10.0 kV. X-ray photoelectron spectroscopy (XPS) studies were conducted on a PHI5400/XPS instrument with an Al K_α source operated at 350 W and 10^{-9} Torr. UV-vis absorption spectra were acquired using a PerkinElmer Lambda 35 UV-vis spectrometer with a 1 cm quartz cuvette. X-ray absorption spectroscopy (XAS) measurements were performed using the Sector 20-BM beamline of the Advanced Photon Source at Argonne National Laboratory.

3.3.6 Electrochemistry

All electrochemical tests were carried out on a CHI710 workstation in a three-electrode configuration. A graphite rod was used as the counter electrode, and a Ag/AgCl electrode in 1.0M KCl was used as the reference electrode. This Ag/AgCl electrode was calibrated

against a reversible hydrogen electrode (RHE), and all potentials in this study are reported in reference to this RHE. A rotating (gold) ring-(glassy carbon) disk electrode (RRDE, Pine Research Instrument) was used as the working electrode. To prepare catalyst inks, 0.8 mg of the FeCo-NC samples prepared above and 2.0 µL nafion were added to 200 µL of a water-ethanol mixture (1:1 v/v). After sonication for at least 30 min, 5.0 µL of the ink was dropcasted onto the glassy carbon disk, corresponding to a catalyst loading of 81.30 µL/cm^2. Once the catalyst layer was dried, 3.0 µL of 20% nafion was added to cover the surface, and the electrode was immersed into electrolyte solutions for electrochemical testing.

3.4 Results and Discussion

In the present study, melamine was used as the main carbon and nitrogen source, which was polymerized onto the silica surface with formaldehyde as the crosslinker.[44] After pyrolysis at the optimal temperature of 800 °C and template removal, FeCo-NC-X [($Na_3[Co(NO_2)_6]$) and FeCo-NC-$[Co(Im)_4](NO_3)_2$], respectively (Figure 3.1, Figure 3.2). As seen in our previous report,[29] FeCo-NC-$CoCl_2$ was synthesized, it was found that the optimal ratio for all of Fe:Co is 1:1 when doped with cobalt complexes Therefore, for this study all Fe:Co samples of 1:1 is investigated. As seen in Figure 1a, FeCo-NC-($Na_3[Co(NO_2)_6]$) shows evidence of the formation of isolated metal nanoparticles. As seen by the HRTEM (Inset Figure 3.1a) lattice spacing of 0.21nm were obtained, which is consistent with metallic Fe.[45–47] Since particles can be seen both on the surface and within the carbon structure, it is reasonable to expect lattice spacings corresponding to metallic states. In addition, a separate lattice spacings of 0.37 could be observed in the carbon matrix, corresponding to spacing between carbon layers and hexagonal graphitic carbon, respectively.[48–50] Upon elemental mapping results from are (Figure 3.1b), one can see Fe particles wrapped around a carbon cage, with their respective atomic composition (Table 3.1). In addition, one can see that nitrogen is also rather evenly dispersed within the carbon skeleton, suggesting a nitrogen doped carbon skeleton.

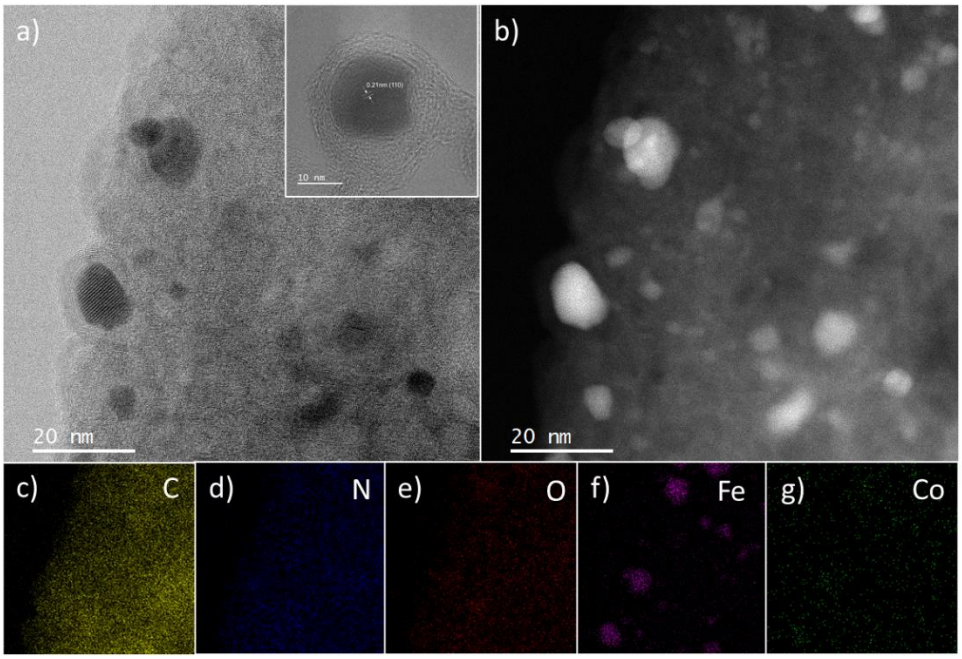

Figure 3.1 Electron microscopy studies. Representative TEM image of (a) FeCo-NC-(Na3[Co(NO2)6]), and its respective HRTEM images and elemental mapping, respectively. (b,c-g)

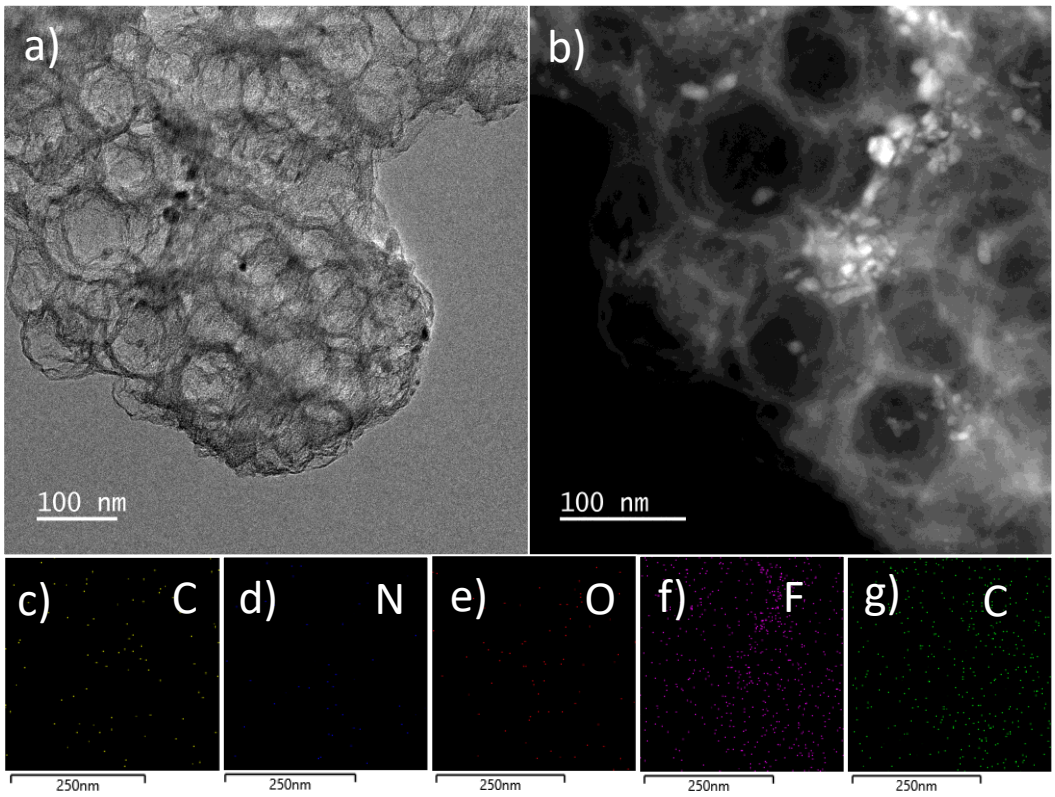

Figure 3.2 Images of FeCo-NC-[Co(im)4](NO3)2 (a-b) TEM and STEM. (c-g) elemental mapping.

Table 3.1 Elemental composition of FeCo-NC-X as determined by EDS.

Sample	C (at. %)	O (at. %)	N (at. %)	Fe (at. %)	Co (at. %)
FeCo-NC-$Na_3[Co(NO_2)_6]$	85.34	0.78	-	13.36	0.51
FeCo-NC-$[Co(im)_4](NO_3)_2$	47.3	30.9	20.1	1.2	0.4

XPS studies were then carried out to investigate the elemental composition and the valence states of the samples. From the survey spectra (Figure 3.3), one can see that the FeCo-NC-X samples are mainly composed of carbon, oxygen, and nitrogen, with trace amounts of iron and cobalt in the doped samples. The amounts of Fe and Co differ between samples, signifying that they are incorporated into the carbon framework to varying degrees (Table 3.2). It is worth noting that although the feed ratio of Fe to Co is less than or equal to one, the final ratio is always greater than one suggesting that iron has a higher affinity for the binding sites in the MF polymer, and forms more stable interactions with the carbon matrix. Table S2 highlights the important result that the amount of both metals is significantly higher in FeCo-NC-Na_3 $[Co(NO_2)_6]$ and FeCo-NC-$[Co(Im)_4](NO_3)_2$. As previously reported,[29] FeCo-NC-$CoCl_2$ exhibited largest atomic percent uptake. Now, with the addition of various cobalt complexes and iron, we see a significantly higher metal content. Furthermore, Comparing the two samples containing only cobalt, FeCo-NC-$CoCl_2$ and FeCo-NC-$Na_3[Co(NO_2)_6]$, the same initial metal concentration yields atomic percentages of 0.05 and 0.22, respectively. This effect is enhanced primarily in the co-doped samples, as exemplified by FeCo-NC-$CoCl_2$ and FeCo-NC-$Na_3[Co(NO_2)_6]$. An important trend that can be observed from Table 3.2 is that the metal uptake is much greater in the FeCo-NC-$Na_3[Co(NO_2)_6]$ and FeCo-NC-$[Co(Im)_4](NO_3)_2$

samples than in those containing a single dopant. Taken together, these observations suggest not only that certain Co complexes can form more permanent interactions with the MF resin, but also that the Fe and Co dopants interact with each other, thereby influencing each other's uptake.

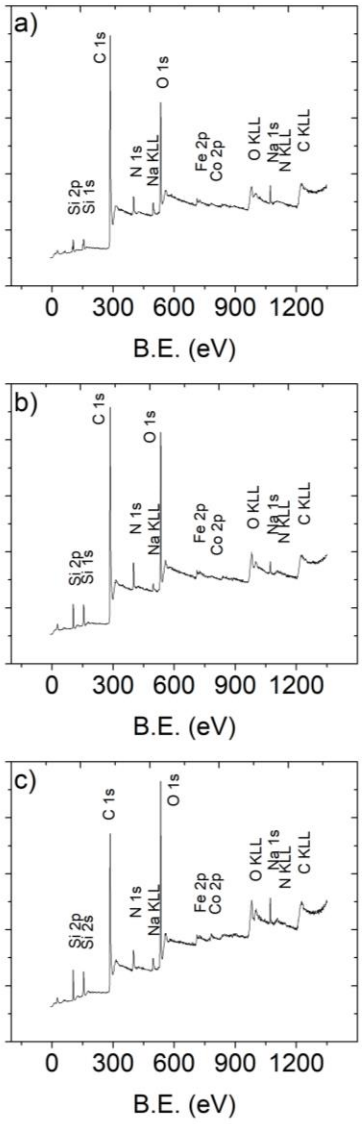

Figure 3.3 XPS survey spectrums. (a) FeCo-NC-CoCl2,(b) FeCo-NC- Na3[Co(NO2)6], and (c) FeCo-NC-[Co(im)4](NO3)2

Table 3.2 Elemental composition of FeCo-NX as determined by XPS. Those highlighted in yellow are single doped CHS with their respective cobalt complex precursors.

Sample	C (at. %)	O (at. %)	N (at. %)	Fe (at. %)	Co (at. %)	Fe:Co ratio
FeCo-NC-$CoCl_2$	64.05	20.62	6.28	0.18	0.40	1.80
FeCo-NC-$Na_3[Co(NO_2)_6]$	82.08	9.51	7.06	0.95	0.37	2.41
FeCo-NC-$[Co(im)_4](NO_3)_2$	86.60	6.83	5.47	0.73		1.95

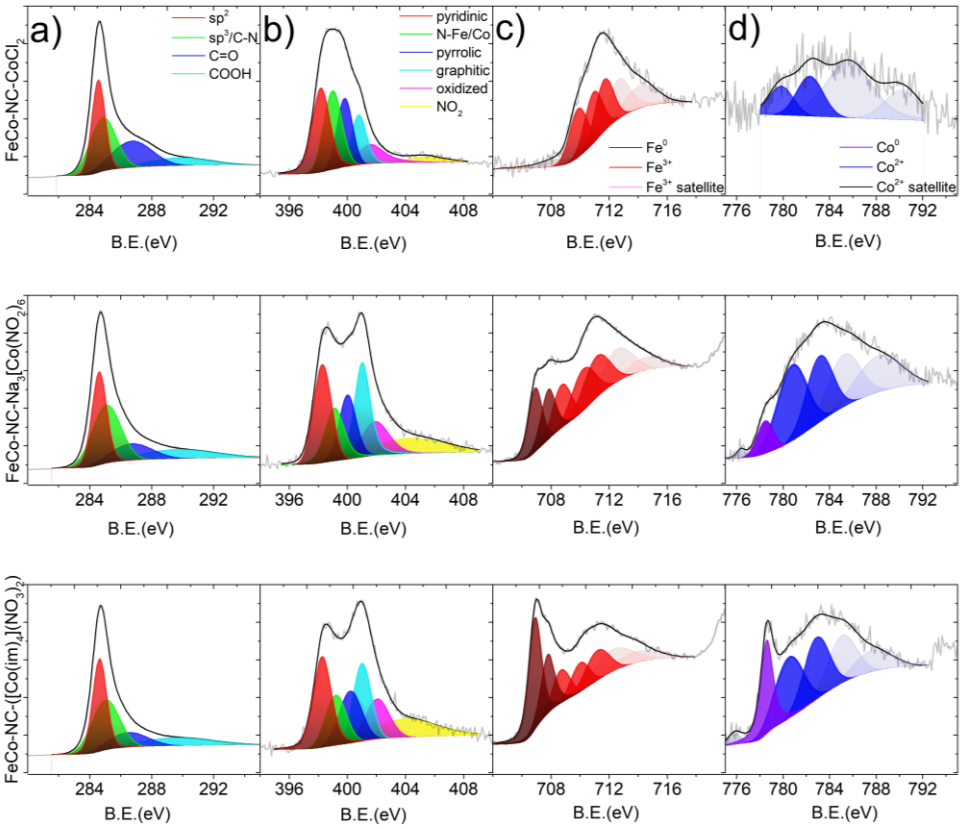

Figure 3.4 High-resolution XPS scans of the (a) C 1s, (b) N 1s, (c) Fe 2p, and (d) Co 2p electrons of different cobalt complex FeCo-NC samples. Grey curves are experimental data, and colored areas are deconvolution fits

Figure 3.4 shows the corresponding high-resolution XPS spectra of the samples. All C 1s spectra are very similar in shape and composition, featuring a sharp peak at 284.6 eV for sp^2 carbon, a broader peak at 285.1 eV for sp^3 carbon (including carbon bonded to nitrogen), and two broad peaks at 286.9 eV and 289.8 eV, corresponding to carbonyl carbon and carboxylic acids, or π - π* transitions.[51,52]

The N 1s spectra in Figure 3.4b can be fitted with six peaks at 398.2, 399.1, 399.9, 400.9, 401.8, and 403.9 eV (average from the series of samples Table 3.3), with exception of the as prepared CHS, in which the peak at 399.1 eV is not present. The first four peaks can be assigned to pyridinic, metal-bonded, pyrrolic, graphitic, and oxidized nitrogen, respectively, while the broad peak at 403.9 eV is attributed to chemisorbed NO_x.[43,53,54]While

all peaks stay within 0.1 eV between samples, their relative intensities vary. Notably, the M-N peak at 399.1 eV is correlated to the relative amount of oxidized metal in the sample, while entirely absent in the metal-free CHS sample (Figure 3.5a,b), and it has the largest relative contribution to the total N content in FeCo-NC-$CoCl_2$. Additionally, the M-N peak makes a much smaller contribution to the total, with a larger fraction coming from graphitic and pyridinic nitrogen instead. In CHS-$Na_3[Co(NO_2)_6]$,FeCo-NC-$[Co(im)_4](NO_3)_2$, its contribution to the total is significant, albeit not as large as in FeCo-NC-$CoCl_2$, even though their total metal content is much greater (Table 3.2). However, since these samples contain metal nanoparticles, only a fraction of the observed metal will be coordinated to nitrogen centers, while the remainder is located within the particles.

Table 3.3 Binding energies of nitrogen dopants in FeCo-NC-X from XPS measurements.

Sample	**N-Fe/Co**	**Pyridinic N**	**Pyrrolic N**	**Graphitic N**	**Oxidized N**
FeCo-NC-$CoCl_2$	399.01	398.19	399.83	400.80	401.61
FeCo-NC-$Na_3[Co(NO_2)_6]$	399.14	398.30	400.03	401.03	401.94
FeCo-NC-$[Co(im)_4](NO_3)_2$	399.22	398.28	400.22	401.02	402.07

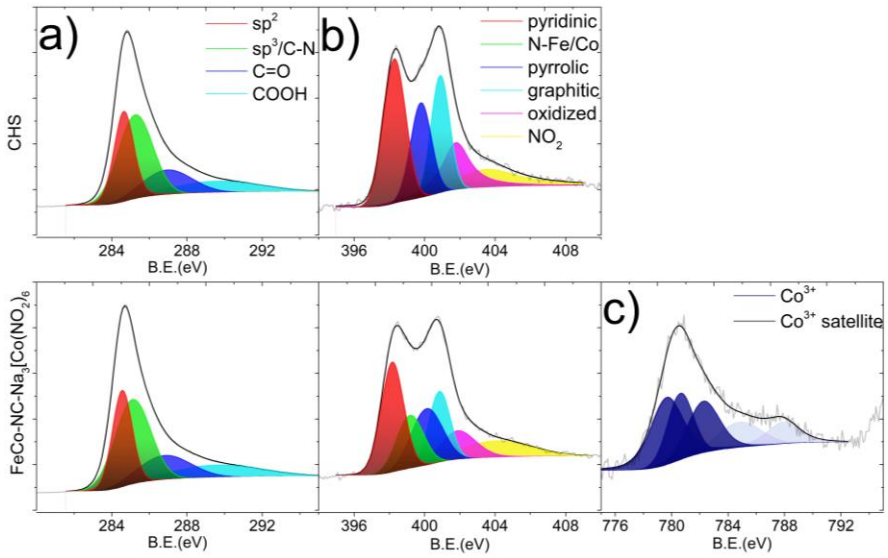

Figure 3.5 . High-resolution XPS scans of the (a) C 1s, (b) N 1s, and (c) Co 2p electrons of different control-FeCo-NC-X samples (Top-CHS, Bottom- FeCo-NC-Na3[Co(NO2)6] . Grey curves are experimental data, and colored areas are deconvolution

For iron and cobalt, the XPS analysis is complicated not only by spin-orbit coupling of the 2p orbitals, producing a $p_{3/2}$ and a $p_{1/2}$ portion of the peak, but also by the spin splitting of the main peak as a result of the unpaired electrons present in the metals. Thus, the different metal species have strongly overlapping signatures. Nevertheless, an attempt has been made to identify the dominant species. For the spin-split peaks, the position of the first peak is reported. The FeCo-NC-$CoCl_2$ consists of a main peak, spin-split into three, as well as two satellites. The number of peaks and their position at 709.9 eV are consistent with a rather low Fe^{3+}.[55,56] This suggests that the sample consists of iron in between the two oxidation states, such as Fe^{2+} in an electron-withdrawing environment. In FeCo-NC-$Na_3[Co(NO_2)_6]$ and FeCo-$NCSO_4$-$[Co(im)_4](NO_3)_2$ there are not only oxidized Fe species, but also characteristic peaks of metallic Fe, in agreement with the obtained TEM images (Table 3.4). The oxidized species appear at 708.6 eV, only slightly higher than Fe^{2+}, and the sharp metallic peak is easily identified at 706.9 eV. Surprisingly, both spectra also contain an additional peak at 707.8 eV,

which cannot be assigned to any single species, and any attempts at a fitting without this peak were unsuccessful. Its position suggests that this peak belongs to Fe in between the 0 and 2+ states, similar to what was observed previously. In this case, the shift falls in between the natural gap that exists between the Fe^0 and Fe^{2+} peaks, allowing for its resolution as a separate peak. This implies that in these two samples, there is an electron-withdrawing element that interacts with the metallic phase of Fe, while in FeCo-NCSO_4-$CoCl_2$, in the absence of metallic Fe, an interaction occurs instead with Fe^{2+}.

Table 3.4 Metal binding energies of the first peaks and atomic percentages from XPS measurements.

	Fe $2p_{3/2}$ B.E. (eV)	**Fe(0) at%**	**Co B.E. (eV)**	**Co(0) at%**
FeCo-NC-$CoCl_2$	709.90	-	781.96	-
FeCo-NC-$Na_3[Co(NO_2)_6]$	706.92	0.28	780.79	0.03
FeCo-NC-$[Co(im)_4](NO_3)_2$	706.91	0.33	780.52	0.08

The analysis of the Co spectra is subject to the additional complications caused by the low abundance of Co in the samples. The resulting noise makes any precise fitting impossible, and the peak positions obtained can merely provide general trends. Furthermore, the first peak of Co^{2+} is at 780.4 eV in $Co(OH)_2$ and at 780.0 eV in CoO, while that of Co^{3+} in Co_3O_4 is at 779.6 eV,[56] making it impossible to distinguish between them by means of the main peak position alone for all others. Here, the number of peaks producing the best fit and the intensities of the satellite peaks were used to obtain an indication of the oxidation state. The most straightforward results were obtained for FeCo-NC-$Na_3[Co(NO_2)_6]$, with the first peak at 779.6 eV, and three spin-split components and two satellites, which is consistent with

Co^{3+} and matches the initial oxidation state of the complex used. From our previous report FeCo-NC-$CoCl_2$, the initial peak is at 779.5 eV, which suggests that some $CoCl_2$ may have been oxidized to Co^{3+}, however, the large satellite features are characteristic of Co^{2+}, and the intensity of the peaks is too low for a precise determination. In addition to the peaks associated with oxidized Co, the spectra of FeCo-NC-$Na_3[Co(NO_2)_6]$ and especially FeCo-NC-$[Co(im)_4](NO_3)_2$ contain peaks that can be assigned to metallic Co. The main metallic peak is located at 776.4 eV, slightly higher than the expected value of 776.2 eV, and the smaller LMM B Auger peak at 766.2 eV typically present in metallic Co is also observed. The oxidized Co peaks appear at 780.5 and 780.7 eV, respectively, which are higher than the binding energies observed for other samples, but still consistent with species of Co^{2+},[56,57]while the intense satellite structures are also characteristic of Co^{2+} species. This suggests that these cobalt species are more reduced than the Co^{3+} observed in CHS-$Na_3[Co(NO_2)_6]$ (Figure 3.5), indicating that they gained electrons. Combined, the XPS results show that when both metals are present in a sample, there are Fe species that are more oxidized and Co species that are more reduced, compared to their monometallic counterparts. This suggests that a charge transfer is taking place, whose direction from Fe to Co is consistent with their relative electron affinities.

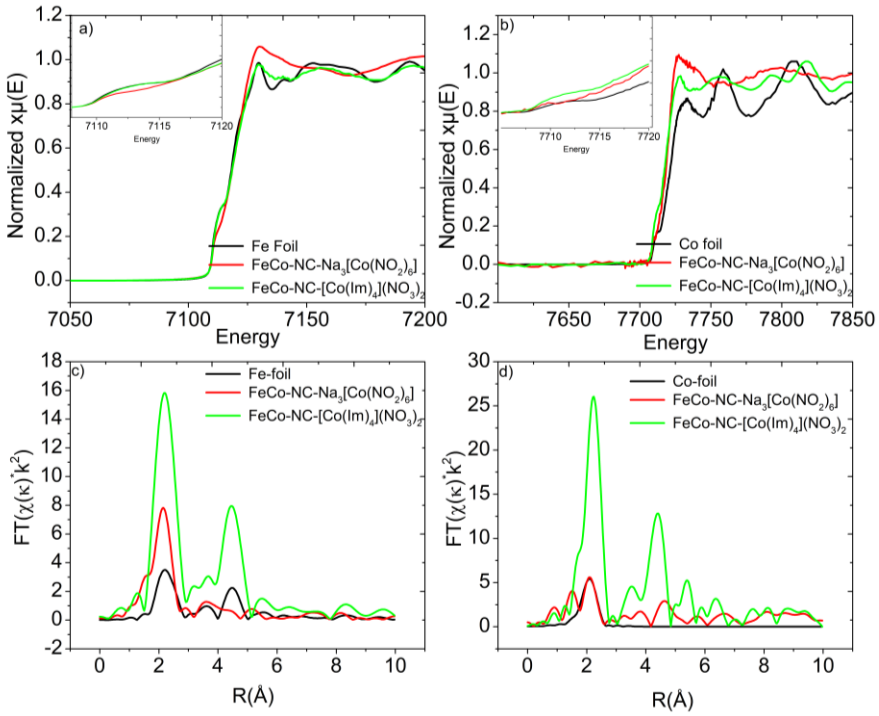

Figure 3.6 . X-ray absorption spectroscopic studies. (a) Iron normalized X-ray absorption near edge structure data for FeCo-NC-X (NC-X(Na3[Co(NO2)6], Co(im)4](NO3)2samples. (b) Cobalt normalized X-ray absorption near edge structure data for FeCo-NC-X((Na3[Co(NO2)6, $Co(im)_4](NO_3)_2$ samples, with their respective reference foil samples.(c,d) Fourier transform extended X-ray adsorption fine structure data for FeCo-NC-X samples.

The Fe K-edge X ray absorption near-edge structure (XANES) analysis was conducted for FeCo-NC-X($Na_3[Co(NO_2)_6]$, $Co(im)_4](NO_3)_2$, as seen in Figure 3.6a,b. The Fe XANES curves in Figure 3.6a shows a pre-edge area at 7114eV, implying that $[Co(im)_4](NO_3)_2$ complex has a similar feature compared to that of Fe foil indicative of being in a metallic state.[58] Whereas, ($Na_3[Co(NO_2)_6]$) pre-edge shows some characteristic of metallic and non-metallic state. Additionally, the absorption edge energy of FeCo-NC-$Na_3[Co(NO_2)_6$ is slightly higher than FeCo-NC- $[Co(im)_4](NO_3)_2$ compared to that of Fe foil, which is

indicative of a higher degree of oxidation state. Additionally, the Co K-edge displays a pre-edge peak at 7714eV and as seen in Fe K-edge, similarly it shows that all Co atoms are in various oxidation states. Both figure 3.6a,b show a zoomed-in inset of the pre-edge area for Fe and Co XANES, respectively. These results confirm the presence of Fe in various oxidation states from Fe^{0} up to Fe^{3+}/Fe^{2+} as suggested by XPS measurements (Figure 3.4) and TEM (Figure 3.1).

The corresponding extended X-ray absorption fine structure (EXAFS) spectra of Fe and Co are depicted in Figure (c,d) for FeCo-NC-X($Na_3[Co(NO_2)_6]$, $Co(im)_4](NO_3)_2$ respectively. In Figure 3.6c, the Fe foil displays a predominant peak around 2.3 Å and 4.5 Å. These spectral features were also seen in all FeCo-NC-X samples, indicating that there is a Metal-Metal (M-M) interaction between them (i.e. Fe-Fe, Fe-Co) and further agreement with FeCo-NC- $Na_3[Co(NO_2)_6]$ TEM Figure 3.1. Additionally, FeCo-NC- $Na_3[Co(NO_2)_6]$ exhibited a peak around 1.5 Å corresponding to Fe-N bond length, which is consistent with a coordination number of 3 (Table 3.5), suggesting that this sample had a significant number of FeN_3 Moeities, which are known to be active for ORR However FeCo-NC- $Co(im)_4](NO_3)_2$ showed no interaction of Fe-N, suggesting a reason for its lower kinetics for ORR. Moreover, Figure 3.6d displays the Co-EXAFS when fitted with M-N shell for all three 3 samples. FeCo-NC- $Na_3[Co(NO_2)_6]$ and FeCo-NC-$((Et_4N)_2CoCl_4)$ exhibited a predominant peak correlated to Co-N at 1.95 Å, whereas FeCo-NC-$Co(im)_4](NO_3)_2$ was a bit longer at 2.06 Å. Interestingly, FeCo-NC-$(Na_3[Co(NO_2)_6]$ was the only sample that demonstrated an interaction between both shells Fe-N and Co-N. In summary, EXAFS results suggest that the interaction between metallic Fe and Co have an influence on a Metallic-Metallic state interaction and forming a FeN_3 moiety. Where both are known to play a critical role in ORR.

Table 3.5 Structural parameters extracted from EXAFS fitting (S02 = 0.80)

Sample	Shell	C.N.	R (Å)	σ^2 (10^{-3} Å^2)	ΔE_0 (eV)
Fe foil[ref]	Fe-Fe	8 (fixed)	2.48(1)	1.4(2)	2.4(1)
	Fe-Fe	6 (fixed)	2.87(2)	7.8(2)	
FeCo-NC- $Na_3[Co(NO_2)_6]$	Fe–N	6(4)	1.95(1)	6.3(3)	-7(1)
	Fe-Fe	4(1)	2.51(1)	6(2)	-7(3)
FeCo-NC-$[Co(im)_4](NO_3)_2$	Co–N	2.7(9)	2.06(1)	5(1)	10(1)
	Fe-Fe	5(1)	2.49(2)	2(2)	10(3)

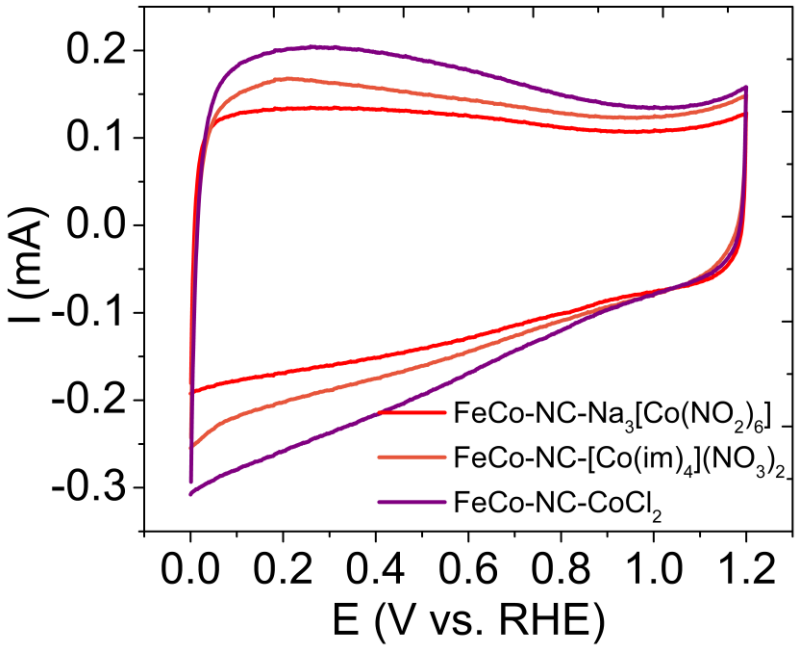

Figure 3.7. CHS-X samples with a potential scan rate of 10 mV/s in an O2-saturated 0.1 M KOH

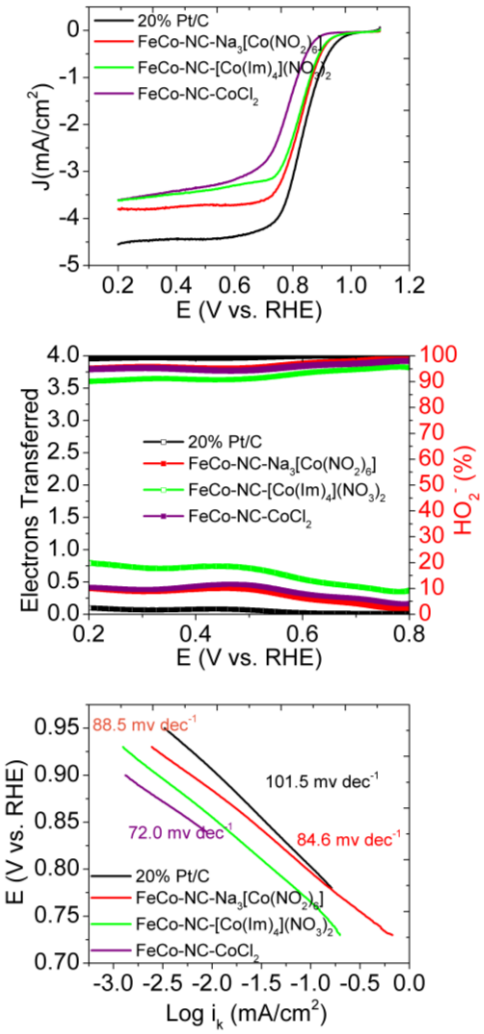

Figure 3.8 Electrochemical characterization of various FeCo-NC-X (CoCl2, Na3[Co(NO2)6] and [Co(im)4](NO3)2, samples (a) Polarization curves obtained at 10 mV/s and 1600 rpm in O2-saturated 0.1M KOH. (b) Electron transferred (top, black arrow) and H2O2 yield (bott bottom, red arrow) vs. Potentials for various samples in (a). (c) Tafel plot curves of the various samples from (a).

Electrochemical measurements were then conducted to evaluate their electrocatalytic performance towards ORR. Figure 3.8 shows the cyclic voltammetry (CV) curves of the dual-doped FeCo-NXwhere all exhibit a large CV area. The electrocatalytic performance of the samples was then evaluated in RRDE measurements. From the polarization curves in Figure

8a, it is evident that our previous reported controlled cobalt sample (FeCo-NC-$CoCl_2$) exhibited a poor activity (E_{onset} = +0.93 V, $E_{1/2}$ = +0.81 V). Additionally, Upon changing the Co precursor to (FeCo-NC-[$Co(im)_4$](NO_3)$_2$ and FeCo-NC-[$Co(im)_4$](NO_3)$_2$)) it was accompanied by an unprecedented change in electrocatalytic performance as seen by both FeCo-$NCSO_4$-[$Co(im)_4$](NO_3)$_2$ (E_{onset} = +0.98 V, $E_{1/2}$ = +0.81V) and FeCo-$NCSO_4$-Na_3[$Co(NO_2)_6$] (E_{onset} = +0.98 V, $E_{1/2}$ = +0.82 V). In these two samples, the electrocatalytic performance significantly enhanced and was close to that of commercial Pt. Consistent behaviors can be seen in the electron transfer numbers in Figure 4b with their respective H_2O_2 % yield.

In addition, Figure 3.8c shows the Tafel plots, where the Tafel slopes are 72.0, 84.6, 88.5, and 101.5 mv dec^{-1}, respectively. Furthermore, In (FeCo-NC-[$Co(im)_4$](NO_3)$_2$ and FeCo-NC-[$Co(im)_4$](NO_3)$_2$)) electrocatalytic performance significantly enhanced and close to commercial Pt, while electron transfer numbers remain largely unchanged and Tafel plots show improvements in exchange current density, now surpassing Pt, but with similar slopes. This indicates that the reaction still proceeds through the same pathway, and the reason for the performance gain must be a direct consequence of an increased activity at the active sites within the material. In fact, the catalytic activity of the samples correlates well with their overall metal content (Table 3.2), providing further evidence that the metals play a key role in the electrocatalytic performance.

To confirm that the material maintains its catalytic properties during use, a stability test was conducted by cycling the potential for an extended period. The results in Figure 3.9 show that there is no discernible difference between the initial voltametric profile and that after 10,000 cycles, confirming that the material is stable enough to endure prolonged exposure to this potential range In a separate experiment, the electrolyte was poisoned with 10 mM KSCN (Figure 3.10). The thiocyanate anion is known to bind strongly and selectively to metal centers, both in particle and in atomically dispersed form, blocking access to potential active sites. [59] If these metal centers are directly involved in the catalytic process,

the KSCN therefore renders the catalyst inactive, providing insight into the nature of the catalytically active sites. [60,61] Therefore, suggesting that the metal nanoparticles have a great influence on the catalytic activity.

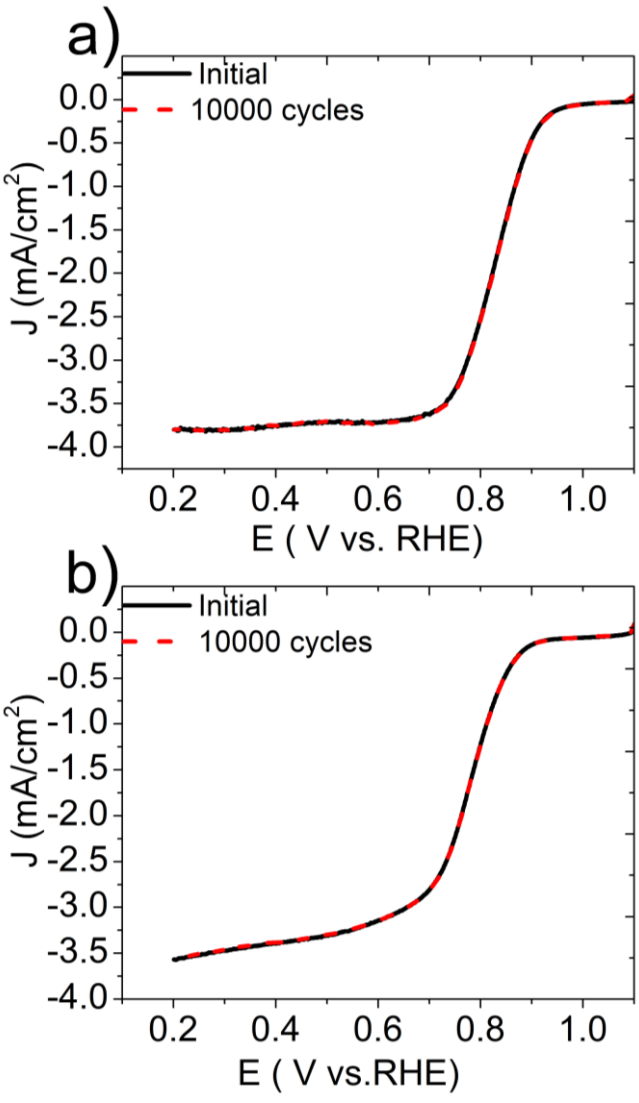

Figure 3.9 . Results of a 10,000-cycle stability test conducted with (a)CHS-Fe-CHS-Na3[Co(NO2)6] (b) CHS-Fe-[Co(im)4](NO3)2 (samples at 1600 rpm and a potential scan rate of 10 mV/s in an O2-saturated 0.1 M KOH solution

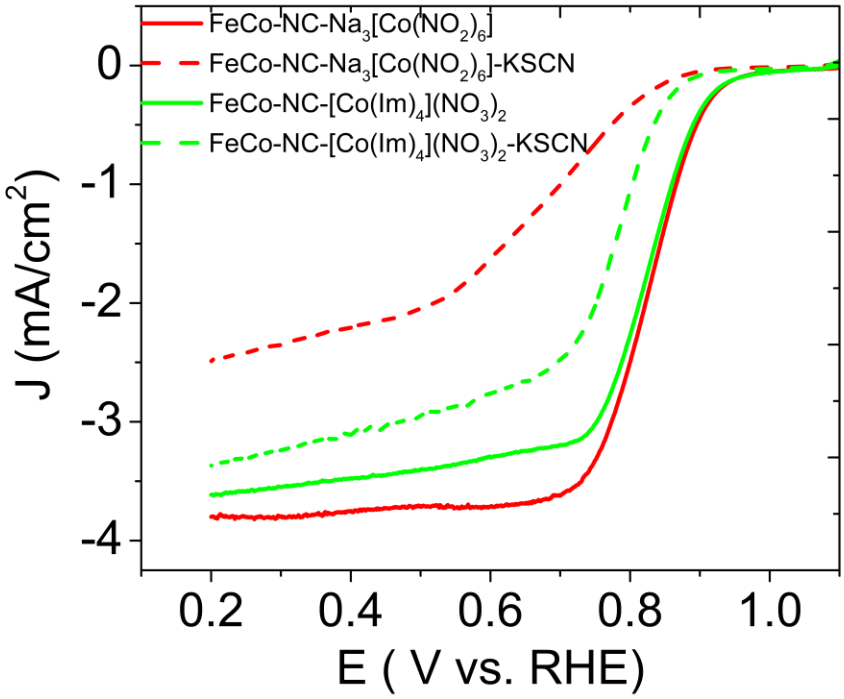

Figure 3.10 KSCN polarization curves of CHS-Na3[Co(NO2)6] and CHS-Fe-[Co(im)4](NO3)2 samples at 1600 rpm and a potential scan rate of 10 mV/s in an O2-saturated 0.1 M KOH solution

3.5 Conclusion

In this study, Fe and Co dual doped CHS were prepared. It was found that Co complex precursors had a strong influence on the structure and chemical composition of the material, and hence its catalytic performance. Not only do they influence the extent of each other's uptake into the carbon framework, they also influence their relative positions within the matrix. XPS results suggest the presence of individual, N – coordinated metal centers in all tested samples. Using Co complexes instead of $CoCl_2$ yields structures with much higher metal contents, and a much stronger interaction between Fe and Co, leading to nanoparticle formation. Notably, XPS suggests that the charge transfer attributed to the interaction between Fe and Co now occurs between the metallic phases of the two, which is constituent

with TEM observations. Thus, the significant enhancement of catalytic activity in the complex-doped samples is a result of both the higher metal abundance and the different interaction between Fe and Co. These results demonstrate that the activity of Fe/Co co-doped catalysts is influenced by the nature of the precursors used, thus resulting in metal nanoparticles as they deposit and affect the metal uptake into the carbon skeleton.

3.6 References

(1) Zhou, X.; Qiao, J.; Yang, L.; Zhang, J. A Review of Graphene-Based Nanostructural Materials for Both Catalyst Supports and Metal-Free Catalysts in PEM Fuel Cell Oxygen Reduction Reactions. *Adv Energy Mater* **2014**, *4* (8), 1301523. https://doi.org/10.1002/aenm.201301523.

(2) Ozoemena, K. I. Nanostructured Platinum-Free Electrocatalysts in Alkaline Direct Alcohol Fuel Cells: Catalyst Design, Principles and Applications. *Rsc Adv* **2016**, *6* (92), 89523–89550. https://doi.org/10.1039/c6ra15057h.

(3) Fernández, J. L.; Raghuveer, V.; Manthiram, A.; Bard, A. J. Pd-Ti and Pd-Co-Au Electrocatalysts as a Replacement for Platinum for Oxygen Reduction in Proton Exchange Membrane Fuel Cells. *J Am Chem Soc* **2005**, *127* (38), 13100–13101.

(4) Ai, K.; Liu, Y.; Ruan, C.; Lu, L.; Lu, G. M. Sp 2 C-Dominant N-Doped Carbon Sub-Micrometer Spheres with a Tunable Size: A Versatile Platform for Highly Efficient Oxygen-Reduction Catalysts. *Adv Mater* **2012**, *25* (7), 998–1003. https://doi.org/10.1002/adma.201203923.

(5) Gong, K.; Du, F.; Xia, Z.; Durstock, M.; Dai, L. Nitrogen-Doped Carbon Nanotube Arrays with High Electrocatalytic Activity for Oxygen Reduction. *Sci New York N Y* **2009**, *323* (5915), 760–764. https://doi.org/10.1126/science.1168049.

(6) Liu, J.; Qiao, S. Z.; Budi Hartono, S.; Lu, G. Q. M. Innentitelbild: Monodisperse Yolk-Shell Nanoparticles with a Hierarchical Porous Structure for Delivery Vehicles and Nanoreactors (Angew. Chem. 29/2010). *Angew Chem-ger Edit* **2010**, *122* (29), 4958–4958. https://doi.org/10.1002/ange.201002660.

(7) Masa, J.; Xia, W.; Muhler, M.; Schuhmann, W. On the Role of Metals in Nitrogen-Doped Carbon Electrocatalysts for Oxygen Reduction. *Angewandte Chemie Int Ed* **2015**, *54* (35), 10102–10120. https://doi.org/10.1002/anie.201500569.

(8) Li, Y.; Zhao, Y.; Cheng, H.; Hu, Y.; Shi, G.; Dai, L.; Qu, L. Nitrogen-Doped Graphene Quantum Dots with Oxygen-Rich Functional Groups. *J Am Chem Soc* **2011**, *134* (1), 15–18. https://doi.org/10.1021/ja206030c.

(9) Ferrero, G. A.; Diez, N.; Sevilla, M.; Fuertes, A. B. Iron–Nitrogen-Doped Dendritic Carbon Nanostructures for an Efficient Oxygen Reduction Reaction. *Acs Appl Energy Mater* **2018**, *1* (11), 6560–6568. https://doi.org/10.1021/acsaem.8b01457.

(10) Leonard, N. D.; Wagner, S.; Luo, F.; Steinberg, J.; Ju, W.; Weidler, N.; Wang, H.; Kramm, U. I.; Strasser, P. Deconvolution of Utilization, Site Density, and Turnover Frequency of Fe–Nitrogen–Carbon Oxygen Reduction Reaction Catalysts Prepared with Secondary N-Precursors. *Acs Catal* **2018**, *8* (3), 1640–1647. https://doi.org/10.1021/acscatal.7b02897.

(11) Qian, Y.; Du, P.; Wu, P.; Cai, C.; Gervasio, D. F. Chemical Nature of Catalytic Active Sites for the Oxygen Reduction Reaction on Nitrogen-Doped Carbon-Supported Non-Noble Metal Catalysts. *J Phys Chem C* **2016**, *120* (18), 9884–9896. https://doi.org/10.1021/acs.jpcc.6b02670.

(12) Yang, W.; Peng, Y.; Zhang, Y.; Lu, J. E.; Li, J.; Chen, S. Air Cathode Catalysts of Microbial Fuel Cell by Nitrogen-Doped Carbon Aerogels. *Acs Sustain Chem Eng* **2018**, *7* (4), 3917–3924. https://doi.org/10.1021/acssuschemeng.8b05000.

(13) Fang, X.; Zhao, X.; Fang, W.; Chen, C.; Zheng, N. Self-Templating Synthesis of Hollow Mesoporous Silica and Their Applications in Catalysis and Drug Delivery. *Nanoscale* **2013**, *5* (6), 2205–2218. https://doi.org/10.1039/c3nr34006f.

(14) Choi, C. H.; Park, S. H.; Woo, S. I. Binary and Ternary Doping of Nitrogen, Boron, and Phosphorus into Carbon for Enhancing Electrochemical Oxygen Reduction Activity. *Acs Nano* **2012**, *6* (8), 7084–7091. https://doi.org/10.1021/nn3021234.

(15) Proietti, E.; Jaouen, F.; Lefèvre, M.; Larouche, N.; Tian, J.; Herranz, J.; Dodelet, J. Iron-Based Cathode Catalyst with Enhanced Power Density in Polymer Electrolyte Membrane Fuel Cells. *Nat Commun* **2011**, *2* (1), 416. https://doi.org/10.1038/ncomms1427.

(16) Schulenburg, H.; Stankov, S.; Schünemann, V.; Radnik, J.; Dorbandt, I.; Fiechter, S.; Bogdanoff, P.; Tributsch, H. Catalysts for the Oxygen Reduction from Heat-Treated Iron(III) Tetramethoxyphenylporphyrin Chloride: Structure and Stability of Active Sites. *J Phys Chem B* **2003**, *107* (34), 9034–9041. https://doi.org/10.1021/jp030349j.

(17) Zhou, Q.; Li, C. M.; Li, J.; Lu, J. Electrocatalysis of Template-Electrosynthesized Cobalt−Porphyrin/Polyaniline Nanocomposite for Oxygen Reduction. *J Phys Chem C* **2008**, *112* (47), 18578–18583. https://doi.org/10.1021/jp8077375.

(18) Maldonado, S.; Stevenson, K. J. Direct Preparation of Carbon Nanofiber Electrodes via Pyrolysis of Iron(II) Phthalocyanine: Electrocatalytic Aspects for Oxygen Reduction. *J Phys Chem B* **2004**, *108* (31), 11375–11383. https://doi.org/10.1021/jp0496553.

(19) Wu, G.; More, K.; Johnston, C.; Zelenay, P. High-Performance Electrocatalysts for Oxygen Reduction Derived from Polyaniline, Iron, and Cobalt. *Science* **2011**, *332* (6028), 443–447. https://doi.org/10.1126/science.1200832.

(20) Chlistunoff, J. RRDE and Voltammetric Study of ORR on Pyrolyzed Fe/Polyaniline Catalyst. On the Origins of Variable Tafel Slopes. *J Phys Chem C* **2011**, *115* (14), 6496–6507. https://doi.org/10.1021/jp108350t.

(21) Wu, G.; Artyushkova, K.; Ferrandon, M.; Kropf, A.; Myers, D.; Zelenay, P. Performance Durability of Polyaniline-Derived Non-Precious Cathode Catalysts. **2009**, 1299–1311. https://doi.org/10.1149/1.3210685.

(22) Jaouen, F.; Lefèvre, M.; Dodelet, J.; Cai, M. Heat-Treated Fe/N/C Catalysts for O2 Electroreduction: Are Active Sites Hosted in Micropores? *J Phys Chem B* **2006**, *110* (11), 5553–5558. https://doi.org/10.1021/jp057135h.

(23) Shi, Z.; Liu, H.; Lee, K.; Dy, E.; Chlistunoff, J.; Blair, M.; Zelenay, P.; Zhang, J.; Liu, Z. Theoretical Study of Possible Active Site Structures in Cobalt- Polypyrrole Catalysts for Oxygen Reduction Reaction. *J Phys Chem C* **2011**, *115* (33), 16672–16680. https://doi.org/10.1021/jp2027719.

(24) Strickland, K.; Miner, E.; Jia, Q.; Tylus, U.; Ramaswamy, N.; Liang, W.; Sougrati, M.; Jaouen, F.; Mukerjee, S. Highly Active Oxygen Reduction Non-Platinum Group Metal Electrocatalyst without Direct Metal–Nitrogen Coordination. *Nat Commun* **2015**, *6* (1), 7343. https://doi.org/10.1038/ncomms8343.

(25) Chung, H.; Won, J.; Zelenay, P. Active and Stable Carbon Nanotube/Nanoparticle Composite Electrocatalyst for Oxygen Reduction. *Nat Commun* **2013**, *4* (1), 1922. https://doi.org/10.1038/ncomms2944.

(26) Fu, G.; Liu, C.; Zhang, Q.; Chen, Y.; Tang, Y. Polyhedral Palladium–Silver Alloy Nanocrystals as Highly Active and Stable Electrocatalysts for the Formic Acid Oxidation Reaction. *Sci Rep-uk* **2015**, *5* (1), 13703. https://doi.org/10.1038/srep13703.

(27) Bu, L.; Zhang, N.; Guo, S.; Zhang, X.; Li, J.; Yao, J.; Wu, T.; Lu, G.; Ma, J.; Su, D.; Huang, X. Biaxially Strained PtPb/Pt Core/Shell Nanoplate Boosts Oxygen Reduction Catalysis. *Science* **2016**, *354* (6318), 1410–1414. https://doi.org/10.1126/science.aah6133.

(28) Zhu, Z.; Zhai, Y.; Dong, S. Facial Synthesis of PtM (M = Fe, Co, Cu, Ni) Bimetallic Alloy Nanosponges and Their Enhanced Catalysis for Oxygen Reduction Reaction. *Acs Appl Mater Inter* **2014**, *6* (19), 16721–16726. https://doi.org/10.1021/am503689t.

(29) Mercado, R.; Wahl, C.; Lu, J. E.; Zhang, T.; Lu, B.; Zhang, P.; Lu, J. Q.; Allen, A.; Zhang, J. Z.; Chen, S. Nitrogen-Doped Porous Carbon Cages for Electrocatalytic Reduction of Oxygen: Enhanced Performance with Iron and Cobalt Dual Metal Centers. *Chemcatchem* **2020**, *12* (12), 3230–3239. https://doi.org/10.1002/cctc.201902324.

(30) Xue, H.; Tang, J.; Gong, H.; Guo, H.; Fan, X.; Wang, T.; He, J.; Yamauchi, Y. Fabrication of PdCo Bimetallic Nanoparticles Anchored on Three-Dimensional Ordered N-Doped Porous Carbon as an Efficient Catalyst for Oxygen Reduction Reaction. *Acs Appl Mater Inter* **2016**, *8* (32), 20766–20771. https://doi.org/10.1021/acsami.6b05856.

(31) Lu, B.; Guo, L.; Wu, F.; Peng, Y.; Lu, J.; Smart, T.; Wang, N.; Finfrock, Y.; Morris, D.; Zhang, P.; Li, N.; Gao, P.; Ping, Y.; Chen, S. Ruthenium Atomically Dispersed in Carbon Outperforms Platinum toward Hydrogen Evolution in Alkaline Media. *Nat Commun* **2019**, *10* (1), 631. https://doi.org/10.1038/s41467-019-08419-3.

(32) Zitolo, A.; Goellner, V.; Armel, V.; Sougrati, M.; Mineva, T.; Stievano, L.; Fonda, E.; Jaouen, F. Identification of Catalytic Sites for Oxygen Reduction in Iron- and Nitrogen-Doped Graphene Materials. *Nat Mater* **2015**, *14* (9), 937–942. https://doi.org/10.1038/nmat4367.

(33) Yi, J.; Xu, R.; Wu, Q.; Zhang, T.; Zang, K.; Luo, J.; Liang, Y.; Huang, Y.; Cao, R. Atomically Dispersed Iron–Nitrogen Active Sites within Porphyrinic Triazine-Based Frameworks for Oxygen Reduction Reaction in Both Alkaline and Acidic Media. *Acs Energy Lett* **2018**, *3* (4), 883–889. https://doi.org/10.1021/acsenergylett.8b00245.

(34) Yang, W.; Fellinger, T.; Antonietti, M. Efficient Metal-Free Oxygen Reduction in Alkaline Medium on High-Surface-Area Mesoporous Nitrogen-Doped Carbons Made from Ionic Liquids and Nucleobases. *J Am Chem Soc* **2010**, *133* (2), 206–209. https://doi.org/10.1021/ja108039j.

(35) Niu, W.; Li, L.; Liu, X.; Wang, N.; Liu, J.; Zhou, W.; Tang, Z.; Chen, S. Mesoporous N-Doped Carbons Prepared with Thermally Removable Nanoparticle Templates: An Efficient Electrocatalyst for Oxygen Reduction Reaction. *J Am Chem Soc* **2015**, *137* (16), 5555–5562. https://doi.org/10.1021/jacs.5b02027.

(36) Niu, W.; Li, L.; Liu, J.; Wang, N.; Li, W.; Tang, Z.; Zhou, W.; Chen, S. Graphene-Supported Mesoporous Carbons Prepared with Thermally Removable Templates as Efficient Catalysts for Oxygen Electroreduction. *Small* **2016**, *12* (14), 1900–1908. https://doi.org/10.1002/smll.201503542.

(37) Niu, W.; Li, L.; Wang, N.; Zeng, S.; Liu, J.; Zhao, D.; Chen, S. Volatilizable Template-Assisted Scalable Preparation of Honeycomb-like Porous Carbons for Efficient Oxygen Electroreduction. *J Mater Chem A* **2016**, *4* (28), 10820–10827. https://doi.org/10.1039/c6ta03570a.

(38) Wang, X.; Xu, X.; Niu, C.; Meng, J.; Huang, M.; Liu, X.; Liu, Z.; Mai, L. Earth Abundant Fe/Mn-Based Layered Oxide Interconnected Nanowires for Advanced K-Ion Full Batteries. *Nano Lett* **2016**, *17* (1), 544–550. https://doi.org/10.1021/acs.nanolett.6b04611.

(39) Lu, B.; Smart, T.; Qin, D.; Lu, J.; Wang, N.; Chen, L.; Peng, Y.; Ping, Y.; Chen, S. Nitrogen and Iron-Codoped Carbon Hollow Nanotubules as High-Performance Catalysts toward Oxygen Reduction Reaction: A Combined Experimental and Theoretical Study. *Chem Mater* **2017**, *29* (13), 5617–5628. https://doi.org/10.1021/acs.chemmater.7b01265.

(40) Davis, W. J.; Smith, J. Imidazole Complexes with Cobalt(II) Salts. *J Chem Soc Inorg Phys Theor* **1971**, *0* (0), 317–324. https://doi.org/10.1039/j19710000317.

(41) Kandhaswamy, M. A.; Srinivasan, V. Synthesis and Characterization of Tetraethylammonium Tetrachlorocobaltate Crystals. *B Mater Sci* **2002**, *25* (1), 41–45. https://doi.org/10.1007/bf02704593.

(42) Harada, T.; Ikeda, S.; Ng, Y.; Sakata, T.; Mori, H.; Torimoto, T.; Matsumura, M. Rhodium Nanoparticle Encapsulated in a Porous Carbon Shell as an Active Heterogeneous Catalyst for Aromatic Hydrogenation. *Adv Funct Mater* **2008**, *18* (15), 2190–2196. https://doi.org/10.1002/adfm.200701442.

(43) Zhang, R.; He, S.; Lu, Y.; Chen, W. Fe, Co, N-Functionalized Carbon Nanotubes in Situ Grown on 3D Porous N-Doped Carbon Foams as a Noble Metal-Free Catalyst for Oxygen Reduction. *J Mater Chem A* **2015**, *3* (7), 3559–3567. https://doi.org/10.1039/c4ta05735j.

(44) Mou, S.; Lu, Y.; Jiang, Y. A Facile and Cheap Coating Method to Prepare SiO2/Melamine-Formaldehyde and SiO2/Urea-Formaldehyde Composite Microspheres. *Appl Surf Sci* **2016**, *384*, 258–262. https://doi.org/10.1016/j.apsusc.2016.04.156.

(45) Tihay, F.; Pourroy, G.; Richard-Plouet, M.; Roger, A.; Kiennemann, A. Effect of Fischer–Tropsch Synthesis on the Microstructure of Fe–Co-Based Metal/Spinel Composite Materials. *Appl Catal Gen* **2001**, *206* (1), 29–42. https://doi.org/10.1016/s0926-860x(00)00595-0.

(46) Yang, J.; Wang, X.; Li, B.; Ma, L.; Shi, L.; Xiong, Y.; Xu, H. Novel Iron/Cobalt-Containing Polypyrrole Hydrogel-Derived Trifunctional Electrocatalyst for Self-Powered Overall Water Splitting. *Adv Funct Mater* **2017**, *27* (17), 1606497. https://doi.org/10.1002/adfm.201606497.

(47) Tan, X.; Wang, S.; Chen, Y.; Zhou, Y.; Li, Z. Design, Preparation and Characterization of Iron Nitride Magnetic Abrasives. *J Alloy Compd* **2019**, *774*, 443–450. https://doi.org/10.1016/j.jallcom.2018.09.389.

(48) Wu, B.; Li, M.; Xiao, S.; Qu, Y.; Qiu, X.; Liu, T.; Tian, F.; Li, H.; Xiao, S. A Graphyne-like Porous Carbon-Rich Network Synthesized via Alkyne Metathesis. *Nanoscale* **2017**, *9* (33), 11939–11943. https://doi.org/10.1039/c7nr02247f.

(49) Gong, X.; Hu, Q.; Paau, M.; Zhang, Y.; Shuang, S.; Dong, C.; Choi, M. Red-Green-Blue Fluorescent Hollow Carbon Nanoparticles Isolated from Chromatographic Fractions for Cellular Imaging. *Nanoscale* **2014**, *6* (14), 8162–8170. https://doi.org/10.1039/c4nr01453g.

(50) Ponrouch, A.; Goñi, A.; Palacín, M. High Capacity Hard Carbon Anodes for Sodium Ion Batteries in Additive Free Electrolyte. *Electrochem Commun* **2013**, *27*, 85–88. https://doi.org/10.1016/j.elecom.2012.10.038.

(51) Yang, Z.; Xu, M.; Liu, Y.; He, F.; Gao, F.; Su, Y.; Wei, H.; Zhang, Y. Nitrogen-Doped, Carbon-Rich, Highly Photoluminescent Carbon Dots from Ammonium Citrate. *Nanoscale* **2014**, *6* (3), 1890–1895. https://doi.org/10.1039/c3nr05380f.

(52) Kundu, S.; Wang, Y.; Xia, W.; Muhler, M. Thermal Stability and Reducibility of Oxygen-Containing Functional Groups on Multiwalled Carbon Nanotube Surfaces: A Quantitative High-Resolution XPS and TPD/TPR Study. *J Phys Chem C* **2008**, *112* (43), 16869–16878. https://doi.org/10.1021/jp804413a.

(53) Sarapuu, A.; Samolberg, L.; Kreek, K.; Koel, M.; Matisen, L.; Tammeveski, K. Cobalt- and Iron-Containing Nitrogen-Doped Carbon Aerogels as Non-Precious Metal Catalysts for Electrochemical Reduction of Oxygen. *J Electroanal Chem* **2015**, *746*, 9–17. https://doi.org/10.1016/j.jelechem.2015.03.021.

(54) Zhong, H.; Zhang, H.; Liu, S.; Deng, C.; Wang, M. Nitrogen-Enriched Carbon from Melamine Resins with Superior Oxygen Reduction Reaction Activity. *Chemsuschem* **2013**, *6* (5), 807–812. https://doi.org/10.1002/cssc.201200919.

(55) Grosvenor, A.; Kobe, B.; Biesinger, M.; McIntyre, N. Investigation of Multiplet Splitting of Fe 2p XPS Spectra and Bonding in Iron Compounds. *Surf Interface Anal* **2004**, *36* (12), 1564–1574. https://doi.org/10.1002/sia.1984.

(56) Biesinger, M.; Payne, B.; Grosvenor, A.; Lau, L.; Gerson, A.; Smart, R. Resolving Surface Chemical States in XPS Analysis of First Row Transition Metals, Oxides and Hydroxides: Cr, Mn, Fe, Co and Ni. *Appl Surf Sci* **2011**, *257* (7), 2717–2730. https://doi.org/10.1016/j.apsusc.2010.10.051.

(57) Yang, J.; Liu, H.; Martens, W.; Frost, R. Synthesis and Characterization of Cobalt Hydroxide, Cobalt Oxyhydroxide, and Cobalt Oxide Nanodiscs. *J Phys Chem C* **2010**, *114* (1), 111–119. https://doi.org/10.1021/jp908548f.

(58) Huang, Z.; Pan, H.; Yang, W.; Zhou, H.; Gao, N.; Fu, C.; Li, S.; Li, H.; Kuang, Y. In Situ Self-Template Synthesis of Fe–N-Doped Double-Shelled Hollow Carbon Microspheres for

Oxygen Reduction Reaction. *Acs Nano* **2018**, *12* (1), 208–216. https://doi.org/10.1021/acsnano.7b05832.

(59) Wang, Q.; Zhou, Z.; Lai, Y.; You, Y.; Liu, J.; Wu, X.; Terefe, E.; Chen, C.; Song, L.; Rauf, M.; Tian, N.; Sun, S. Phenylenediamine-Based FeN(x)/C Catalyst with High Activity for Oxygen Reduction in Acid Medium and Its Active-Site Probing. *J Am Chem Soc* **2014**, *136* (31), 10882–10885. https://doi.org/10.1021/ja505777v.

(60) Thorum, M.; Hankett, J.; Gewirth, A. Poisoning the Oxygen Reduction Reaction on Carbon-Supported Fe and Cu Electrocatalysts: Evidence for Metal-Centered Activity. *J Phys Chem Lett* **2011**, *2* (4), 295–298. https://doi.org/10.1021/jz1016284.

(61) Varnell, J.; Tse, E.; Schulz, C.; Fister, T.; Haasch, R.; Timoshenko, J.; Frenkel, A.; Gewirth, A. Identification of Carbon-Encapsulated Iron Nanoparticles as Active Species in Non-Precious Metal Oxygen Reduction Catalysts. *Nat Commun* **2016**, *7* (1), 12582. https://doi.org/10.1038/ncomms12582.

4. Nitrogen-doped carbon flowers with Fe and Ni dual metal centers for effective electroreduction of oxygen

4.1 Abstract

Carbon-based nanocomposites have been attracting extensive attention as high-performance catalysts in alkaline media towards the electrochemical reduction of oxygen. Herein, polyacrylonitrile nanoflowers are synthesized via a free-radical polymerization route and used as a structural scaffold and precursor, whereby controlled pyrolysis leads to the ready preparation of carbon nanocomposites (FeNi-NCF) doped with both metal (Fe and Ni) and nonmetal (N) elements. Transmission electron microscopy studies show that the FeNi-NCF composites retain the flower-like morphology, with the metal species atomically dispersed into the flaky carbon petals. Remarkably, despite a similar structure, elemental composition, and total metal content, the FeNi-NCF sample with a high Fe:Ni ratio exhibits an electrocatalytic performance towards oxygen reduction reaction (ORR) in alkaline media that is similar to that by commercial Pt/C, likely due to the Ni to Fe electron transfer that promotes the adsorption and eventually reduction of oxygen, as evidenced in X-ray photoelectron spectroscopic measurements. Results from this study underline the importance of the electronic properties of metal dopants in the manipulation of the ORR activity of carbon nanocomposites.

4.2 Introduction

Development of sustainable energy technologies has been attracting extensive interest, and fuel cells represent a unique viable option [1]. Typical fuel cell operation entails two main reactions, oxidation of small molecule fuels at the anode and reduction of oxygen at the cathode, where appropriate catalysts are needed to generate a current density sufficiently high for practical applications. These are in general based on the platinum group metals (PGM). Nevertheless, the precious nature of PGM has significantly impeded the commercial

implementation of these technologies [2]. In addition, PGM-based catalysts are prone to inactivation by poisoning species (e.g., CO) and structural instability due to Ostwald ripening in long-term operation, which compromise the overall performance [3, 4]. Thus, significant efforts have been dedicated to the development of alternative catalysts, in particular, for the cathodic oxygen reduction reaction (ORR), which has been largely accepted as a significant road block that limits the fuel cell performance. Among these, carbon-based nanocomposites have been recognized as viable electrocatalysts, mostly owing to ready structural engineering that renders it possible to obtain a large surface area, good conductivity, corrosion resistance, and easy modification of its skeleton for both functionalization and hetero doping [5-7]. For instance, heteroatoms such as nitrogen can be readily doped into the carbon matrices, leading to electron redistribution and activation of various atomic sites that is conducive to the adsorption of key ORR intermediates. Thus, doped carbon can exhibit an apparent ORR activity, although it is typically inferior to that of commercial Pt/C benchmark [8, 9]. Improvement of the performance can be achieved with the additional doping of select metal centers, forming MN_x coordination moieties [10-14]. This is primarily attributed to the synergistic tuning of the electronic interactions between the MN_x sites and reaction intermediates [15]. In fact, extensive research has been reported focusing on metal-nitrogen codoped carbon, since the first breakthrough with a Fe-N-C catalyst in 2009 [6, 7, 16].

In recent years, carbon nanocomposites with bimetal dopants have been found to exhibit further improved ORR activity, in comparison to the mono-metal based counterparts, largely due to the unique metal-metal charge transfer that provides a further control of the electronic interactions with ORR intermediates [17, 18]. For instance, carbon nanocomposites doped with Fe/Co [19], Fe/Mn [20], and Fe/Ni [21] have shown a remarkable ORR activity. This can also be aided by the formation of a three-dimensional (3D) porous carbon scaffold, with interconnected micropores, mesopores and macropores that facilitate both the electron transfer involved in ORR and mass transfer of reactants and electrolyte species.

Herein, polyacrylonitrile with a nanoflower morphology was first prepared by free radical polymerization [22], and was transformed into N-doped carbon nanoflowers embedded with Fe/Ni bimetallic centers by controlled pyrolysis with the addition of iron and nickel compounds at varied feeds. It was found that the obtained nanocomposites displayed a significantly improved ORR activity in alkaline media, in comparison to the metal-free counterparts, signifying the critical role of the metal dopants in dictating the electrocatalytic activity.

4.3 Experimental Section

4.3.1 Chemicals

Iron(III) chloride ($FeCl_3$, 97%, Sigma Aldrich), nickel(II) nitrate ($Ni(NO_3)_2$, 99.999%, Sigma Aldrich), azobis(isobutyronitrile) (AIBN, 98%, Sigma Aldrich), acrylonitrile (≥99%, Sigma Aldrich), and Pt/C (20 wt%, Alfa Aesar) were used as received without further treatment. Water was purified with a Barnstead Nano-pure Water System (resistivity 18.3 MΩ cm)

4.3.2 Sample preparation

Polyacrylonitrile with a nanoflower morphology was first prepared by following a free radical polymerization procedure reported previously with modification [22]. Briefly, 4 mL of acrylonitrile was dispersed into 4 mL of acetone, into which was then added 4 mL of AIBN as the initiator. The reaction was run for 2 h in a vial at 70 °C, affording a white powder (PACN-70) after being dried at ambient temperature for 1 d. The sample was then stabilized by thermal treatment in air at 230 °C for 2 h, producing a brown powder denoted as PACN-230.

The obtained PACN-230 was then utilized to prepare Fe/Ni-codoped carbon flowers. Briefly, 20 mg of PACN-230 was sonicated in acetone for 45 min, into which was then added an aqueous solution containing $FeCl_3$ and $Ni(NO_3)_2$ with a total concentration of 3 mM but at varied feed ratios: 1:0, 1:1, 2:1, and 3:1. The mixture was then dried in vacuum, loaded into a tube furnace, and thermally treated at 900 °C in a N_2 atmosphere for 1 h. The produced black

powders were referred to as Fe-NCF and FeNi-NCF (1,2,3), respectively. A control sample (NCF) was also synthesized in the same fashion but in the absence of any metal salts.

4.3.3 Characterization

Transmission electron microscopic (TEM) images were acquired with an aberration corrected Titan FEI electron microscope. Nitrogen sorption isotherms were obtained at 77 K using 99.999% N_2 with an Autosorb iQ2 (Quantachrome) low-pressure gas sorption analyzer. X-ray photoelectron spectroscopic (XPS) studies were performed with a PHI 5000 Versaprobe instrument.

4.3.4 Electrochemical tests

Electrochemical studies were all performed in a three-electrode configuration with a CHI 710 electrochemical workstation. The counter electrode was a graphite rod, while a Ag/AgCl electrode in 1.0 M KCl served as the reference electrode. A reversible hydrogen electrode (RHE) was used to calibrate the potential of the reference electrode, and the potentials in the present study were all referenced to this RHE. The working electrode was a gold ring-glassy carbon disk electrode (RRDE) purchased from Pine Research Instrument. In the preparation of catalyst inks, the nanocomposites prepared above (0.8 mg) and a Nafion solution (20%, 2.0 μL) were added to a mixture of water and ethanol (1:1 v:v, 200 μL). After 30 min's sonication, a calculated amount of the ink (5.0 μL) was cast onto the glassy carbon disk. The loading of the catalysts was estimated to be 84.2 μg cm^{-2}. After the catalyst film was dried, it was covered with 3.0 μL of 20% Nafion, and the electrode was introduced into the electrolytes for electrochemical measurements.

4.4 Results and discussion

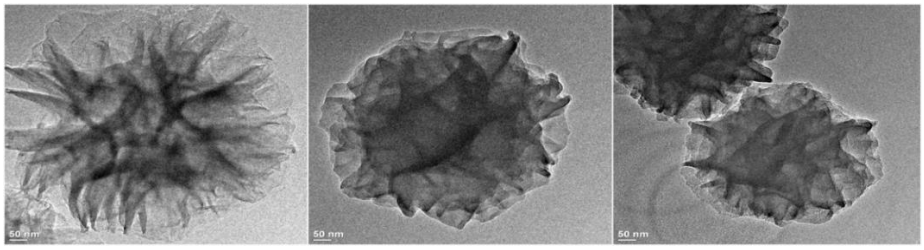

Figure 4.1 FTEM images of (a) PACN-70, (b) PACN-230, and (c) NCF.

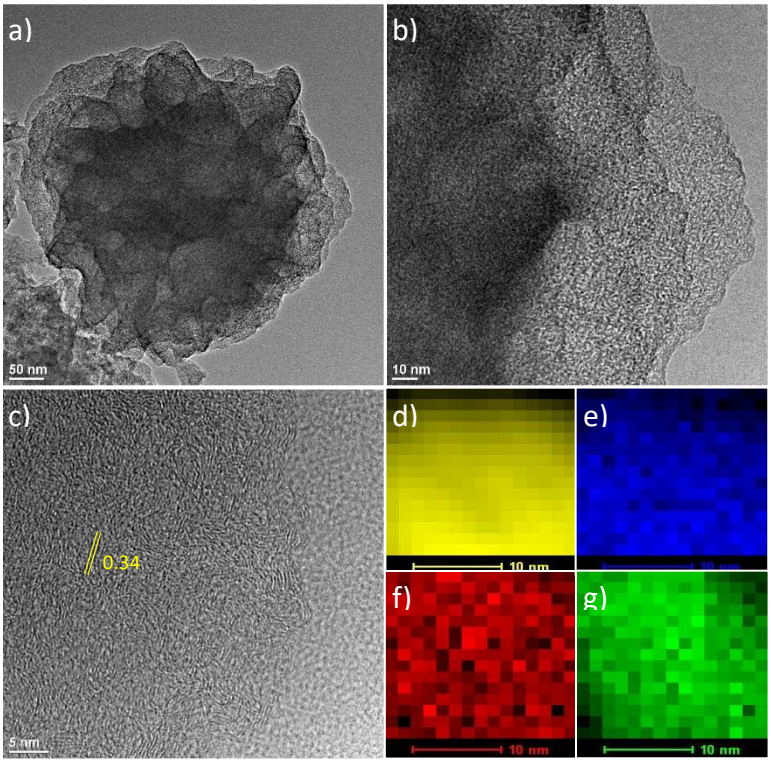

Figure 4.2(a-c) TEM images of FeNi-NCF(3) at different magnifications, along with the associated elemental maps of (d) C, (e) N, (f) Fe, and (g) Ni.

Polyacrylonitrile was first prepared by AIBN-initiated free radical polymerization of acrylonitrile, exhibiting a nanoflower morphology with a diameter of ca. 850 nm and porous

petals [22], as manifested in TEM measurements (Figure 4.1). The overall morphology was stabilized in a subsequent thermal annealing in ambient at 230 °C, but with a slight shrinkage of the nanoflowers to ca. 750 nm (Figure 4.1b), suggesting increasing rigidity and compactness of the polymer flowers [23]. Note that this stabilization step was critical to preserve the nanoflower structure after pyrolysis. Upon carbonization at 900 °C (Figure 4.1c), one can see that carbon nanoflowers (NCF) were produced but the size was further decreased to 400-500 nm [24]. A similar structure was observed for the FeNi-NCF samples. From Figure 4.2, the FeNi-NCF(3) sample can be seen to retain the flower morphology with a diameter of ca. 400 nm. Furthermore, at higher magnifications, no particulates can be identified within the flaky petals, suggesting that the metal species were atomically distributed within the carbon scaffolds (Figure 4.2b); furthermore, the nanoflowers entailed only short-range lattice fringes, featuring an interplanar separation of ca. 0.34 nm (Figure 4.2c), suggestive of the formation of highly defective carbon. In fact, from the elemental maps acquired with energy-dispersive X-ray spectroscopy (Figure 4.2 d-g), one can see a rather uniform distribution of Fe, Ni, and N over the C background.

The sample structures were further characterized by XRD measurements (not shown), where only two broad peaks were identified at $2\Theta \approx 21$ and 41^{o}, due to the (002) and (101) facets of graphitic carbon, respectively (PDF card #65-6212), confirming successful carbonization of polyacrylonitrile. No diffraction features characteristic of metal/metal oxide nanoparticles can be resolved, consistent with atomic dispersion of the metal species into the carbon matrix.

The sample porosity was then examined by nitrogen sorption measurements (Figure 4.3). From panel a, the metal-free NCF can be seen to display a Type-I nitrogen adsorption/desorption isotherm with a hysteresis loop, which suggests mostly micropores, whereas FeNiC-NCF(3) produced a Type-IV isotherm, suggesting both micropores and mesopores in the sample. From the pore size distributions (panel b), NCF was indeed found to consist mostly of micropores of ca. 1.25 nm, whereas FeNi-NCF(3) contained a significant

portion of mesopores at 2.5 nm, likely due to the thermal volatility of the metal compounds that that renders them effective porogens [5]. Additionally, the Brunauer-Emmet-Teller (BET) specific surface was found to increase from 90 $m^2 g^{-1}$ for NCF to 110 $m^2 g^{-1}$ for FeNi-NCF(3).

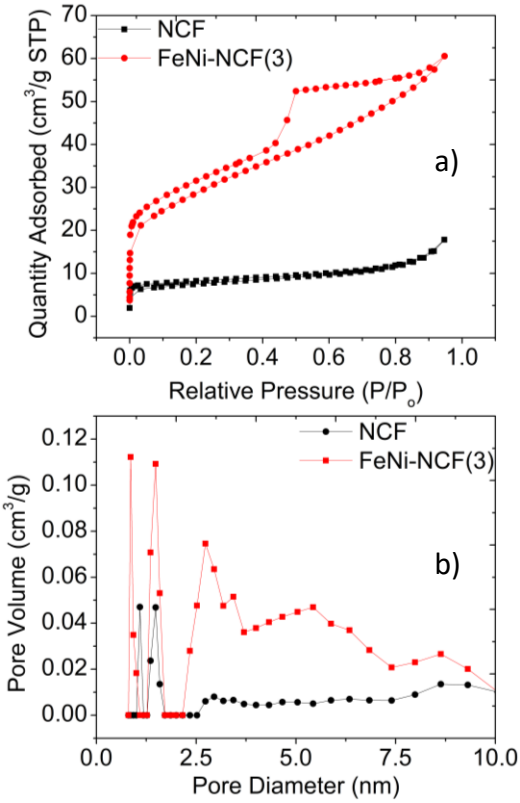

Figure 4.3(a) N2 sorption isotherms and (b) the corresponding pore size distributions of NCF and FeNi-NCF(3).

XPS measurements were then carried out to evaluate the elemental composition and valency of the nanocomposites. Figure 4.4 shows the survey spectra, where the elements of carbon, nitrogen, and oxygen can be clearly resolved within the NCF, Fe-NCF and FeNi-NCF samples, with additional Fe and Ni for the latter, indicative of successful doping of the carbon skeletons by N, Fe and Ni. On the basis of the integrated peak areas, the metal-free NCF sample was found to consist of 90.11 at% of C, 6.20 at% of N and 3.70 at% of O. For the Fe-NCF sample, 92.2 at% of C, 2.28 at% of N, 0.13 of Fe at%, and 5.41 at% of O. In the FeNi-NCF series the carbon content stayed virtually invariant at ca. 90 at%; the N content was

about 2.28 at% for Fe-NCF, 2.21 at% for FeNi-NCF(1), 4.09 at% for FeNi-NCF(2), and 4.10 at% for FeNi-NCF(3); and O content increased somewhat to 6.97 at% for FeNi-NCF(1), 6.10 at% for FeNi-NCF(2), and 4.41 at% for FeNi-NCF(3), suggesting that the basic carbon scaffold was virtually invariant with the addition of the metal precursors (Table 4.1). Notably, the total metal content remained low among the Fe-NCF and FeNi-NCF samples, only 0.15 at% for Fe-NCF, 0.26 at% for FeNi-NCF(1), 0.27 at% for FeNi-NCF(2), and 0.22 at% for FeNi-NCF(3), with a respective Fe:Ni atomic ratio of 1.0, 2.0 and 3.5 for the FeNi-NCF series, in good agreement with the initial feeds.

Table 4.1Elemental compositions of the sample series from XPS measurements.

Sample	**C**	**N**	**Fe**	**Ni**	**O**	**Metal %**	**Fe/Ni Ratio**
NCF	90.1	6.2		-	3.70		-
Fe-NCF	92.2	2.28	0.15	-	-	0.15	-
FeNi-NCF(1)	90.6	2.21	0.13	0.13	6.97	0.26	1.0
FeNi-NCF(2)	89.5	4.09	0.18	0.091	6.10	0.27	2.0
FeNi-NCF(3)	91.3	4.10	0.17	0.049	4.41	0.22	3.5

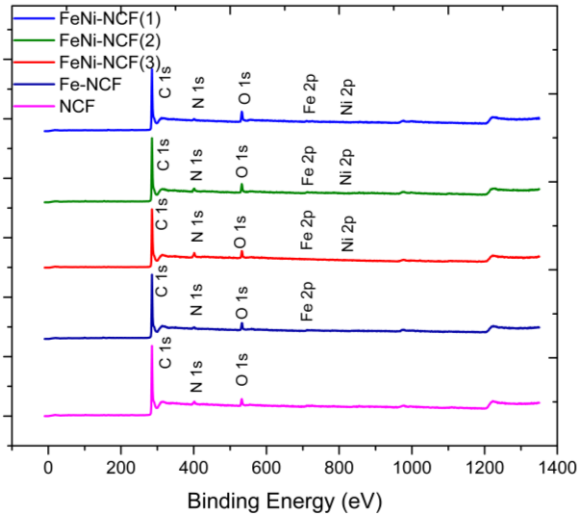

Figure 4.4. XPS survey spectra of FeNi-NCF(1), FeNi-NCF(2), FeNi-NCF(3), and NCF.

The high-resolution C 1s spectra are shown in Figure 4.5, where the FeNi-NCF samples all displayed a major component at 284.4 eV due to graphitic sp^2 carbon, evidence of successful carbonization of polyacrylonitrile, C sp^3 at 285.1 eV, with two minor ones at 286.7 and 289.7 eV, corresponding to oxidized carbon such as C=O and COOH, respectively [25]. The corresponding N 1s, O 1s, Fe 2p, and Ni 2p spectra for Fe-NCF and FeNi-NCF are depicted in Figure 24 and 25. From the N 1s spectra in Figure 24a, six N species can be resolved at ca. 398.1 eV for pyridinic N, 398.9 eV for metal-N, 399.9 eV for pyrrolic, 400.8 eV for graphitic, 401.7 eV for oxidized N, and 403 eV for NO_2 [26, 27]. Note that the metal-N peak was absent in the NCF sample (Figure S5). The O 1s spectra are shown in Figure 24b, which contain three components, 532.2 eV for O-C, 533.3 eV for O-H, and 530.1 eV for metal-O [28, 29]. These results collectively indicate that the metal species are most likely involved in the chelation interactions with the N and O dopants within the carbon skeletons.

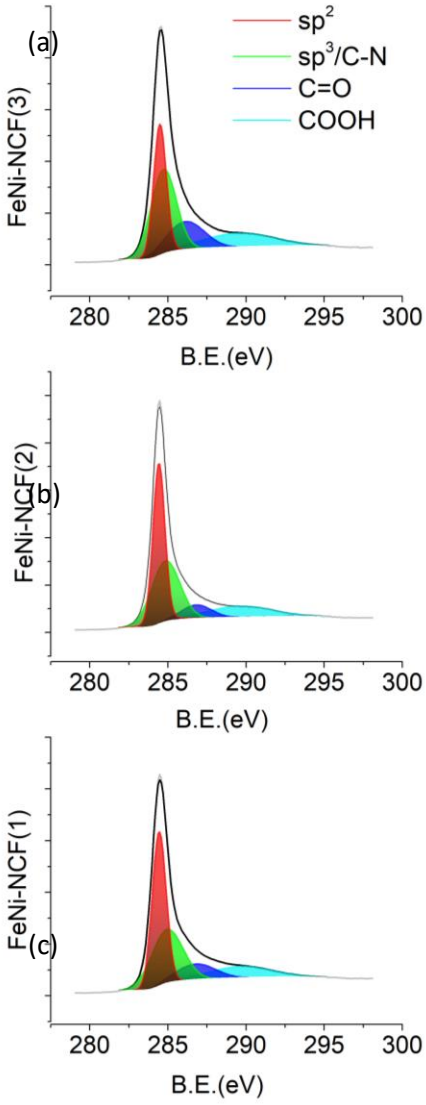

Figure 4.5. High-resolution C 1s spectra of the series of FeNi-NCF samples.

From the Fe 3p spectra in Figure 4.6c and 4.7, the FeNi-NCF and Fe-NCF samples all displayed a very consistent binding energy of the Fe $2p_{3/2}$ electrons at about 710 eV, which can be ascribed to Fe^{2+}, respectively. Similarly, from the Ni 2p spectra in Figure 4.6d, the FeNi-NCF samples can be seen to show a binding energy of ca. 854.6 eV for the $2p_{3/2}$

electrons of Ni^{2+} [17, 30]. Interestingly, one can see that among the series, the FeNi-NCF(3) sample showed the lowest binding energy for Fe $2p_{3/2}$ at 709.58 eV, but the highest binding energy for Ni $2p_{3/2}$ at 854.69 eV, suggesting that the Fe^{2+} centers were in an electron-withdrawing environment (Table 4.2) [17, 31]. Note that such Ni to Fe metal-metal charge transfer is conducive to ORR electrochemistry catalyzed by metal-doped carbon nanocomposites (vide infra) [32, 33].

Table 4.2 Binding energies of Fe and Ni in the sample series from XPS measurements.

Sample	Fe (B.E.)	Ni (B.E)
NCF	-	-
Fe-C	710.11	-
FeNi-NCF(1)	710.43	854.45
FeNi-NCF(2)	710.11	854.61
FeNi-NCF(3)	709.58	854.69

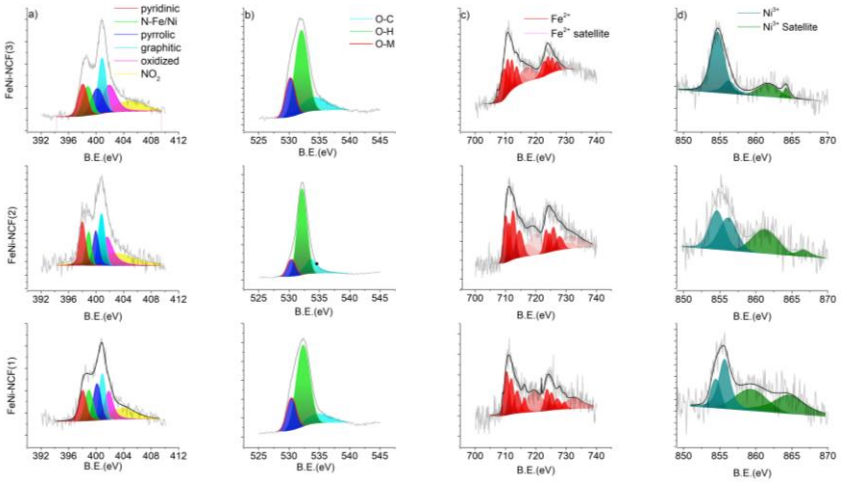

Figure 4.6High-resolution XPS spectra of the FeNi-NCF samples: (a) N 1s, (b) O 1s, (c) Fe 2p, and (d) Ni 2p.

.

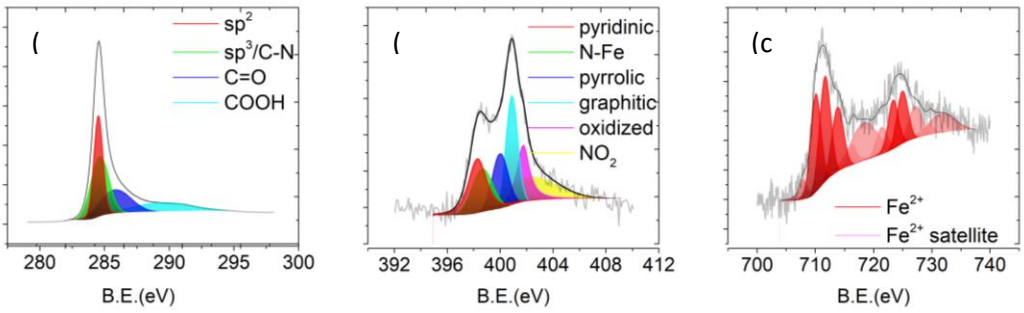

Figure 4.7High-resolution scans of the (a) C 1s, (b) N 1s, and (c) Fe 2p electrons of Fe-NCF.

The ORR activity of the nanocomposites was then evaluated and compared in alkaline media. As shown in Figure 4.8a, the nanocomposite samples all exhibited a non-zero ORR activity in 0.1 M KOH; yet the activity varied among the samples. The metal-free NCF exhibited only a minimal activity featuring an onset potential (E_{onset}) below +0.6 V. The activity was substantially improved with the Fe-NCF sample, with E_{onset} = +0.89 V and (half-wave potential) $E_{1/2}$ = +0.72 V, signifying the key role of metal species in driving the electron-transfer kinetics. The performance was further enhanced with the FeNi-NCF samples, and FeNi-NCF(3) exhibited the best activity within the series, where the $E_{1/2}$ (+0.79 V) and E_{onset} (+0.93 V) values were only somewhat lower than those of the commercial Pt/C benchmark ($E_{1/2}$ = +0.83 V, E_{onset} = +1.00 V).

The electron-transfer number (n) and H_2O_2 yield (H_2O_2%) were then estimated from the RRDE data (Figure 4.8b). Again, FeNi-NCF(3) exhibited the best performance, with the higher n and lower H_2O_2% than all other samples. For example, at +0.70 V the n/H_2O_2% values were 3.99/0.59 for FeNi/NCF(3), in comparison to 3.82/9.6 for FeNi/NCF(2), 3.87/7.1 for FeNi/NCF(1), 3.99/0.69 for Fe-NCF, and 3.99/0.4 for Pt/C, indicating high selectivity of the 4e- ORR pathway by the nanocomposites. Figure 4.8c shows the associated Tafel plots,

where FeNi-NCF(3) exhibits the lowest slope of 77.62 mV dec^{-1}, which suggested that the first electron reduction of oxygen was likely the rate-limiting step [32, 33].

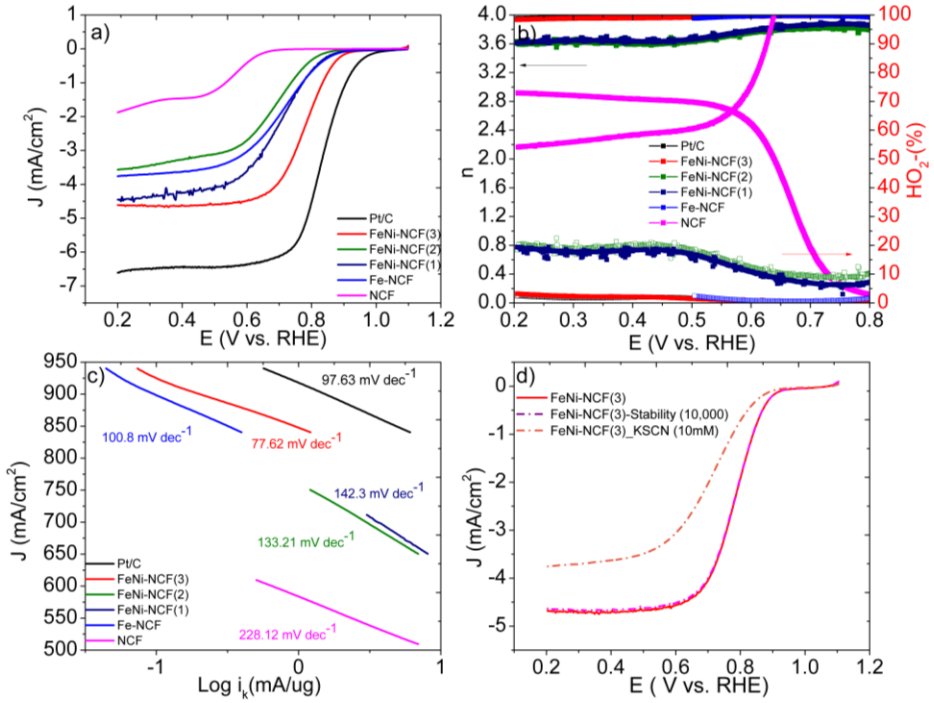

Figure 4.8. (a) ORR polarization curves of the sample series in an oxygen-purged 0.1 M KOH solution. Potential sweep rate 10 mV s-1, rotation rate 1600 rpm. (b) Electron transfer number (left y axis) and H2O2% yield (right y axis) for the electrocatalysts in (a), and (c) the corresponding Tafel plots. (d) ORR polarization curves in the first scan and after 10,000 potential cycles within +0.2 to +1.1 V, as well as with the introduction of KSCN (10 mM).

As mentioned earlier, the FeNi-NCF samples consisted of a similar elemental composition and total metal contents (Table 4.1). Therefore, it is most likely that the remarkable ORR activity of FeNi-NCF(3) is a consequence of the collective contributions of a porous structure and effective Ni-Fe charge transfer that facilitated the adsorption and ultimately reduction of oxygen [32, 33].

Notably, the FeNi-NCF(3) sample also exhibited remarkable stability. The ORR polarization curve remained virtually unchanged after 10,000 potential cycles within the range

of +0.20 to 1.00 V (Figure 4.8d). Yet, the introduction of KSCN (10 mM) led to a substantial diminishment of the ORR activity (Figure 4.8d), due to blocked access to the catalytic active sites, further confirming the key role of metal species in ORR electrocatalysis.

4.5 Conclusion

In this study, carbon nanoflowers doped with both metal (Fe and Ni) and non-metal (N) elements were readily synthesized by controlled pyrolysis of polyacrylonitrile flowers in the presence of Fe and Ni compounds. The obtained FeNi-NCF nanocomposites exhibited a similar elemental composition and total metal content. However, the sample that exhibited a high Fe:Ni atomic ratio showed the best ORR performance that was close to that of commercial Pt/C, likely due to the Ni to Fe metal-metal charge transfer that facilitated the adsorption and ultimately reduction of oxygen, as evidenced in XPS measurements. Results from this study suggest that structural engineering of the electronic properties of metal dopants is a critical strategy in improving the electrocatalytic activity of carbon-based nanocomposites.

4.6 References

[1] K.I. Ozoemena, S. Chen, Nanomaterials for Fuel Cell Catalysis, Nanostructure Science and Technology, Springer International Publishing: Imprint: Springer, Cham, 2016, pp. 1 online resource.

[2] W. Wang, B. Lei, S.J. Guo, Engineering Multimetallic Nanocrystals for Highly Efficient Oxygen Reduction Catalysts, Adv Energy Mater, 6 (2016) 1600236.

[3] G.Q. He, Y. Song, K. Liu, A. Walter, S. Chen, S.W. Chen, Oxygen Reduction Catalyzed by Platinum Nanoparticles Supported on Graphene Quantum Dots, Acs Catal, 3 (2013) 831-838.

[4] J. Ustarroz, I.M. Ornelas, G.H. Zhang, D. Perry, M. Kang, C.L. Bentley, M. Walker, P.R. Unwin, Mobility and Poisoning of Mass-Selected Platinum Nanoclusters during the Oxygen Reduction Reaction, Acs Catal, 8 (2018) 6775-6790.

[5] W.H. Niu, L.G. Li, S.W. Chen, Recent Progress in Template-Assisted Synthesis of Nitrogen-Doped Porous Carbons for Oxygen Electroreduction, Journal of Electrochemistry, 23 (2017) 110-122.

[6] Y. Peng, B.Z. Lu, S.W. Chen, Carbon-Supported Single Atom Catalysts for Electrochemical Energy Conversion and Storage, Adv Mater, 30 (2018) 1801995.

[7] Y.X. Wang, H.Y. Su, Y.H. He, L.G. Li, S.Q. Zhu, H. Shen, P.F. Xie, X.B. Fu, G.Y. Zhou, C. Feng, D.K. Zhao, F. Xiao, X.J. Zhu, Y.C. Zeng, M.H. Shao, S.W. Chen, G. Wu, J. Zeng, C. Wang, Advanced Electrocatalysts with Single-Metal-Atom Active Sites, Chem Rev, 120 (2020) 12217-12314.

[8] J.A. Behan, E. Mates-Torres, S.N. Stamatin, C. Dominguez, A. Iannaci, K. Fleischer, M.K. Hoque, T.S. Perova, M. Garcia-Melchor, P.E. Colavita, Untangling Cooperative Effects of Pyridinic and Graphitic Nitrogen Sites at Metal-Free N-Doped Carbon Electrocatalysts for the Oxygen Reduction Reaction, Small, 15 (2019) 1902081.

[9] N. Wang, B.Z. Lu, L.G. Li, W.H. Niu, Z.H. Tang, X.W. Kang, S.W. Chen, Graphitic Nitrogen Is Responsible for Oxygen Electroreduction on Nitrogen-Doped Carbons in Alkaline Electrolytes: Insights from Activity Attenuation Studies and Theoretical Calculations, Acs Catal, 8 (2018) 6827-6836.

[10] W.H. Niu, L.G. Li, X.J. Liu, N. Wang, J. Liu, W.J. Zhou, Z.H. Tang, S.W. Chen, Mesoporous N-Doped Carbons Prepared with Thermally Removable Nanoparticle Templates: An Efficient Electrocatalyst for Oxygen Reduction Reaction, J Am Chem Soc, 137 (2015) 5555-5562.

[11] B.Z. Lu, T.J. Smart, D.D. Qin, J.E. Lu, N. Wang, L.M. Chen, Y. Peng, Y. Ping, S.W. Chen, Nitrogen and Iron-Codoped Carbon Hollow Nanotubules as High-Performance Catalysts toward Oxygen Reduction Reaction: A Combined Experimental and Theoretical Study, Chem Mater, 29 (2017) 5617-5628.

[12] X. Liu, Y. Jiao, Y. Zheng, M. Jaroniec, S.Z. Qiao, Building Up a Picture of the Electrocatalytic Nitrogen Reduction Activity of Transition Metal Single-Atom Catalysts, J Am Chem Soc, 141 (2019) 9664-9672.

[13] C.C. Hou, L.L. Zou, L.M. Sun, K.X. Zhang, Z. Liu, Y.W. Li, C.X. Li, R.Q. Zou, J.H. Yu, Q. Xu, Single-Atom Iron Catalysts on Overhang-Eave Carbon Cages for High-Performance Oxygen Reduction Reaction, Angew Chem Int Edit, 59 (2020) 7384-7389.

[14] T. He, B.Z. Lu, Y. Chen, Y. Wang, Y.Q. Zhang, J.L. Davenport, A.P. Chen, C.W. Pao, M. Liu, Z.F. Sun, A. Stram, A. Mordaunt, J. Velasco, Y. Ping, Y. Zhang, S.W. Chen, Nanowrinkled Carbon Aerogels Embedded with FeNx Sites as Effective Oxygen Electrodes for Rechargeable Zinc-Air Battery, Research-China, 2019 (2019) 6813585.

[15] B.Z. Lu, Q.M. Liu, S.W. Chen, Electrocatalysis of Single-Atom Sites: Impacts of Atomic Coordination, Acs Catal, 10 (2020) 7584-7618.

[16] M. Lefevre, E. Proietti, F. Jaouen, J.P. Dodelet, Iron-Based Catalysts with Improved Oxygen Reduction Activity in Polymer Electrolyte Fuel Cells, Science, 324 (2009) 71-74.

[17] R. Mercado, C. Wahl, J.E. Lu, T.J. Zhang, B.Z. Lu, P. Zhang, J.N.Q. Lu, A. Allen, J.Z. Zhang, S.W. Chen, Nitrogen-Doped Porous Carbon Cages for Electrocatalytic Reduction of Oxygen: Enhanced Performance with Iron and Cobalt Dual Metal Centers, Chemcatchem, 12 (2020) 3230-3239.

[18] Y. Chen, S.Q. Hu, F. Nichols, F. Bridges, S.T. Kan, T. He, Y. Zhang, S.W. Chen, Carbon aerogels with atomic dispersion of binary iron-cobalt sites as effective oxygen catalysts for flexible zinc-air batteries, J Mater Chem A, 8 (2020) 11649-11655.

[19] S. Yuan, L.L. Cui, Z.Y. Dou, X. Ge, X.Q. He, W. Zhang, T. Asefa, Nonprecious Bimetallic Sites Coordinated on N-Doped Carbons with Efficient and Durable Catalytic Activity for Oxygen Reduction, Small, 16 (2020) 2000742.

[20] S. Sarkar, A. Biswas, T. Purkait, M. Das, N. Kamboj, R.S. Dey, Unravelling the Role of Fe-Mn Binary Active Sites Electrocatalyst for Efficient Oxygen Reduction Reaction and Rechargeable Zn-Air Batteries, Inorg Chem, 59 (2020) 5194-5205.

[21] Z.J. Zhu, H.J. Yin, Y. Wang, C.H. Chuang, L. Xing, M.Y. Dong, Y.R. Lu, G. Casillas-Garcia, Y.L. Zheng, S. Chen, Y.H. Dou, P. Liu, Q.L. Cheng, H.J. Zhao, Coexisting Single-Atomic Fe and Ni Sites on Hierarchically Ordered Porous Carbon as a Highly Efficient ORR Electrocatalyst, Adv Mater, 32 (2020) 2004670.

[22] D.M. Koshy, S.C. Chen, D.U. Lee, M.B. Stevens, A.M. Abdellah, S.M. Dull, G. Chen, D. Nordlund, A. Gallo, C. Hahn, D.C. Higgins, Z.N. Bao, T.F. Jaramillo, Understanding the Origin of Highly Selective CO2 Electroreduction to CO on Ni,N-doped Carbon Catalysts, Angew Chem Int Edit, 59 (2020) 4043-4050.

[23] S.C. Chen, D.M. Koshy, Y. Tsao, R. Pfattner, X.Z. Yan, D.W. Feng, Z.A. Bao, Highly Tunable and Facile Synthesis of Uniform Carbon Flower Particles, J Am Chem Soc, 140 (2018) 10297-10304.

[24] Z.Y. Xing, Y.T. Qi, Z.Q. Tian, J. Xu, Y.F. Yuan, C. Bommier, J. Lu, W. Tong, D.E. Jiang, X.L. Ji, Identify the Removable Substructure in Carbon Activation, Chem Mater, 29 (2017) 7288-7295.

[25] T. He, Y. Peng, Q.X. Jia, J.E. Lu, Q.M. Liu, R. Mercado, Y. Chen, F. Nichols, Y. Zhang, S.W. Chen, Nanocomposites Based on Ruthenium Nanoparticles Supported on Cobalt and Nitrogen-Codoped Graphene Nanosheets as Bifunctional Catalysts for Electrochemical Water Splitting, Acs Appl Mater Inter, 11 (2019) 46912-46919.

[26] Q.M. Liu, Y. Peng, Q.X. Li, T. He, D. Morris, F. Nichols, R. Mercado, P. Zhang, S.W. Chen, Atomic Dispersion and Surface Enrichment of Palladium in Nitrogen-Doped Porous Carbon Cages Lead to High-Performance Electrocatalytic Reduction of Oxygen, Acs Appl Mater Inter, 12 (2020) 17641-17650.

[27] T. He, Y.Q. Zhang, Y. Chen, Z.Z. Zhang, H.Y. Wang, Y.F. Hu, M. Liu, C.W. Pao, J.L. Chen, L.Y. Chang, Z.F. Sun, J. Xiang, Y. Zhang, S.W. Chen, Single iron atoms stabilized by microporous defects of biomass-derived carbon aerogels as high-performance cathode electrocatalysts for aluminum-air batteries, J Mater Chem A, 7 (2019) 20840-20846.

[28] D.M. Morales, M.A. Kazakova, S. Dieckhofer, A.G. Selyutin, G.V. Golubtsov, W. Schuhmann, J. Masa, Trimetallic Mn-Fe-Ni Oxide Nanoparticles Supported on Multi-Walled Carbon Nanotubes as High-Performance Bifunctional ORR/OER Electrocatalyst in Alkaline Media, Adv Funct Mater, 30 (2020) 1905992.

[29] C. Liu, H. Li, J.S. Chen, Z.X. Yu, Q. Ru, S.Z. Li, G. Henkelman, L. Wei, Y. Chen, 3d Transition-Metal-Mediated Columbite Nanocatalysts for Decentralized Electrosynthesis of Hydrogen Peroxide, Small, 17 (2021) 2007249.

[30] A.P. Grosvenor, B.A. Kobe, M.C. Biesinger, N.S. McIntyre, Investigation of multiplet splitting of Fe 2p XPS spectra and bonding in iron compounds, Surf Interface Anal, 36 (2004) 1564-1574.

[31] A.P. Grosvenor, M.C. Biesinger, R.S. Smart, N.S. McIntyre, New interpretations of XPS spectra of nickel metal and oxides, Surf Sci, 600 (2006) 1771-1779.

[32] H.X. Zhong, J. Wang, Q. Zhang, F.L. Meng, D. Bao, T. Liu, X.Y. Yang, Z.W. Chang, J.M. Yan, X.B. Zhang, In Situ Coupling FeM (M = Ni, Co) with Nitrogen-Doped Porous Carbon toward Highly Efficient Trifunctional Electrocatalyst for Overall Water Splitting and Rechargeable Zn-Air Battery, Adv Sustain Syst, 1 (2017) 1700020.

[33] Y. Cheng, S. He, J.P. Veder, R. De Marco, S.Z. Yang, S. Jiang, Atomically Dispersed Bimetallic FeNi Catalysts as Highly Efficient Bifunctional Catalysts for Reversible Oxygen Evolution and Oxygen Reduction Reactions, Chemelectrochem, 6 (2019) 3478-3487.